

Transition Metal Intercalated Poly(heptazine imides) for Electro- and Photocatalytic Water Splitting

vorgelegt von

M. Sc.

Meng-Yang Ye

an der Fakultät II – Mathematik und Naturwissenschaften
der Technischen Universität Berlin
zur Erlangung des akademischen Grades

Doktor der Naturwissenschaften

- Dr. rer. nat. -

genehmigte Dissertation

Promotionsausschuss:

Vorsitzender: Prof. Dr. Roel van de Krol

Gutachter: Prof. Dr. Arne Thomas

Gutachter: Prof. Dr. Markus Antonietti

Tag der wissenschaftlichen Aussprache: 06. September 2021

Berlin 2021

Acknowledgements

Time flies and four years have passed in a blink. I still remember the day I joined AK Thomas, that happened to be Matthias' defense day. I was so fascinated by the hat Matthias got after he succeeded with the defense, that I couldn't wait to get mine. At this moment that I finally submit my thesis, I can see that hat waving at me in the foreseeable future.

Doing a PhD is certainly not easy, but doing a PhD with the support of the right people was also the most enjoyable experience in my life.

I would first like to thank Prof. Thomas for all the inspiring and enlightening discussions over the years. His creative way of thinking and immense collection of knowledge always amaze me. He is not only the best advisor to turn to when I encountered scientific problems, but also the most insightful reviewer who always checks the solidness of the research I made. I will always be proud that I did my PhD research under his supervision.

Special thanks to Prof. Dr. Markus Antonietti and Max-Planck institute of colloids and interfaces for their support during my research, especially Dr. Nadezda V. Tarakina who measured all the beautiful STEM images.

I would like to thank my kind collaboration partners, Prof. Dr. Robert Bittl, and Dr. Christian Teutloff for the pulse EPR measurements, Dr. Wing Ying Chow for the NMR measurements, Sebastian Praetz and Prof. Dr. Guiying Tian for the measurement and analysis of XAS results, Prof. Dr. Lequan Liu for the PL spectrum measurement and water oxidation activity evaluation. Dr. Samrat Ghosh for the DFT calculation. Without all these sophisticated characterizations and calculations, I couldn't possibly learn so much about PHIs.

I'm also very grateful that Dipl. Christoph Fahrenson and Zelmi provided me a great platform to measure the SEM over these years, it was not only very helpful for my own research, but also gave me a lot of chances to participate in many interesting scientific projects.

Research is like a battle fighting against uncertainty, there were so many moments that I felt lost, frustrated, and struggling to find the courage to keep going. But having a group like AK Thomas backing you up is the most reassuring thing one can expect. I would like to thank our former and current group members, Dr. Johannes Schmidt, Dr. Pradip Pachfule, Dr. Jérôme Roeser, Dr. Matthias Trunk, Dr. Shuang Li, Dr. Xiaojia Zhao, Dr. Suman Chandra, Sarah Vogl, Jin Yang, Amitava Acharjya, Michaela König, Nicolas Chaoui, Thomas Langenhahn, Julia Grüneberg, Vincent Weigelt, Hüseyin Küçükkeçeci, Najmeh Bashiri, Robert Sroka, Leo

Sagurna, Yasmine Ziouani, Michael Traxler. And our technicians Maria Unterweger and Christina Eichenauer. When I was lost, they brainstormed with me to tackle the problem, when I was frustrated, they cheered me up with warm encouragement, they are not only the smart co-workers always helpful with the work, also friends I can turn to when I need help in daily life.

I would like to thank Dr. Jean-Philippe Lonjaret who brought me to the warm family of BIGNSE. I want to thank my former supervisors, Prof. Dr. Wei Zhao, Prof. Dr. Zhurui Shen, Prof. Dr. Huiming Ji, they guide me to this fascinating world of science, taught me how to research and send me to this better platform, where I can learn from the best minds coming from all over the world.

I am also grateful that I could work with Dr. Ralph Krähnert, Marvin Frisch and Aleks Arinchtein shortly before I leave for my new editorial job. They are an amazing and exuberant team that always has interesting results and ideas coming out.

I would like to thank my friends in Berlin, Rhea, Piyush, Anika, Esteban and Jean, they are like my family in this foreign country. Just as the writer of the famous show *Friends* used to say, there was a time in your life that your friends are everything in your life. The years in Berlin were this kind of time for me, and I am grateful that they are the friends that light up my life.

Last but not least, I would like to thank my family. I want to thank Leon, my husband and the love of my life, who is always so supportive, loving and understanding, and always willing to join every adventure of mine in the past and in the future. He celebrated when I enjoy my triumph of finding some exciting results, and he comforted me when I doubt myself. I want to thank my parents, who always encourage me, believe in me. They gave me a lot of space to explore the world and make my own decision, even when I was a little kid. It was because of the values they taught me, that I can grow up with curiosity and passion, and enjoyed life as a researcher.

All in all, I would never forget the years I spent in Berlin, all these kind and intelligent people I met, all those exciting experiences I had. Doing this PhD here is not only an important part of my career but also a wonderful journey in my life.

Abstract

Overall water splitting, as a sustainable pathway to obtain clean energy, can be achieved via electrocatalytic and photocatalytic reactions. However, neither of them has yet been widely applied in the industry. Thus, the achievement of electro- and photocatalysts for overall water splitting is still in high demand.

Carbon nitride has been commonly applied in both electro- and photocatalysis over the past years. For electrocatalysis, the abundant and well-dispersed nitrogen sites of carbon nitride can act as efficient metal coordinated sites, which is crucial for composing a type of high-performance electrocatalysts— $M-N_x$ electrocatalysts. In the field of photocatalysis, carbon nitride, as a metal-free semiconductor, has risen as a promising candidate for multiple photocatalytic applications due to its favorable band position. In fact, many state-of-the-art photocatalysts for visible-light-driven hydrogen evolution are based on carbon nitride.

However, carbon nitride has its limitations. The low conductivity and electrochemical stability of carbon nitride have restricted its performance in electrocatalysis. Therefore, carbon nitride must be mixed with carbon additives to perform as electrocatalyst. For photocatalytic water splitting, in spite of carbon nitrides' high activity in catalyzing hydrogen evolution, it is barely active in catalyzing the other half-reaction, water oxidation. This is because the valence band of carbon nitride is usually not positive enough to drive this half-reaction.

Poly(heptazine) imide (PHI) is an ionic carbon nitride, which not only inherits the attractive properties of carbon nitride, but also overcomes many of the aforementioned limitations. Unlike the polymeric carbon nitrides, which are prepared by condensing urea, melamine, cyanamide, dicyanamide, *etc.*, PHI is prepared by salt-melt assisted condensation of triazole or tetrazole. The polymeric carbon nitride is composed of heptazine units connected by amine bridges. The heptazine units in PHI are linked by deprotonated imides, whose charge is counterbalanced by metal cations introduced by the salt template.

In this thesis, a series of transition metal, noble metal, and bi-metal intercalated poly(heptazine) imide (noted as PHI-M, $M = Co, Ni, Cu, Fe, Mn, Pt \dots$) is synthesized via facile salt melt assisted condensation of tetrazole precursor for modifying the composition of the salt template. The structures of these PHI-M's are systematically characterized, proving that the PHI backbones stay intact after the intercalation of different metal cations.

The synergetic effects between the intercalated metal cations and the PHI backbone are also studied in this thesis. On the one hand, by altering the composition of the metal salt in the salt template, the metal species intercalated in the PHI backbone can be changed accordingly. This property not only makes it easy to embed different metal active sites into the PHI backbones for various catalytic reactions, but also shown to be an efficient pathway to tune the band position of PHI-based photocatalysts. On the other hand, the abundant negatively charged nitrogen sites and metal cations in the PHI backbone remarkably enhance the charge mobility of the material, enabling it to work as an electrocatalyst without conducting additives.

The catalytic activities of cobalt and nickel intercalated poly(heptazine) imides (PHI-Co and PHI-Ni) were evaluated, and they turned out to be highly active electro- and photocatalysts. PHI-Co shows excellent electrocatalytic OER activity and photocatalytic water oxidation activity. As an OER electrocatalyst, the overpotential ($j = 10 \text{ mA/cm}^2$) of the best-performing PHI-Co-0.5 (Co content: 0.45 wt%) is 0.324 V, standing among the best polymer-based electrocatalysts. When applied in photocatalysis, the most active PHI-Co-0.1 (Co content: 0.08 wt%) shows a visible-light-driven oxygen generation activity of $589 \mu\text{mol h}^{-1} \text{ g}^{-1}$, which is one of the most active catalysts that have been reported for water oxidation. Furthermore, PHI-Ni is highly active in catalyzing visible-light-driven hydrogen evolution. PHI-Ni-0.7 (Ni content 0.74 wt%), which shows visible-light-driven hydrogen generation activity of $1996 \mu\text{mol g}^{-1} \text{ h}^{-1}$, more than 14-fold higher than Ni-free PHI, and 42-fold higher than polymeric CN.

Zusammenfassung

Wasserspaltung stellt einen nachhaltigen Weg zur Gewinnung von sauberer Energie dar, welche durch Elektro- und Photokatalyse erreicht werden kann. Da jedoch keiner der katalytischen Prozesse bisher eine breite Anwendung in der Industrie findet, werden effiziente Elektro- und Photokatalysatoren für die Wasserspaltung nach wie vor dringend benötigt.

Kohlenstoffnitride wurden in den letzten Jahren häufig sowohl in Elektro- als auch in Photokatalyse eingesetzt. Für die Elektrokatalyse können die reichlich vorhandenen und homogen verteilten Stickstoffeinheiten des Kohlenstoffnitrids als Koordinationsstellen für Metalle dienen, die zur Herstellung effizienter Elektrokatalysatoren (M-N_x-Elektrokatalysatoren) von entscheidender Bedeutung sind. In der Photokatalyse haben sich Kohlenstoffnitride aufgrund ihrer günstigen Bandposition als vielversprechender Kandidat für diverse photokatalytische Anwendungen erwiesen. Tatsächlich basieren viele neuartige Photokatalysatoren auf Kohlenstoffnitriden, welche durch Bestrahlung mit sichtbarem Licht Wasserstoff erzeugen.

Jedoch haben Kohlenstoffnitride geringe Leitfähigkeit und elektrochemische Stabilität. Aus diesem Grund wird die Leistung bei der Elektrokatalyse stark eingeschränkt. Daher müssen Kohlenstoffnitride mit Kohlenstoff gemischt werden, um als Elektrokatalysator eingesetzt zu werden. Trotz der hohen Aktivität der Kohlenstoffnitride in der photokatalytischen Wasserstoffentwicklung, können sie nicht in der photokatalytischen Wasserspaltung angewendet werden, da Kohlenstoffnitride in der zweiten Halbreaktion, der Wasseroxidation, wenig katalytisch aktiv sind. Der Grund dafür ist die Position des Valenzbandes des Kohlenstoffnitrids, welches nicht positiv genug ist, um damit die Wasseroxidation anzutreiben.

Poly(heptazin)imid (PHI) ist ein ionisches Kohlenstoffnitrid, welches nicht nur die begehrten Eigenschaften von Kohlenstoffnitrid besitzt, sondern auch viele der oben genannten Einschränkungen überwindet. Anders als die weitverbreiteten Kohlenstoffnitride, die durch Kondensation von Harnstoff, Melamin, Cyanamide, Dicyanamid usw. hergestellt werden, wird PHI durch Salzschnmelze-unterstützte Kondensation von Triazol oder Tetrazol hergestellt. Im Gegensatz zu den Melon-kondensierten Kohlenstoffnitriden, deren Heptazin-Einheiten über Amine verknüpft sind, sind die Heptazin-Einheiten des PHI über deprotonierte Imide verbrückt. Die daraus entstehende Ladung des Polymergerüsts, wird durch Gegenkationen, die durch das zu templatierende Salz eingeführt werden, ausgeglichen.

In dieser Arbeit wurde durch Modifizieren der Zusammensetzung der Salz-Template eine Reihe von Übergangsmetall-, Edelmetall- und Bimetall-interkalierten Poly(heptazin)imide (PHI-M, M = Co, Ni, Cu, Fe, Mn, Pt...) über eine Salzschnmelze-unterstützte Kondensation synthetisiert. Die Struktur dieser PHI-Ms wurde systematisch charakterisiert, um zu beweisen, dass die PHI-Polymergerüste nach Interkalation mit Metallkationen unterschiedlicher Größe und Menge, intakt bleiben können.

Außerdem werden in dieser Arbeit die synergetischen Effekte zwischen den interkalierten Metallkationen und dem PHI-Polymergerüst untersucht. Die reichlich vorhandenen, negativ geladenen Stickstoffeinheiten des PHI-Grundgerüst und deren Gegenkationen verbessern die Leitfähigkeit des Materials erheblich, wodurch dieses als Elektrokatalysator eingesetzt werden kann. Wenn eine Änderung der Zusammensetzung des Metallsalzes für die Templatierung erfolgt, ändert sich dementsprechend auch die Zusammensetzung der Metallspezies in der PHI-Struktur. Dies erleichtert nicht nur, verschiedene aktive Metallzentren für unterschiedliche katalytische Reaktionen in das PHI-Grundgerüst einzubetten, sondern erweist sich auch als effizienter Weg, um die Bandposition der PHI-basierten Photokatalysatoren abzustimmen.

Die katalytischen Aktivitäten von Cobalt-interkalierten und Nickel-interkalierten Poly(heptazin)imiden (PHI-Co und PHI-Ni) wurden näher betrachtet und erwiesen sich als hochaktive Elektro- und Photokatalysatoren. PHI-Co zeigt eine ausgezeichnete elektrokatalytische und photokatalytische OER-Aktivität. Beim Einsatz von PHI-Co-0,5 (Co-Gehalt: 0,45 wt%) als OER-Elektrokatalysator, beträgt das Überpotential ($j = 10 \text{ mA} / \text{cm}^2$) 0,324 V. Damit gehört das Material zu den besten Elektrokatalysatoren auf Polymerbasis. In der Photokatalyse zeigte das aktivste PHI-Co-0,1 (Co-Gehalt: 0,08 wt%) mit sichtbarem Licht eine Sauerstofferzeugungsrate von $639 \text{ umol h}^{-1} \text{ g}^{-1}$ und gehört damit ebenfalls zu den aktivsten Katalysatoren, die für Wasseroxidation publiziert wurde. Davon abgesehen zeigte sich PHI-Ni effizient als Photokalaysator für die Wasserstoffentwicklung durch Sommerlicht. Die maximale Aktivität für PHI-Ni wurde für das Material PHI-Ni-0,7 (0,74 wt% Ni-Gehalt) bestimmt, welches eine Wasserstofferzeugungsaktivität von $1996 \text{ umol g}^{-1} \text{ h}^{-1}$ aufweist, und somit mehr als 14-fach höher im Vergleich zu Ni-freiem PHI und 42 -fach höher im Vergleich zu Kohlenstoffnitrid ist.

Contents

1	Introduction	1
1.1	Aim and outline of this thesis	1
1.2	Structure of the thesis.....	3
1.3	Overall water splitting.....	4
1.3.1	<i>Electrolysis: development and challenges</i>	4
1.3.2	<i>Photocatalytic overall water splitting and its major challenges</i>	9
1.4	From carbon nitrides to poly(heptazine) imides	13
1.4.1	<i>Carbon nitrides</i>	13
1.4.2	<i>Poly(heptazine) imides</i>	15
1.5	Characterizing the structure of catalysts	17
1.5.1	<i>X-ray photoelectron spectroscopy (XPS)</i>	17
1.5.2	<i>X-ray absorption spectroscopy (XAS)</i>	17
1.5.3	<i>Scanning transmission electron microscopy (STEM)</i>	19
1.6	Important parameters for evaluating electrocatalytic and photocatalytic activities	19
1.6.1	<i>Overpotential</i>	19
1.6.2	<i>Tafel slope</i>	19
1.6.3	<i>Turnover frequency (TOF)</i>	20
1.6.4	<i>UV-vis spectroscopy</i>	21
1.6.5	<i>Photoluminescence spectroscopy</i>	21
1.6.6	<i>Band position</i>	21
2	Cobalt intercalated poly(heptazine) imide for electrocatalytic oxygen evolution.....	23
	Motivation	23
	Results and Discussion.....	24
	Conclusion.....	40
3	Cobalt intercalated poly(heptazine) imide as photocatalyst for water oxidation.....	43
	Motivation	43
	Results and Discussion.....	44
	Conclusion.....	55
4	Nickel intercalated poly(heptazine) imide for photocatalytic hydrogen evolution.....	57
	Motivation	57

Results and Discussion.....	58
Conclusion.....	71
5 Exploration of transition-metal- and noble-metal-intercalated poly(heptazine) imides	73
Motivation	73
Results and discussions	74
<i>Synthesis and structure of first-row transition metal intercalated poly(heptazine) imides</i>	<i>74</i>
<i>Synthesis and structure of Pt exchanged poly(heptazine) imides.</i>	<i>80</i>
<i>Synthesis and structure of Co, Ni, and Co, Pt bi-metal intercalated poly(heptazine) imides.....</i>	<i>84</i>
<i>Bandgap position tuning of PHI via the intercalating different metal cations</i>	<i>88</i>
Conclusions	92
6 Conclusions and Outlook.....	93
7 Catalysts synthesis	97
7.1 Catalysts synthesis	97
7.2 Structural characterizations.....	101
7.3 Activity evaluation.....	103
7.4 Calculations	105
Supporting Information	107
References.....	109

1 Introduction

1.1 Aim and outline of this thesis

The convenient modern life has been built on the reliance on fossil fuels since the industrial revolution¹⁻³. However, the overuse of fossil fuels in recent decades is draining the fossil fuel storage on earth at a shocking speed and escalating environmental pollution⁴⁻⁶. Hydrogen is considered an environmentally friendly solution for the impending crisis due to its high energy density and green combustion products^{4,7}.

Among the widely used methods to obtain hydrogen, such as natural gas reforming⁸, or biomass gasification⁹, overall water splitting has neither a dangerous dependence on fossil fuels and crops, nor generating carbon dioxide emission^{7,10-13}.

Overall water splitting can be achieved via electrolysis and photocatalytic reactions¹⁴⁻¹⁹. The water-splitting reaction can be divided into two half-reactions, hydrogen generation, and water oxidation which yields oxygen^{15,20}. Due to the two-electron process, the former half-reaction is relatively easier to achieve²¹. In fact, many materials have popped up as efficient photo-/electrocatalysts for hydrogen evolution^{15,22-25}. However, the other half-reaction, water oxidation, remains a major challenge. Water oxidation shows slow kinetics stemming from a four-electron oxidation process²⁶. The difficulties in optimizing this half-reaction have severely hindered the development of overall water splitting devices.

Several strategies are developed in electrocatalytic and photocatalytic water splitting to achieve high water oxidation activity. For instance, introducing metal active sites into N abundant substrates is often used to achieve the high-performance oxygen evolution reaction (OER) electrocatalysts²⁷⁻²⁹. In photocatalysis, tuning the semiconductors' conduction band to positive positions can be an efficient way for achieving visible-light-driven water oxidation^{20,30,31}.

Polymeric carbon nitride rises as an intriguing candidate for various applications such as photo-/electrocatalytic water splitting, due to its low-cost precursor, facile synthetic process, N abundant structure, and favorable band position for hydrogen evolution as a semiconductor³²⁻³⁷. In electrocatalysis, the nitrogen-abundant structure of carbon nitride provides a high amount of coupling sites for guest metals, allowing it to act as support materials to construct M-N_x

Chapter 1. Introduction

active sites^{6,21}. M-N_x active sites have recently shown tremendous potential in various electrocatalytic reactions, including electrocatalytic hydrogen and oxygen evolution (HER and OER)^{28,38-41}. In photocatalytic applications, polymeric carbon nitrides (CN) have a suitable bandgap width, negative valence band position and excellent photostability, which exhibits high activity working as visible-light-driven hydrogen generation catalyst.^{23,42,43}

However, carbon nitride also has its shortcomings in these applications. For electrocatalysis, the relatively low conductivity and electrochemical stability of carbon nitride largely limit its performance; therefore, to reach a higher activity, it is usually mixed with carbon materials^{21,40}. As a photocatalyst, carbon nitride's valence band position is usually not positive enough, which limits its potential in water oxidation. Meanwhile, the low crystallinity of melon-condensed carbon nitride leads to defects in the structure, resulting in worse charge separation in the semiconductor^{23,33,44}.

Poly(heptazine imide) (PHI) is an ionic carbon nitride. Unlike polymeric carbon nitride condensed by heating, *e.g.*, urea or cyanamide, PHI is prepared by salt-melt assisted condensation of triazole or tetrazole⁴⁵⁻⁴⁷. While in polymeric carbon nitrides, heptazine units are connected by amine bridges, in PHI, the heptazine units are linked by imides, whose charge is counterbalanced by metal cations introduced by the salt template⁴⁴. The negatively charged nitrogen sites remarkably enhance the charge mobility of the material and allow the structure to host various metals as counterions, yielding an excellent dispersion and periodicity within the structure^{33,48,49}. This unique structural feature of PHI makes it a promising support material that can disperse and stabilize highly efficient active sites^{28,43,49}. Therefore, developing a universal method to introduce different metal cations into the PHI backbones, and exploring their possible catalytic activity becomes an interesting topic.

In this thesis, a facile salt-template-assisted method is developed, to introduce various transition and noble metals into the PHI structure (generally denoted as PHI-M) in controllable type and amount. The structures of these PHI-M's were studied by various techniques, such as XRD, NMR, EPR, XPS, XAFS, STEM, EDX, revealing the distribution of the metal cations. The catalytic activity of several PHI-Ms are further studied in-depth: cobalt intercalated PHI (PHI-Co) was utilized as electrocatalysts for oxygen evolution reaction (OER) and exhibit remarkable OER activity; moreover, this PHI-Co also showed high efficiency in photocatalytic water

oxidation, which stands among the best water oxidation catalysts reported. A nickel intercalated PHI (PHI-Ni) presented efficient hydrogen evolution activity, showing the potential to match with PHI-Co as tandem catalysts towards photocatalytic overall water splitting.

1.2 Structure of the thesis

The first chapter of this thesis is an introduction that briefly reviews the recent development of photo-/electrocatalytic water splitting and the major challenges these fields currently face. As a promising solution to some of the critical problems in photocatalytic water splitting, ionized carbon nitride is introduced to the reader. PHI's structural advantages are depicted, and some successful applications of the metal intercalated PHIs are summarized. After the overview of the structure and properties of these catalysts, the techniques to evaluate the structure of the catalysts and the crucial parameters for evaluating the catalytic activity are introduced.

The second chapter focuses on the preparation and characterization of cobalt intercalated PHI (PHI-Co), furthermore, its electrocatalytic performance in the oxygen evolution reaction (OER) is explored. The working mechanism and reaction kinetics are discussed in this chapter to elucidate the efficient oxidation activity of PHI-Co.

The third chapter further explores the photocatalytic water oxidation activity of PHI-Co. This chapter focuses on the unique optical properties of PHI-Co, which lead to the excellent photocatalytic water oxidation property.

The fourth chapter is a further extension based on the previous chapter. Another transition metal cation, Ni, is introduced to the PHI polymeric lattice, which leads to an efficient catalyst for photocatalytic hydrogen evolution. The structural and optical properties and the photoactivity of the PHI-Ni are studied in this chapter and compared with PHI-Co and transition-metal-free PHI.

The fifth chapter summarizes the other transition-metal-, noble-metal-, and bi-metal-intercalated poly(heptazine) imides that were synthesized. The crystallinity and chemical structures of these PHI-M's are analyzed. Meanwhile, the optical bandgap of several PHI-M's

are calculated, confirming that intercalating different cations can tune the band positions of PHI-M's.

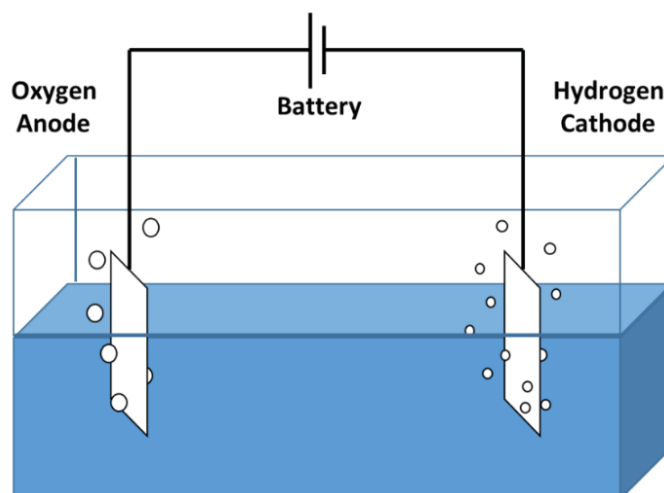
The aforementioned results and conclusions are summarized in the sixth chapter. A detailed description of the experimental section, including the material preparation, characterization with measuring parameters, and some calculations mentioned in the thesis, are provided in the seventh chapter.

1.3 Overall water splitting

1.3.1 Electrolysis: development and challenges

Electrocatalytic water splitting, also known as electrolysis, is one of the oldest and well-known methods to produce hydrogen⁵⁰⁻⁵⁴. In the early 19th century, van Troostwijk and Deiman noticed that when attaching two wires to each side of a battery and placing the other ends of the wires in a container filled with water, on the tip of the two wires the generation of two types of gases, namely hydrogen and oxygen, can be observed⁵⁵. The process is schematically shown in **Scheme 1-1**.

This simple but unprecedented experiment revealed a unique feature of electrocatalytic water splitting, that is, the two half-reactions of photon reduction and water oxidation happen separately on two electrodes. More specifically, in an electrolytic cell, the cathode part involves the hydrogen evolution reaction (HER), and the anode part the oxygen evolution reaction (OER)^{17,56,57}.



Scheme 1-1 Schematic diagram of an electrochemical water splitting system.

The reaction steps of water electrolysis are varied in different reaction conditions and highly dependant on the pH value of the electrolytes. Usually, in acidic conditions, the H^+ in the electrolyte is reduced to H_2 . Meanwhile, the H_2O molecules are oxidized into O_2 . In alkaline conditions, the hydroxyl groups (OH^-) are oxidized and transformed into H_2O and O_2 , while the H_2O is reduced to form H_2 ⁵⁵. The half-reactions on each electrode in different conditions are listed below in **Table 1-1**.

Table 1-1 The half-reactions on each electrode and their corresponding equilibrium half-cell potentials^{58,59}.

Reaction condition	Electrode	Reactions on corresponding electrode	Equilibrium half-cell potentials (1 atm and 25 °C)
Acid (pH=0)	Cathode	$4H^+ + 4e^- \rightarrow 2H_2$	$E_c^0 = 0 \text{ V}$
	Anode	$2H_2O \rightarrow O_2 + 4H^+ + 4e^-$	$E_a^0 = 1.23 \text{ V}$
Alkaline (pH=14)	Cathode	$4H_2O + 4e^- \rightarrow 2H_2 + 4OH^-$	$E_c^0 = -0.83 \text{ V}$
	Anode	$4OH^- \rightarrow O_2 + 2H_2O + 4e^-$	$E_a^0 = -0.40 \text{ V}$

Chapter 1. Introduction

As the two half-reactions of overall water splitting are separated on two different electrodes in the electrolytic cell, in practice, the water electrolysis process requires two different catalysts to facilitate both half reactions^{55,60}.

Noble metals, such as Pt and Pd are the best performing HER electrocatalysts, owing to their low overpotential⁶¹. However, due to the high price and scarcity of noble metals, tremendous effort has been paid to develop noble-metal-free HER electrocatalysts^{60,62,63}. Several transition-metal-based electrocatalytic systems are proved to be also efficient as HER catalysts. Commonly used transition metals, such as metallic Co, Ni, Fe, Cu, their carbides, nitrides, sulfides, and carbon featuring M-N_x catalysts (where M stands for transition metal atoms) often show competitive HER activity comparing to noble-metal-containing HER catalysts⁶⁴⁻⁶⁸. A few non-metal heteroatom-doped nanocarbons, such as S doped graphene, P, N co-doped mesoporous carbon (PNMC), graphitic carbon nitride (g-C₃N₄), and black phosphorus, are also active HER catalysts⁶⁹⁻⁷². The activities of some earth-abundant HER catalysts are summarized in **Figure 1-1** and compared with the activity of commercial Pt/C (20wt%) electrocatalyst⁷¹⁻⁷⁹.

For the OER process, noble-metal-containing electrocatalysts, such as IrO₂, RuO₂, are actually still superior to all other materials in terms of low overpotential and high stability at all pH values^{80,81}. Meanwhile, various transition metal oxide/hydroxide catalysts, such as perovskite (ABO₃, where A stands for alkaline- and/or rare-earth metals, B stands for transition metals), layered hydroxide (LDH) have shown activity and stability as OER catalysts⁸²⁻⁸⁵. Many non-oxide transition metal-containing catalysts, such as metal chalcogenides, metal pnictides, metal coordination complexes, have presented the potential to act as efficient OER catalysts⁸⁶⁻⁹⁰. Herein, η_{10} (overpotential at current density of 10 mA cm⁻²) is again applied as the descriptor, to compare the activities of some earth-abundant OER catalysts with IrO₂ nanoparticles (**Figure 1-2**)^{83, 91-97}.

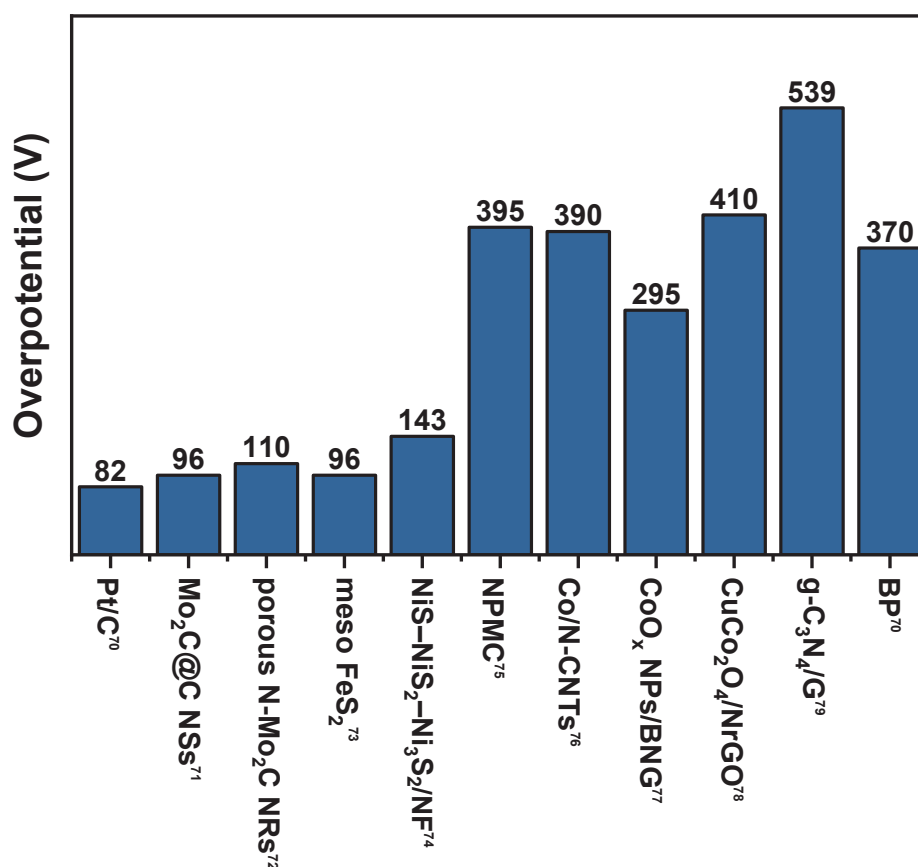


Figure 1-1 Activity of some representative earth-abundant catalysts comparing with the Pt catalyst, using η_{10} (overpotential at current density of 10 mA cm^{-2}) as the descriptor^{70–79}. Please note that the HER activities in this figure are all measured in 0.1 M KOH electrolyte. *The abbreviation NPMC in the figure stands for N, P-doped mesoporous carbon, and BP stands for black phosphorus.

Furthermore, researchers in this field have tried to combine the properties of both HER and OER catalysts and construct efficient bifunctional catalysts^{17,98,99}. These bifunctional electrocatalysts, such as Ni(OH)₂/Ni₃S₂ heterogeneous nanosheets¹⁰⁰, hollow iridium-silver nanotubes¹⁰¹, Ni and Mo₂C nanoparticles loaded nitrogen-doped carbon nanofibers (NCNFs)¹⁰², exhibit activity on both anode and cathode for overall water splitting.

Despite years of study in electrolysis, the technique has not yet been widely used in industry¹⁰³. One of the major challenges in developing high-performance water electrolyzers is to optimize the OER process. OER is a multi-step reaction with a four-electron transfer process (**Table 1-1**)¹⁰⁴. Only one electron transfers per step, leading to the very slow kinetics of the OER

process^{58,59}. Moreover, each step of this reaction requires its own activation energy. As the activation energy of each step accumulates, the OER process often requires a very high overpotential. Therefore, seeking high-performance OER electrocatalysts is still an urgent task¹⁷.

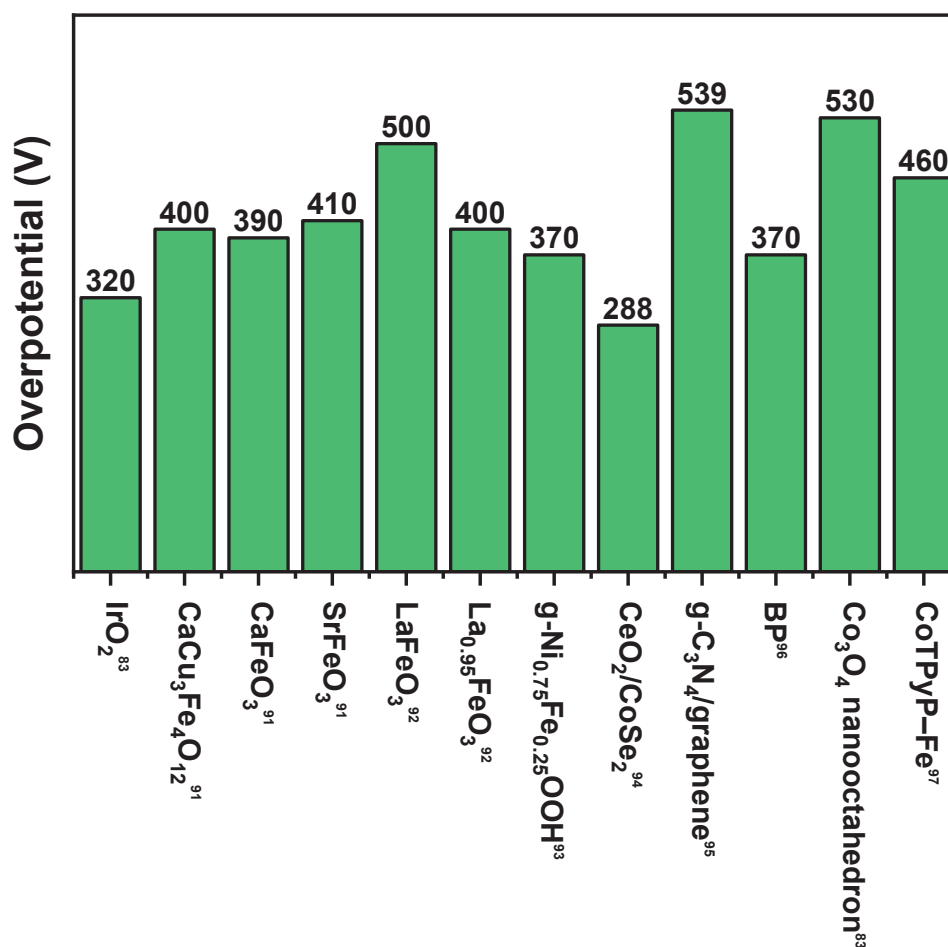


Figure 1-2 Activity of some representative earth-abundant catalysts comparing with IrO_2 and RuO_2 catalyst, using η_{10} (overpotential at current density of 10 mA cm^{-2}) as the descriptor^{83,91-97}. Please note that the OER activities in this figure are all measured in 0.1 M KOH electrolyte. *The abbreviation BP in the figure stands for black phosphorus.

1.3.2 Photocatalytic overall water splitting and its major challenges

Photocatalytic overall water splitting is a relatively young field compared to electrolysis. The phenomenon was first observed by Fujishima and Honda in 1972 when they applied TiO₂ as an electrode in an electrochemical cell. They illuminated the TiO₂ with short-wavelength light, and obtained H₂ and O₂ in lower overpotential¹⁰⁵. The experiment confirmed that semiconductor photocatalysts can be used to split water. In the past 50 years, photocatalytic water splitting draws an increasing amount of attention due to the advantages of this technique: this process converts solar light and water, the most abundant and clean resource on earth, into hydrogen, which has a high energy yield and is pollution-free^{16,106,107}.

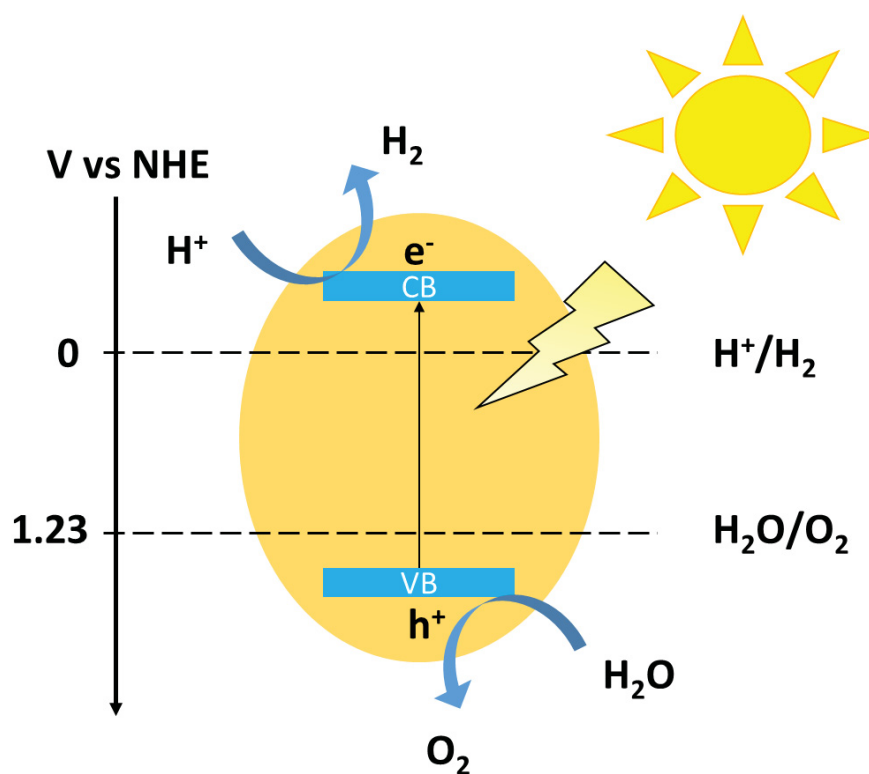
The working mechanism of photocatalytic water splitting is schematically shown in the following **Scheme 1-2**. The reaction process can be summarized as follow. When light irradiates a semiconductor with a proper bandgap width, the electron in its valence band can be activated by the energy of the photon and transition to the conductive band, generating photo-induced electron-hole pairs. The photo-induced electron and holes can be separated and gradually transfer to the surface of the catalyst, on which the electrons are taking part in the hydrogen reduction. While holes take part in water oxidation¹⁰⁸.

Based on its working mechanism, a successful photocatalytic water splitting system needs to fit in the following requirements:

A) Suitable bandgap width. The bandgap width is the energy difference between the valence band maximum and conduction band minimum of the semiconductor¹⁰⁹. Essentially, the energy of a photon (E) and the wavelength of the light (λ) follows the equation below:

$$E=hc/\lambda \quad (1-1)$$

where h is Planck's constant and c is the speed of light. When the incident light provides energy (E) no less than the bandgap width (E_g), the electrons can transfer from the valence band to the conduction band and serve as charge carriers¹¹⁰. According to **equation 1-1**, semiconductors with narrower bandgaps can utilize incident light with longer wavelength and lower energy. However, in order to catalyze the overall water splitting reaction, the bandgap width of a semiconductor also should not be smaller than 1.23 eV. Efficient photocatalysts usually have a bandgap width in the region of 2.0-3.0 eV^{34,111}.



Scheme 1-2 Working mechanism of photocatalytic overall water splitting.

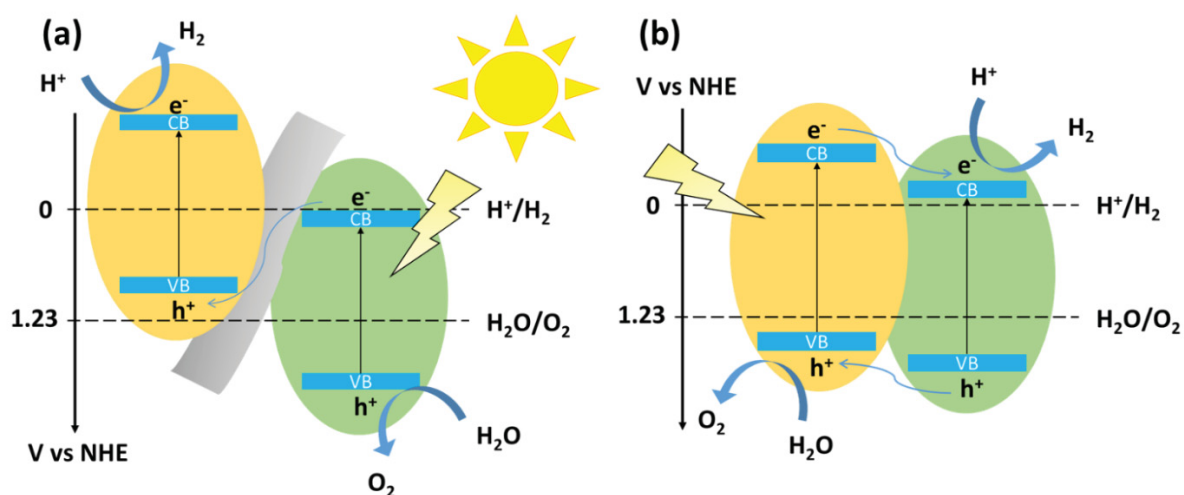
B) Favorable band positions. In neutral conditions at room temperature, the photon reduction potential is defined as 0 V vs NHE, and the water oxidation potential is 1.23 V vs NHE¹¹². Therefore, it is essential that the conduction band minimum (CBM) of the semiconductor should be more negative than the reduction potential, and the valence band maximum (VBM) more positive than the oxidation potential.

C) Easy charge separation. The photo-induced electron-hole pairs often recombine quickly after they were generated, which vastly reduces the quantum yield of the catalyst. Hence, promoting the charge separation is also crucial for promoting the photocatalytic activity¹¹³.

Photocatalytic systems active for overall water splitting can be designed by two different approaches: one-step overall water splitting and two-step water splitting. One-step overall water splitting uses one single semiconductor as the photocatalyst. The photocatalyst should have a suitable thermodynamic potential for catalyzing both, hydrogen evolution and water oxidation,

a sufficiently narrow bandgap that absorbs visible light, and stability against photocorrosion⁷. Due to these critical demands, only a few photocatalysts, such as Cu_2O ¹¹⁴, or GaN:ZnO ¹¹⁵ solid solutions, are reported to be active in one-step overall water splitting.

Two-step water splitting can be achieved by forming a Z-scheme or heterojunction structure from two different semiconductors. In a two-step water splitting process, the hydrogen evolution and water oxidation half reactions happen separately on two different photocatalysts^{4,116}. The difference between a Z-scheme photocatalyst and a heterojunction photocatalyst lies in the charge transfer in the photocatalytic system. The basic structure and working mechanism of two-step water splitting photocatalysts are depicted in **Scheme 1-3**.



Scheme 1-3 Schematic structure of (a) Z-scheme photocatalytic system and (b) heterojunction photocatalytic system.

A Z-scheme is a structure inspired by natural photosynthesis in green plants (**Scheme 1-3a**)¹¹⁷. The structure consists of a photocatalyst for H_2 generation and another photocatalyst for water oxidation. Meanwhile, a shuttle redox couple or conducting layer is introduced to the system for charge carrier transport in between the two photocatalysts.

During the photoreaction, the photo-induced electrons in the semiconductor with the higher conduction band position will participate in H_2 generation, while the holes in the semiconductor with the lower valence band position will participate in water oxidation^{118–120}. In the meantime,

Chapter 1. Introduction

the electrons in the semiconductor with the lower conduction band position will recombine with the holes from the semiconductor with the higher valence band position. A key advantage of the Z-scheme structure is that it has less limitation on the band position of the semiconductors⁷. For instance, WO_3 , as a highly efficient water oxidation photocatalyst, is unable to reduce water to hydrogen due to its conduction band position. However, it can be used as the photocatalyst for water oxidation in Z-scheme photocatalytic system¹¹⁷.

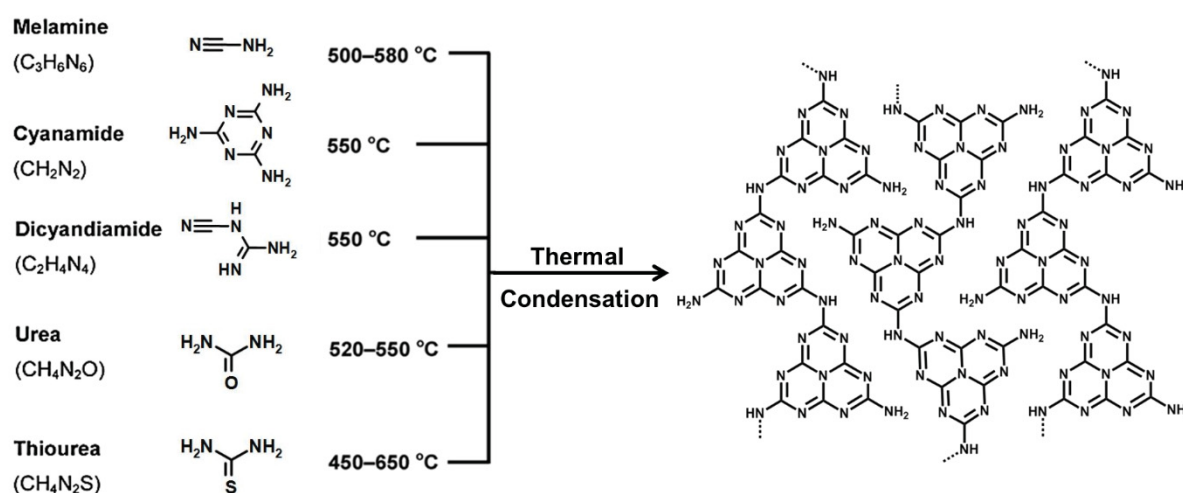
Heterojunction photocatalysts are made by two semiconductors directly in contact with each other (**Scheme 1-3b**). The band structures of the two semiconductors align with each other with a type-II band alignment⁶. The photo-induced electrons accumulate in the semiconductor with the lower conduction band minimum and participate in the H_2 generation. The holes transfer to the semiconductor with the higher valence band maximum and take part in water oxidation¹²¹⁻¹²⁴. Due to its working mechanism, in a heterojunction photocatalytic system, both semiconductors need to have conduction band minima (CBM) more negative than the hydrogen generation potential while the valence band maxima (VBM) must be more positive than the water oxidation potential. Over the years, some heterojunction photocatalysts for overall water splitting, such as $\text{Co}_3(\text{PO}_4)_2/\text{g-C}_3\text{N}_4$, are reported¹²⁵.

To achieve efficient overall water splitting, several challenges still need to be solved urgently, such as promoting electron transfer between two semiconductors and suppressing the backward reactions. But most importantly, despite many efficient photocatalysts that have been developed for hydrogen evolution^{5,126}, optimizing photocatalytic water oxidation is relatively underdeveloped^{25,127}. So far, the active catalysts for photocatalytic water oxidation, such as BiVO_4 , WO_3 , and Bi_2WO_6 , are often toxic and require complicated synthetic processes^{20,31,122,128,129}. Therefore, heavy metal-free, low-cost, and high-performance photocatalyst for visible-light-driven water oxidation is still in high demand for achieving overall water splitting.

1.4 From carbon nitrides to poly(heptazine) imides

1.4.1 Carbon nitrides

Polymeric carbon nitride (CN) is a well-known visible-light photocatalyst^{130–132}. Polymeric carbon nitrides are usually produced by the condensation of nitrogen-rich precursors such as melamine, dicyandiamide, cyanamide or urea¹³³. The synthetic process of polymeric CN is shown below in **Scheme 1-4**.



Scheme 1-4 Synthesis of polymeric carbon nitrides.

Carbon nitride is one of the oldest artificial polymers people managed to synthesize¹³⁴. The earliest literature demonstrating the synthesis of melon-condensed carbon nitride can be traced back to 1834¹³⁵. The very first application of carbon nitride as a heterogeneous catalyst was reported in 2006¹³⁶, as metal-free catalyst for sustainable Friedel–Crafts reactions in very mild conditions. The 'golden age' for carbon nitrides started in 2009, by the time the first report on carbon nitrides photocatalysts for H₂ evolution was published⁴⁵. Polymeric carbon nitride can be prepared via facile synthesis with low-cost, abundant precursors. Its band position is favorable for photocatalytic hydrogen evolution. Due to these properties, carbon nitride has received an increasing amount of attention in various photocatalytic applications, *e.g.*, degradation of organic pollutants, water splitting, CO₂ reduction, N₂ fixation^{137–140}.

Chapter 1. Introduction

Carbon nitride has also caught the attention of an adjacent field: electrocatalysis^{35,36,141}. Carbon featuring M-N_x catalysts are noble-metal-free, high-performance electrocatalysts^{39,41,142,143}. Usually, an M-N_x-C catalyst is a transition metal intercalated nitrogen-doped carbon system^{26,144,145}. It was reported that in such a system, metal species interact synergistically with nitrogen atoms to modify the local electronic structure of the catalyst and consequently optimize the surface adsorption of intermediates^{39,142}. However, in a classical carbon featuring metal-N_x system, the amount, dispersion, and type of the nitrogen dopant in the carbon matrix is relatively difficult to identify and control, which causes difficulties in monitoring the content and dispersion of the metal-N_x active sites¹⁴⁶. In this respect, carbon nitride, as a nitrogen-abundant material, with structurally defined nitrogen sites and electron-abundant structure, can host the metal species, and therefore, become a supreme anchor for constructing M-N_x-C catalysts^{6,21}.

However, despite all these tempting properties, practical applications of carbon nitride are still limited by several shortcomings of pristine carbon nitride. For photocatalysis, pristine carbon nitride suffers from the high recombination rate of charge carriers, abundant surface defects, narrow light-absorbance region in the visible-light spectrum, hence, usually presents low activity in photocatalytic applications^{23,33,44}. In the electrochemical cell, carbon nitride shows low electrical conductivity and relatively low stability, which makes it unable to work independently as an M-N_x catalyst supporting material^{21,40}.

Various strategies have been developed to optimize the activity of pristine carbon nitrides. At a molecular scale, copolymerization and doping are effective approaches to introduce dopants into the carbon nitride matrix in order to modify the electronic structure and tune the band of polymeric CN^{34,147}.

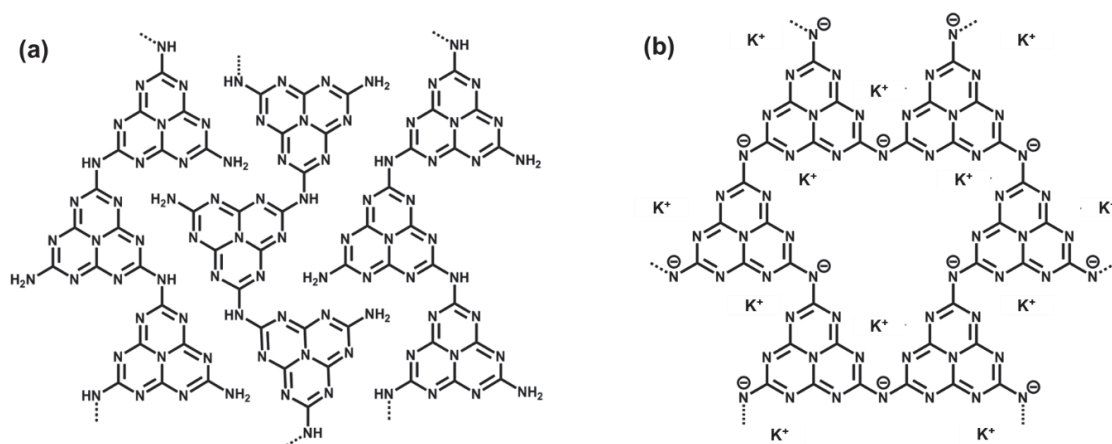
Nanostructure design has also be applied to improve the catalytic activities of carbon nitrides and many different approaches were explored. Soft templating, hard templating, supramolecular preorganization and exfoliation strategies are used for synthesizing polymeric carbon nitrides with different morphologies. Combining carbon nitride with various semiconductors, metallic co-catalysts, conductive layers, was also studied to obtain carbon nitride-based photocatalysts^{133,134,148,149}.

1.4.2 Poly(heptazine) imides

In order to improve the activity of pristine carbon nitrides, different approaches are reported to tailor the molecular structure of polymeric carbon nitride^{43,44,150,151}. Poly(heptazine) imide is one of the structurally tailored carbon nitrides. Due to the higher crystallinity, enhanced electronic conductivity, narrower bandgap width, organic zeolite nature and long-live photoinduced radicals, PHI has been used in multiple applications, such as H₂ evolution, halogenation of aromatic hydrocarbons, charge storage, or photocatalytic Kindler reaction^{28,43,152}.

PHI is prepared by salt-melt-assisted condensation^{45–47}. A eutectic mixture of LiCl and KCl is often used as the salt template. Precursors such as 3,5-diamino-1,2,4-triazole, 3-amino-1,2,4-triazole-5-thiol, and 5-aminotetrazole are mixed with LiCl/KCl salt template, and calcined at 550°C in argon flow to obtain PHI powders^{44,152}. There are also reports demonstrating that, the highly crystallized PHI can be synthesized via ampoule synthesis with a mixture of dicyandiamide, KSCN and potassium melonate penta-hydrate¹⁵³.

Unlike the polymeric carbon nitride, whose heptazine units are connected by amine bridges, PHI consists of heptazine units linked by imides bridges⁴⁴. The salt-melt-assisted synthesis introduces a large number of K cations to the PHI structure, which counterbalances the negative charge from the imide bridges in the PHI backbone^{23,44,147,150,151}. The structural difference of PHI and polymeric CN is schematically shown in **Scheme 1-5**.



Scheme 1-5 Structure of (a) polymeric CN and (b) PHI.

Chapter 1. Introduction

The K cations in PHI can be easily exchanged by protons when treated with hydrochloric acid solutions, forming a protonated PHI-H^{49,153}. The removal of K ions from the PHI structure is reversible, and treatment of PHI-H with KOH solution yields again the K intercalated PHI, which shows a very similar structure as the original PHI⁴⁹. Moreover, Savateev *et. al.*, successfully intercalated a variety of s- and d-metal cations by dispersing PHI powder in a solution of the desired metal salt⁴⁹. The exchange of the metal cations is driven by the concentration gradient of metal ion concentrations in the solid structure and in the solution, and after the ion exchange process, the crystal structure of PHI preserves well in many of the obtained products.

The results from Savateev *et. al.* reveals an intriguing possibility that PHI can be used to disperse and stabilize various metal active sites of atomic level. This makes PHI a promising substrate material for designing highly efficient catalysts⁴⁰.

However, the post-synthesis ion exchange method usually requires a time-consuming dialysis process, which is also influenced by the pH value of the salt solution. Besides, the ion exchange process cannot efficiently control the amount of introduced metal cations. In the meantime, when treated with some metal salt solution, such as CoCl₂, a remarkable change in the crystal structure of the obtained PHI can be observed⁴⁹.

In this thesis, a modified salt-template-assisted method is developed to control the amount of metal cations introduced in the PHI structure. By altering the composition of metal salts in the salt template, the types and amounts of metal cations in the PHI backbone can be easily modified in the final product, meanwhile, the basic structure of PHI can be well-preserved²⁸. In the following chapters, a selection of transition-metal-, noble-metal-, and bi-metal-intercalated PHI are synthesized via the modified salt-template assisted method, among them, Co- and Ni-intercalated PHI (PHI-Co and PHI-Ni) can serve as high-performance electro- and photocatalysts.

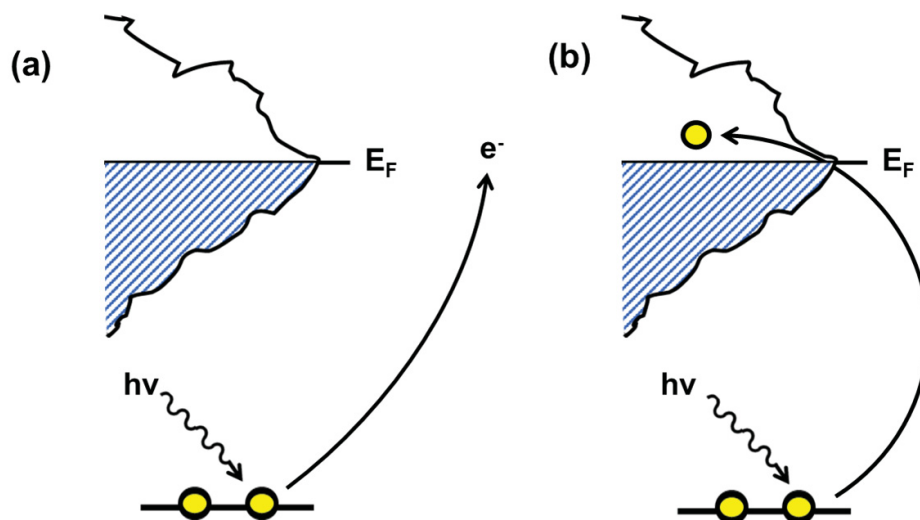
1.5 Characterizing the structure of catalysts

1.5.1 X-ray photoelectron spectroscopy (XPS)

X-ray photoelectron spectroscopy (XPS) is a surface-sensitive spectroscopic technique that collects the photoelectrons emitted from the material excited by X-ray sources and studies the kinetic energy of the photoelectrons. Therefore, XPS can obtain the energy levels of atomic core electrons¹⁵⁴. The measurement is widely applied to identify the elements on the surface of the samples and their chemical states. When paired with ion-beam etching, the technique can also be applied for in-depth profiling of the sample. The results of XPS can offer an overview of elemental composition over the surface of the material. In the meantime, XPS can also identify the oxidation state of the atoms and the coordination of elements^{38,155,156}. Hence, XPS is considered a powerful characterization technique for understanding the chemical structure of the materials. Additionally, XPS also provides the overall electronic structure in the samples, as the offset edge of XPS spectra can be used to calculate the semiconductors' valence band maximum¹⁵⁷.

1.5.2 X-ray absorption spectroscopy (XAS)

X-ray absorption spectroscopy (XAS) is another photoemission spectroscopy, which also collects excited photoelectrons obtained by irradiating a material with a beam of X-rays. Unlike XPS measurement, where the core electron is ionized, in XAS, a core electron is excited into unoccupied orbitals above the Fermi level (**Scheme 1-6**). Therefore, XAS can provide unique structural information of the measured samples¹⁵⁸.



Scheme 1-6. The excitation of photoelectrons in (a) XPS and (b) XAS measurements¹⁵⁸

XAS can be divided into two regimes. Extended X-ray absorption fine structure (EXAFS), where the outgoing electron is well above the ionization range, provides the oxidation states of the target element in the tested materials. X-ray absorption near-edge structure (XANES) is in the low energy range, which helps understand the coordination between the target atoms and their adjacent atoms^{159–162}. The measurements of XAS are usually performed at synchrotron radiation facilities, which provide intense and tunable X-ray beams. However, in recent years, the miniaturization of XAS setups is making significant progress.

The XAS measurements in this thesis were carried out with a self-developed small-size wavelength-dispersive spectrometer in von Hámos geometry¹⁶³. The spectrometer is equipped with a microfocus 30 W Mo X-ray tube, a curved Highly Annealed Pyrolytic Graphite mosaic crystal with a bending radius of 300 mm and a thickness of 20 μm , and a hybrid photon counting CMOS detector of the type EIGER R 500K by Dectris with 512 x 1030 pixel and a pixel size of 75 μm \times 75 μm . The tube was operated with a high voltage of 14.8 kV and a current of 1905 μA .

1.5.3 Scanning transmission electron microscopy (STEM)

A scanning transmission electron microscope (STEM) is a type of transmission electron microscope (TEM). In such a microscope, analytical techniques such as Z-contrast annular dark-field imaging can be applied, and, therefore, suitable for observing atoms in the structure in a very high resolution. Therefore, STEM is often used to spot the size and dispersion of metal atoms/clusters in the structure of the samples or obtaining the crystal structure of highly crystallized samples^{40,164,165}. STEM can also be coupled with spectroscopic mapping by energy-dispersive X-ray (EDX) spectroscopy or electron energy loss spectroscopy (EELS) to detect the composition and dispersion of the elements in a specific area of the measured materials. These signals can be obtained simultaneously, allowing direct correlation of images and spectroscopic data^{43,166}.

1.6 Important parameters for evaluating electrocatalytic and photocatalytic activities

1.6.1 Overpotential

In an electrolytic cell, it usually requires more energy than thermodynamically expected to drive the desired reaction. The overpotential is the potential difference between a half-reaction's thermodynamically determined reduction/oxidation potential (for OER, 1.23 V vs RHE) and the potential where the electrochemical reaction is observed. For an easier comparison between different works, in practice, the overpotential usually derives from the potential ($E_{j=10}$ vs RHE), where current density reaches $j = 10 \text{ mA cm}^{-2}$. The overpotential for OER is calculated as $E_{j=10}$ (vs RHE) minus 1.23 V (vs RHE). In general, a catalyst with an overpotential in the range of 300-400 mV can be considered already as an excellent catalyst for OER^{55,82}.

1.6.2 Tafel slope

Tafel slope is a crucial parameter from the Tafel equation (eq1), which provides multiple

important information in electrochemical kinetics¹⁶⁷.

$$\eta = A \cdot \log (j/j_0) \quad (1-1)$$

In this equation, A represents the Tafel slope, η stands for overpotential, j is the current density, and j_0 is the exchange current density. This equation is the mathematic expression of the first linear part of the Tafel plot, extracted from the polarization curve by setting the X-axis as Log j (where j stands for current density) and Y-axis overpotential.

The Tafel equation relates the rate of an electrochemical reaction to the overpotential, which makes the Tafel slope an essential parameter for comparing the kinetics between different catalysts. The range of values of the Tafel slope can also help identify the rate-determining step. In general, a smaller Tafel slope represents faster kinetic in an electrochemical reaction^{39,55,168}.

1.6.3 Turnover frequency (TOF)

Turnover frequency (TOF) is a valuable parameter to evaluate the specific activities of the active centers and, therefore, often applied to compare catalysts with similar composition but different nano-/molecular structure^{27,28,164,169}.

The turnover number (TON) represents the maximum use that can be made of a catalyst/catalytic center for a specific reaction under certain conditions. The TON can be calculated via moles of desired product formed divided by the number of active centers.

The turnover frequency (TOF) quantifies the specific activity of a catalytic center for a specific reaction under certain reaction conditions per unit time. The TON and TOF fulfill a simple mathematic relation of $TON = TOF \cdot \text{reaction time}$.

In an electrochemical process, the TOF can also be calculated from the equation below:

$$TOF = j/\alpha NF \quad (1-2)$$

where j is the current density, α is 4 for OER due to the four-electron reaction, F is Faraday constant, and N is the molar concentration of active sites.

1.6.4 UV-vis spectroscopy

Ultraviolet-visible (UV-Vis) spectroscopy is an important technique applied to study the light absorption/diffraction of the materials. In UV-Vis spectroscopy, light with a series of wavelengths in the UV or/and the visible spectrum is applied to illuminate the sample. The transmitted or diffracted light signals (depending on whether the material is transparent) are collected to understand the region and intensity of the incident light that the sample can absorb.

In photocatalysis, the UV-vis study can estimate the optical bandgap width of the catalysts^{6,170}. To be absorbed by the semiconductor, a photon should own the energy which at least matches or is higher than the bandgap to promote the semiconductor from the ground state to the excitation state. Therefore, the absorbance edge of the UV-vis spectra is correlated to the bandgap width of the semiconductor.

1.6.5 Photoluminescence spectroscopy

Photoluminescence spectroscopy is a technique probing the photoluminescence in materials. Photoluminescence (PL) is light emission from the material after absorbing photons. The absorption of photons leads to the electrons from the valence band transit to the higher energy level. This process is called excitation. Following the excitation of materials, various relaxation processes can occur, resulting in a recombination of photo-induced electron-hole pairs. In photocatalytic reactions, such a recombination is undesired, as the recombination of photo-induced electron-hole pairs decreases the quantum yield efficiency of the catalysts^{6,49}.

Therefore, by introducing photoluminescence spectroscopy, the charge separation and recombination can be evaluated in photocatalysts, which helps to understand the working mechanism of the catalysts^{152,171–173}.

1.6.6 Band position

The band position of semiconductors has a direct influence on their catalytic activity. The band position includes three parameters: bandgap width (E_g), valence band maximum (E_{vb}) and conduction band minimum (E_{cb}). Knowing the band position of a semiconductor can help

Chapter 1. Introduction

understand the working mechanism of the photocatalyst.

In neutral conditions at room temperature, the photon reduction potential is defined as 0 V vs NHE, and the water oxidation potential is 1.23 V vs NHE. Therefore, it is crucial that the conduction band minimum (CBM) of the semiconductor more negative than the reduction potential and the valence band maximum (VBM) more positive than the oxidation potential^{6,170,172}.

The bandgap width can be calculated via the Tauc plot, which is derived from the UV-Vis absorbance measurements. Typically, a Tauc plot shows the $h\nu$ on the abscissa, where h is Planck constant, ν is the frequency of light. The calculation of ν follows the equation below:

$$\nu = c/\lambda \quad (1-3)$$

Where c is the speed of light and λ is the absorbance wavelength from the UV-vis spectra. On the other hand, the ordinate of the Tauc plot can be written as $(\alpha h\nu)^{1/r}$, where α is the absorption coefficient, which can often be substituted by $F(R)$ in the UV-vis spectrum. $r = 1/2$ for direct bandgap semiconductors.

After the bandgap width (E_g) is obtained, the next step for calculating the semiconductor's band position is to confirm the position of the valence band maximum (E_{vb}). This value can be gained from X-ray photoelectron spectroscopy (XPS).

The -2~10 eV region spectra of XPS can also provide information of the valence band maximum of photocatalysts relative to the Fermi level. By extrapolating the first linear region of the VBM spectra of the target and compared with semiconductors with known band structure, can be used to calculate the position of valence band maximum (E_{vb}) of the semiconductor can be calculated.

When the bandgap energy (E_g) and the valence band maximum (E_{vb}) are both known, the position of conduction band minimum (E_{cb}) can be calculated via the following equation:

$$E_g = E_{cb} - E_{vb} \quad (1-4)$$

2 Cobalt intercalated poly(heptazine) imide for electrocatalytic oxygen evolution

Motivation

Electrocatalytic water splitting is an environmentally friendly method to obtain hydrogen^{174–176}. Due to the four-electron oxidation process, the oxygen evolution half-reaction (OER) has slow kinetics, which has primarily hampered the development of overall water splitting devices^{145,177,178}. Therefore, searching for high-performance electrocatalysts for OER has become one of the major challenges in electrocatalytic water splitting.

Transition metal-N_x electrocatalysts (M-N_x) show comparable activities to the noble-metal-containing catalysts^{38,41,143}. The M-N_x electrocatalysts are usually synthesized by doping nitrogen atoms in the carbon matrix, and then anchoring the metal species on the nitrogen dopant. The excellent electrocatalytic activities of these catalysts originate from the M-N_x active sites, where the metal species interact synergistically with nitrogen atoms to modify the local electronic structure of the catalyst and consequently optimize the surface adsorption of intermediates^{38,41}. In these classical carbon materials featuring M-N_x-C electrocatalysts, the amount, dispersion, and type of the nitrogen dopant in the carbon matrix is relatively difficult to identify and control, causing difficulties in controlling the amount and dispersion of active sites in the catalysts¹⁴⁶.

Poly(heptazine) imide is an ionic carbon nitride, which contains abundant, structurally defined nitrogen sites and atomically dispersed potassium cations. The potassium cations in the PHI backbone can be replaced by transition metals via the post-synthetic ion-exchange method⁴⁹. This unique structure of PHI makes it a promising substrate for designing M-N_x electrocatalyst. Moreover, PHI shows significantly enhanced electronic conductivity comparing with polymeric carbon nitride^{33,48,49}, which is also favorable for electrocatalysis.

Chapter 2. Cobalt intercalated poly(heptazine) imide for electrocatalytic oxygen evolution

PHI is prepared by the pyrolysis of 5-aminotetrazole with the presence of a eutectic LiCl-KCl salt melt^{44,152}. According to the previous report, metal cations can be intercalated in the PHI structure by dispersing PHI powder in a solution of the desired metal salt⁴⁹. However, this post-synthesis ion exchange method usually requires a time-consuming dialysis process, and cannot efficiently control the amount of introduced metal cations.

Therefore, to gain better control over the amount of the metal active sites in PHI, a modified salt-melt-assisted method is developed. This method provides a facile and reliable approach to embed the desired metal cations into the PHI polymeric lattice during the condensation. By altering the composition of the salt template, the amount of metal cations introduced in the PHI structure can be easily modified.

In this chapter, Co²⁺ cations, as a highly active metal species for OER¹⁸²⁻¹⁸⁴, are introduced to the PHI structure by adding CoCl₂ into the eutectic KCl-LiCl salt mixture during PHI preparation. The PHI-Co electrocatalyst shows enhanced OER activity compared to a cobalt-doped polymeric carbon nitride with an overpotential of 324 mV in 1 M KOH, well comparable to state-of-the-art OER electrocatalysts under similar conditions.

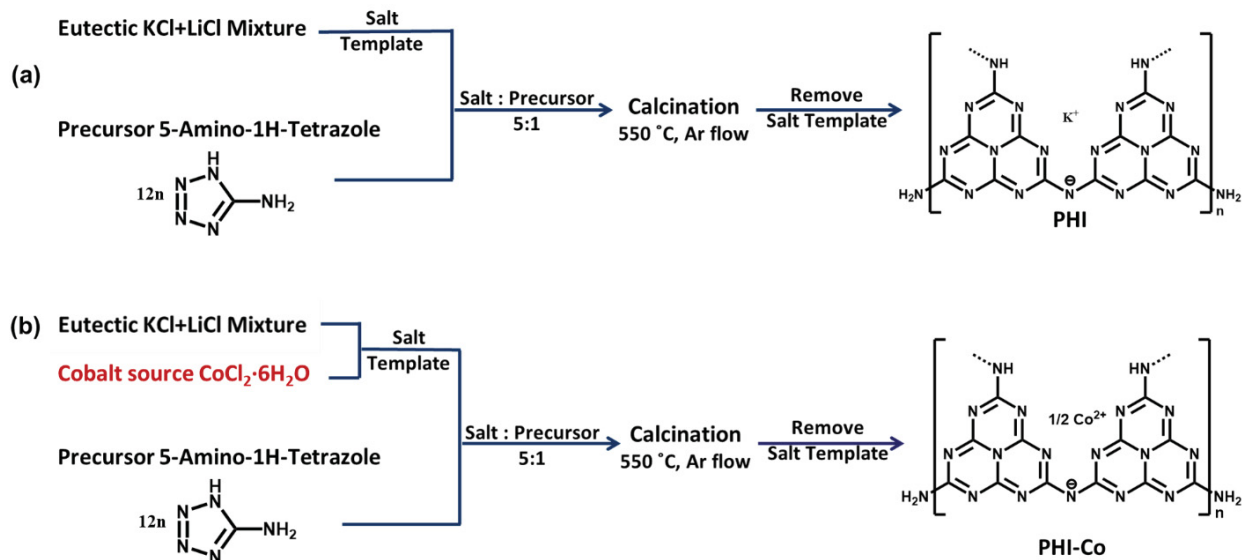
Results and Discussion

The synthesis of the PHI follows the process in **Scheme 2-1a**. In brief, the 5-aminotetrazole precursor is mixed with the salt template, a eutectic mixture of KCl-LiCl. The condensation of tetrazole precursor happens at 550°C in argon flow, with assistance of salt template. The PHI powder can be obtained after the removal of the salt template. Please note that in the as-obtained PHI, potassium cations introduced by the salt template counterbalance the negative charge of imide bridges^{44,152}.

Cobalt intercalated poly(heptazine) imide (PHI-Co) was prepared based on a modified salt-melt-assisted PHI synthesis (**Scheme 2-1b**). Different amounts of CoCl₂ (0.5-5 wt%) were added to the KCl-LiCl mixture to prepare the salt template. This salt template was mixed with the precursor, 5-aminotetrazole. The mixture was then heated at 550 °C for 8 h under argon

Chapter 2. Cobalt intercalated poly(heptazine) imide for electrocatalytic oxygen evolution

flow to obtain the PHI-Co powder (detailed synthesis protocol in **Chapter 7 Experimental Section**).



Scheme 2-1. Typical synthetic process of (a) PHI and (b) PHI-Co via salt-melt-assisted method.

Inductively coupled plasma optical emission spectrometry (ICP-OES) was employed to investigate the amount of Co cations in PHI-Co's (**Table 2-1**). The Co content varied from 0.08-2.61 wt%, when 0.25-5 wt% of CoCl₂ were added to the salt template. In **Table 2-1**, these as-obtained PHI-Co's were noted as PHI-Co-x, where x stands for the Co content (weight percentage) in the PHI-Co sample. The cobalt content in PHI-Co's increases proportionally as the CoCl₂ amount in the salt template increases, concluding that the amount of Co ions can be well controlled by varying the amount of Co source in the salt template. Meanwhile, the K content within the PHIs decreases with increasing Co content (**Table 2-1**), suggesting that the Co ions are partially replacing the K ions in the PHI structure.

Chapter 2. Cobalt intercalated poly(heptazine) imide for electrocatalytic oxygen evolution

Table 2-1 Content of CoCl₂ in the salt template and corresponding content of Co and K in the final PHI's.

Samples	CoCl ₂ in the salt template (wt%)	Co content in samples (wt%)	K content in samples (wt%)
PHI	0	0	1.62
PHI-Co-0.1	0.25	0.08	1.48
PHI-Co-0.2	0.5	0.17	1.29
PHI-Co-0.5	1	0.45	1.05
PHI-Co-0.8	2	0.83	0.83
PHI-Co-1.4	3	1.43	0.85
PHI-Co-2.6	5	2.61	0.79

The crystallinity of the PHI-Co with different cobalt content and the PHI were studied by their X-ray diffraction (XRD) patterns (**Figure 2-1**). In the typical XRD pattern of PHI, the diffraction peak at 8.3° corresponds to the (110) facet, indicating the high periodicity of heptazine units within the layers, and the diffraction peak centered at 27.0° can be ascribed to the (001) facet, corresponding to the interplanar stacking of the layers¹⁵². Several smaller and broader peaks centered at 14.1°, 23.8° and 36.3°, can be assigned to the (120), (011), and (231/321) facets of the well-crystallized PHI structure, respectively¹⁵³. Both diffraction peaks at 8.3° and 27.0° can also be observed in all PHI-Co samples with different Co content, except for PHI-Co-2.6. The crystallinity of PHI-Co significantly decreases with the increase of Co content in PHI-Co. When the cobalt content reaches 2.61 wt%, the crystallinity of PHI-Co can no longer be preserved.

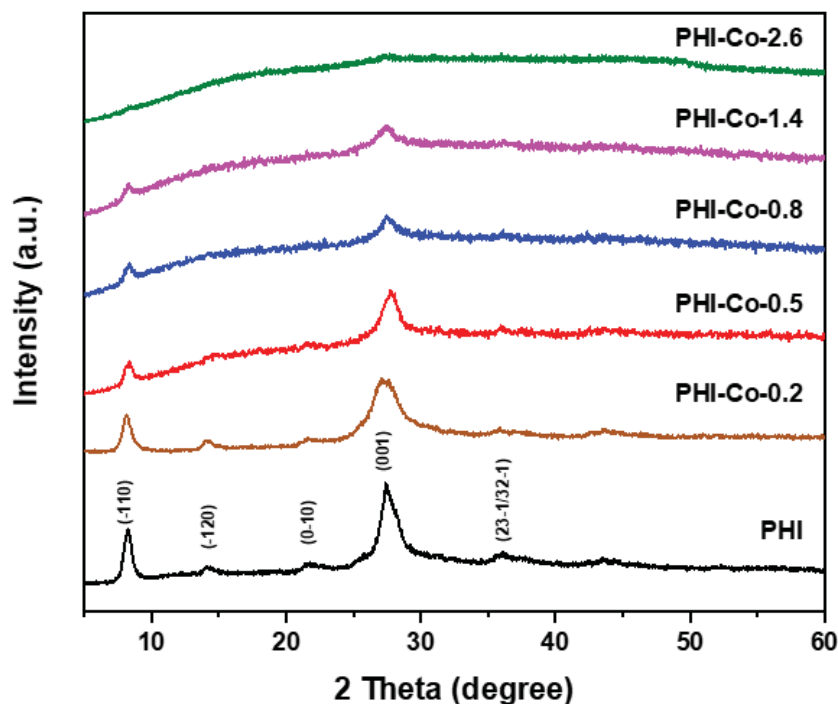


Figure 2-1 XRD patterns of PHI and PHI-Co's with different cobalt content.

The chemical states of elements in PHI-Co are investigated by X-ray photoelectron spectroscopy (XPS, **Figure 2-2**). The doublet peak in the XPS Co 2p spectrum of PHI-Co (**Figure 2-2a**) can be found centered at 780.4 eV with strong satellite features centered at 785.4 eV, indicating that cobalt has an oxidation state of Co(II) in the material¹⁸⁵. The XPS O 1s and Cl 2p spectra of PHI-Co show, no peak of cobalt oxide can be observed (**Figure 2-2b**)¹⁵⁴, nor any hint of Cl remaining in the sample (**Figure S1**). Thus, the cobalt in PHI-Co should mainly exist as the counterion to the anionic imide sites in the polymeric PHI structure.

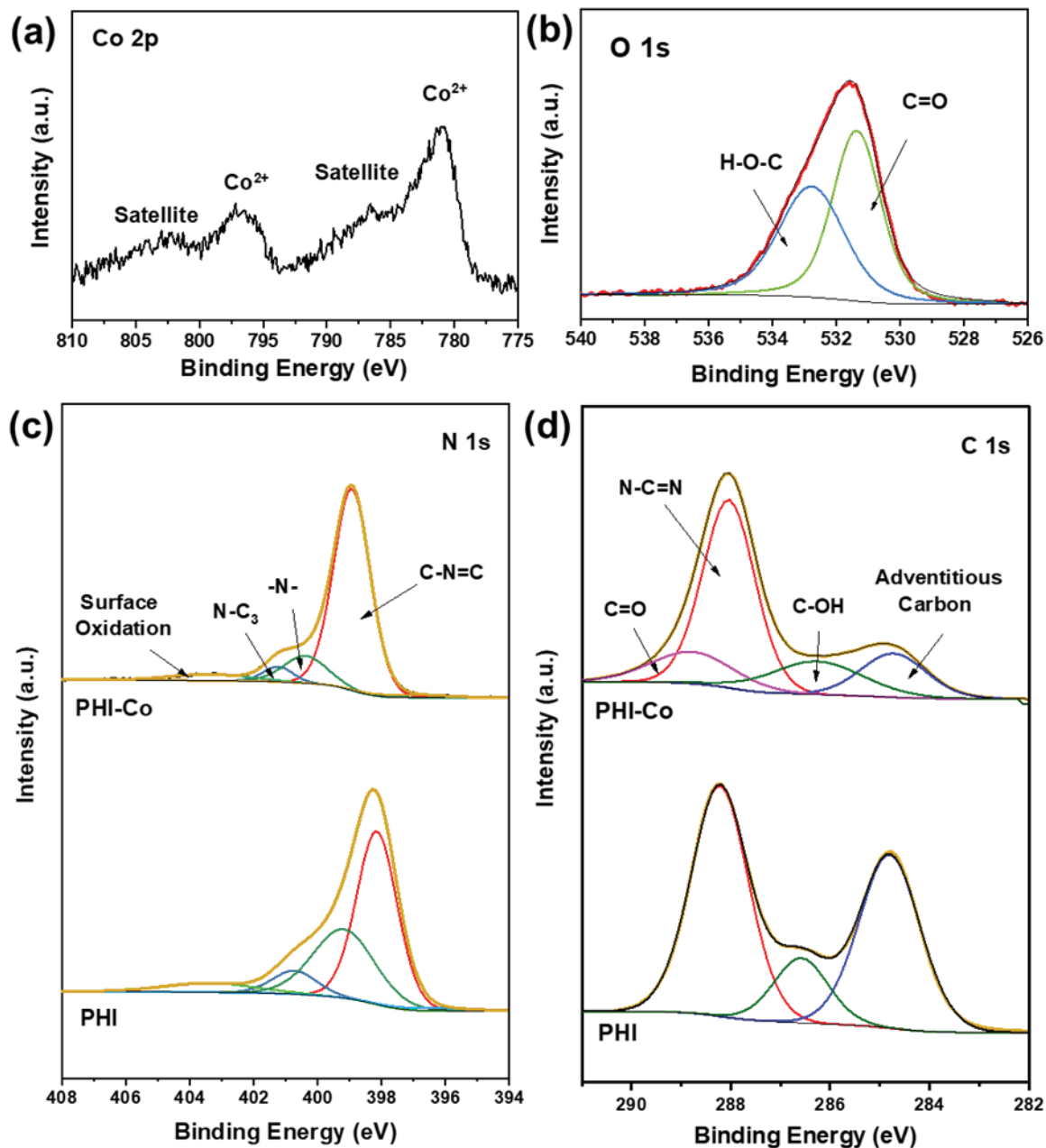


Figure 2-2 (a) Co 2p and (b) O 1s XPS spectra of PHI-Co. (c) N 1s and (d) C 1s XPS spectra of PHI-Co and PHI, respectively.

In the N 1s XPS spectra of PHI-Co (**Figure 2-2c**), the peaks at 398.5 eV and 400.9 eV can be assigned to the C-N=C (ring N in heptazine unit), N-C₃ (central N in heptazine unit), respectively, while the peak at 399.6 eV corresponds to the N bridges between the heptazine

Chapter 2. Cobalt intercalated poly(heptazine) imide for electrocatalytic oxygen evolution

rings^{155,186}. In **Figure 2-2d**, the major contribution in the C 1s spectrum at 288.1 eV can be assigned to N-C=N in the heptazine unit, while the peaks at 284.8 eV and 286.4 eV can be attributed to adventitious carbon and hydroxylated surface carbon atoms, respectively¹⁵². The other small peaks appearing in the C 1s spectra at 288.8 eV and in N 1s spectra at 404.1 eV are indicative of surface oxidation¹⁵⁵. Except for the peak at 288.2 eV in the C 1s of PHI-Co, which corresponds to C=O originating from the surface oxidation, the other N and C species in the XPS N 1s and C 1s spectra of PHI-Co can also be found in cobalt-free PHI (**Figure 2-2c, d**), suggesting that the PHI backbone stays intact after the intercalation of Co cations.

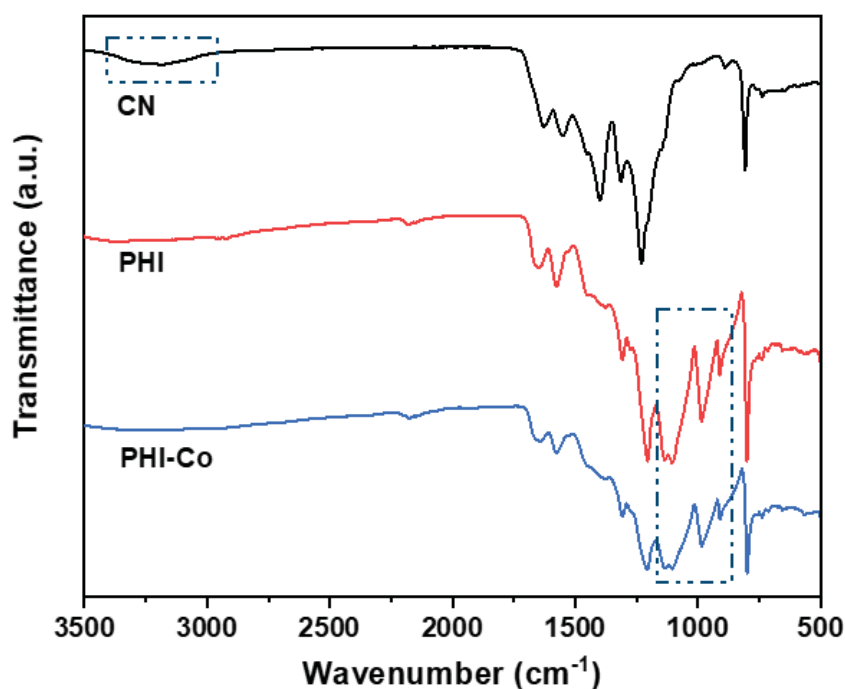


Figure 2-3. FT-IR spectrum of polymeric CN, PHI and PHI-Co.

The similarity of the chemical states of PHI-Co and PHI can be further proved by their infrared (IR) spectra (**Figure 2-3**). In a typical IR spectrum of PHI-Co, the sharp peak at 810 cm⁻¹ can be assigned to heptazine ring out-of-plane bending, while the series of peaks in the range of 1254-1630 cm⁻¹ corresponding to CN heterocycles⁴⁴. These signals can also be found in cobalt-

Chapter 2. Cobalt intercalated poly(heptazine) imide for electrocatalytic oxygen evolution

free PHI and in the IR spectrum of polymeric CN, indicating that the polymeric backbone of PHI-Co stays intact after the intercalation of Co cations. The small peak at 2185 cm^{-1} in PHI and PHI-Co can be ascribed to nitrile stretch, which was also found in some previous reports of PHI's¹⁵³. A broad peak centered at 3190 cm^{-1} can be observed in the IR spectrum of polymeric CN, ascribing to the NH_2 group⁶. This peak cannot be found in both PHI-Co or PHI, indicating that the bridges between heptazine rings are deprotonated imide instead of amine. Meanwhile, several new peaks emerge in the range of $865\text{-}1158\text{ cm}^{-1}$, which show symmetric vibrations of the metal- NC_2 moiety, resulting from the intercalation of metal ions^{49,151}.

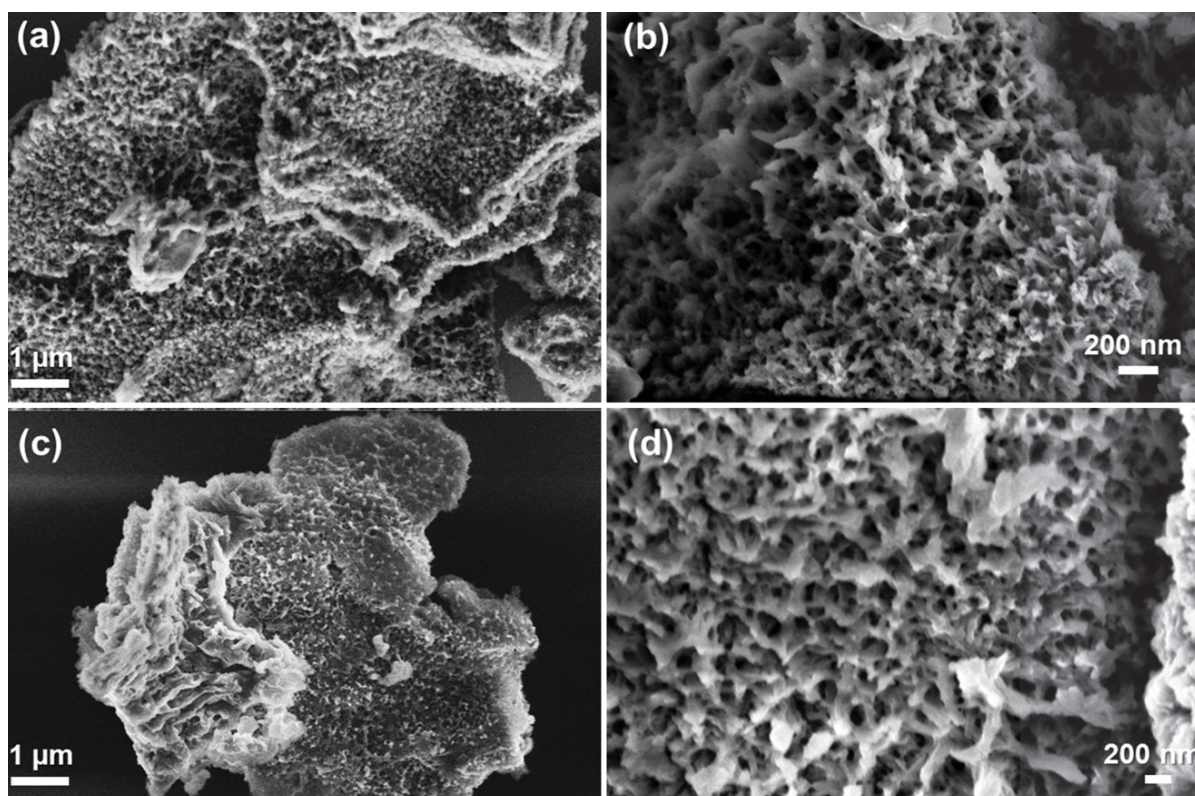


Figure 2-4 SEM images of (a, b) PHI in magnifications of 10k and 50k and (c,d) PHI-Co in magnifications of 10k and 50k, respectively.

The typical morphology of PHI-Co and cobalt-free PHI was recorded via scanning electron microscopy (SEM, **Figure 2-4**). PHI-Co and PHI share a very similar coral-like morphology, which further proves that the intercalation of Co cations does not change the backbone of PHI.

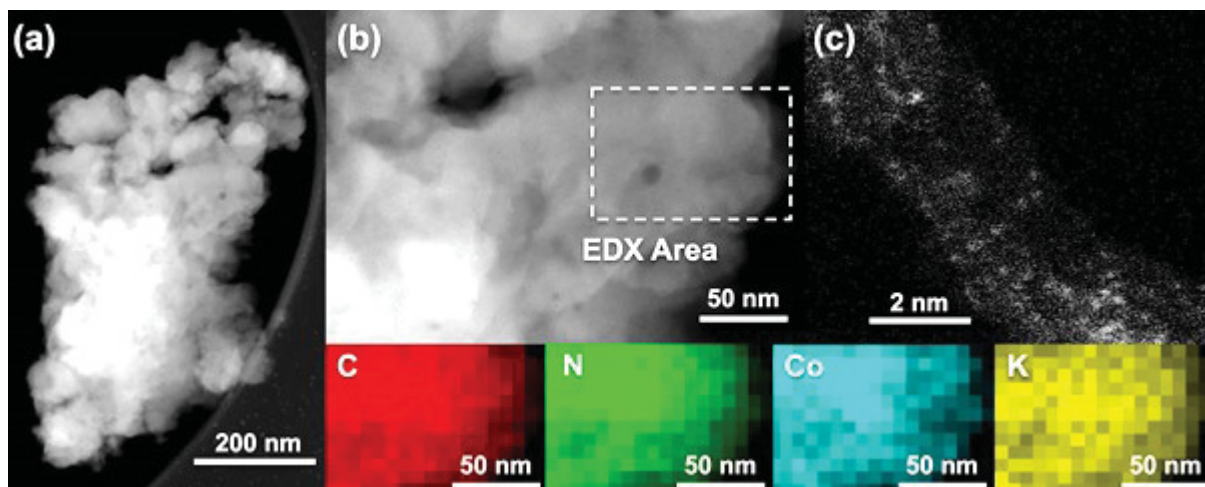


Figure 2-5. (a) ADF-STEM image of a typical PHI-Co agglomerate. (b) Enlargement from Figure 3a with EDX elemental maps of C, N, Co, K elements shown at the bottom, the solid white rectangle indicates the area from which EDX maps were obtained. (c) HR ADF-STEM image of PHI-Co, where the light spots represent cobalt atoms.

The distribution of Co ions was further detected by annular dark-field scanning transmission electron microscopy (ADF-STEM) coupled with an energy dispersive X-ray (EDX) detector. In typical ADF-STEM images, the elements with larger nuclei appear with a higher brightness than light elements such as C and N, which can help to localize the Co cations in the polymeric PHI lattice. It can be first observed from low-resolution STEM images (**Figure 2-5a,b**), that the whole PHI-Co particles in scope have homogenous brightness. Therefore, no pronounced Co agglomeration can be spotted. From EDX elemental mapping (**Figure 2-5**, inset), the signal of Co can be detected over the entire measured part of the sample, further confirming that the Co cations dispersed homogeneously in the PHI structure. In the HR ADF-STEM image of PHI-Co (**Figure 2-5c**), bright dots of with size of $3.2 \pm 0.5 \text{ \AA}$ are dispersed in the darker PHI matrix, roughly fits with the size of cobalt atoms or subnano clusters, proving that Co atoms in the PHI structure are dispersed at the atomic level.

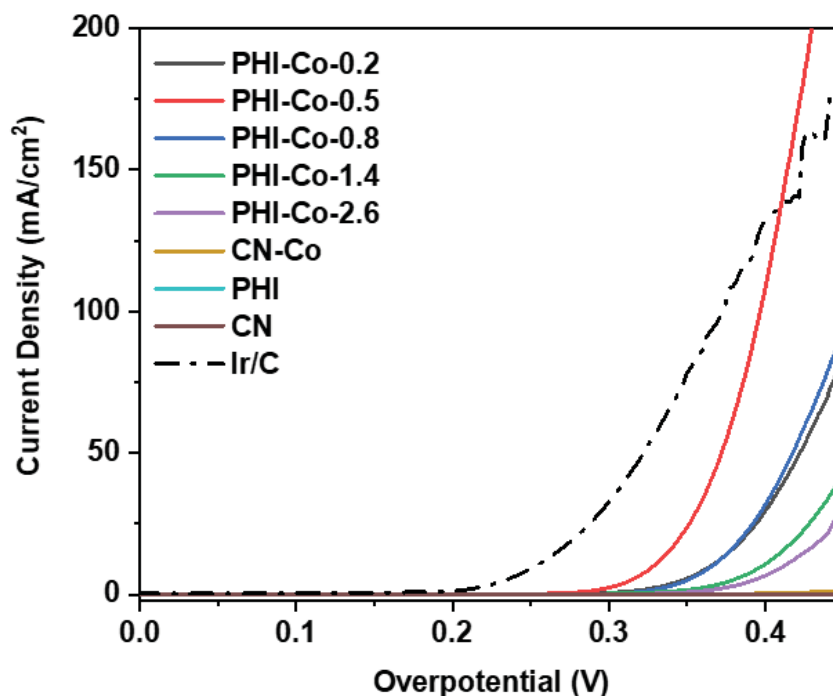


Figure 2-6. OER polarization curves of PHI-Co's, CN-Co, PHI, CN and commercial Ir/C.

The electrocatalytic performance of PHI-Co with different cobalt contents was then measured in 1 M KOH solutions, with a mass loading of 0.38 mg/cm² of catalyst on glassy carbon (GC) rotating disk electrodes. The PHI-Co's are compared with cobalt-doped carbon nitride (CN-Co, 0.52 wt% cobalt), cobalt-free PHI, polymeric carbon nitride (CN), and a commercial Ir/C catalyst. The OER activities of these catalysts were first evaluated by polarization curves (**Figure 2-6**). It can be observed in **Figure 2-6**, PHI-Co's show significantly enhanced OER activity compared to CN-Co, PHI and CN. Among the PHI-Co's, PHI-Co-0.5 shows the lowest overpotential. Notably, the overpotential ($j = 10 \text{ mA/cm}^2$) of PHI-Co-0.5 is very low (0.324 V), which is a promising value when compared with other metal-doped polymer-based electrocatalysts (**Table 2-2**). As a semiconductor, the activity of PHI-Co-0.5 is still competitive with some state-of-the-art carbon-based electrocatalysts (**Table 2-3**).

Chapter 2. Cobalt intercalated poly(heptazine) imide for electrocatalytic oxygen evolution

Table 2-2 OER activities of various polymeric electrocatalysts (the current density is calculated with respect to the geometric surface of the electrode)

Catalyst Names	Electrolyte	Electrode Type	Overpotential (V) ($j = 10 \text{ mA/cm}^2$)	Tafel slope (mV/dec)	Ref.
PHI-Co	1 M KOH	Glassy carbon	0.324	44	This work
Co-UMOFNs	1 M KOH	Glassy carbon	0.371	103	165
Ni-UMOFNs	1 M KOH	Glassy carbon	0.321	65	165
Co ₂ (μ -OH) ₂ (bbta)	1 M KOH	Glassy carbon	0.387	N/A	187
NiPc-MOF	1 M KOH	Glassy carbon	0.390	74	156
Ni-BDC	1 M KOH	Glassy carbon	0.358	57	188
Ultrathin Co-MOF	1 M KOH	Glassy carbon	0.263	74	189
NNU-23 (Fe ₂ Ni-MOF)	1 M KOH	Glassy carbon	0.365	82	190
[Ni _{1.5} (H ₂ L)(4,4'-bipy) _{1.5} (H ₂ O) ₃]-2 H ₂ O	1 M KOH	Glassy carbon	0.395	N/A	170
CoNi-COP	1 M KOH	Glassy carbon	0.40	61	191
EG/ZIF-67	1 M KOH	Exfoliated graphene	0.320	132	192

Chapter 2. Cobalt intercalated poly(heptazine) imide for electrocatalytic oxygen evolution

Table 2-3 OER activity of various electrocatalysts (the current density is calculated in respect to the geometric surface of the electrode)

Catalyst Names	Electrolyte	Electrode Type	Overpotential (V) ($j = 10 \text{ mA/cm}^2$)	Tafel slope (mV/dec)	Ref.
PHI-Co	1 M KOH	Glassy carbon	0.324	44	This work
Ir/C	1 M KOH	Glassy carbon	0.254	61	This work
Co ₄ N/CNW/CC	1 M KOH	Glassy carbon	0.330	81	193
P-Co ₄ N/CNW/CC	1 M KOH	Glassy carbon	0.350	113	193
FeCoN-Gs	1 M KOH	Glassy carbon	0.288	34.3	194
NiFe@g-C ₃ N ₄ /CNTs	1 M KOH	Glassy carbon	0.326	67	21
Co ₃ O ₄ /N-rmGO	1 M KOH	Glassy carbon	0.310	67	145
NC-Co/CoN _x	1 M KOH	Glassy carbon	0.289	137	195
NC-Co	1 M KOH	Glassy carbon	0.373	184	195
NC-NiCu-NiCuN	1 M KOH	Glassy carbon	0.232	55	196
Ni-Mn-LDH/g-C ₃ N ₄ (10%)	1 M KOH	Glassy carbon	0.316	132	197
CoMn LDH	1 M KOH	Glassy carbon	0.324	43	182

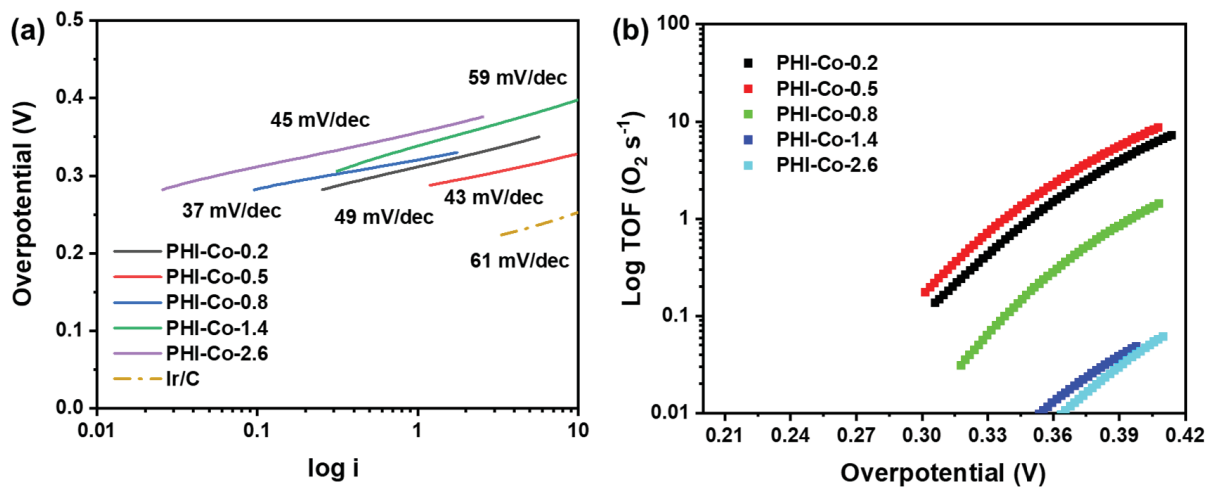


Figure 2-7. (a) Tafel slopes and (b) turnover frequency (TOF) plotted against overpotential of PHI-Co's derived from the OER polarization curves in **Figure 2-6**.

The Tafel plots (**Figure 2-7a**) of PHI-Co's were extracted from the polarization curves (**Figure 2-6**) to understand the kinetics of the reactions. A small Tafel slope indicates faster kinetics of the OER¹⁹⁸. The best-performing PHI-Co (0.45 wt% Co) shows a small Tafel slope of 43 mV/dec, not only smaller than that of commercial Ir/C, but also lower than many state-of-the-art electrocatalysts under similar reaction conditions (**Table 2-2, 2-3**).

The activity of PHI-Co's was further investigated by calculating the turnover frequency (TOF) of the electrocatalysts, with all the cobalt ions exposed on the surface considered active sites. The molar ratio of cobalt atoms exposed on the surface of PHI-Co's were obtained from the surface-sensitive XPS measurements and listed in **Table 2-4**. The TOF values were plotted against the applied overpotential (**Figure 2-7b**). The TOF of PHI-Co-0.5 is remarkably higher than the other PHI-Co's. This trend indicates that the synergistic effect between PHI backbone and Co is strongest in PHI-Co-0.5, which therefore shows the highest activity per active site.

Chapter 2. Cobalt intercalated poly(heptazine) imide for electrocatalytic oxygen evolution

Table 2-4 Surface exposed cobalt in molar percentage in PHI-Co's.

Samples	Cobalt Content (mol%)
PHI-Co-0.2	0.19
PHI-Co-0.5	0.41
PHI-Co-0.8	1.22
PHI-Co-1.4	1.50
PHI-Co-2.6	2.27
PHI-Co-14h	1.13

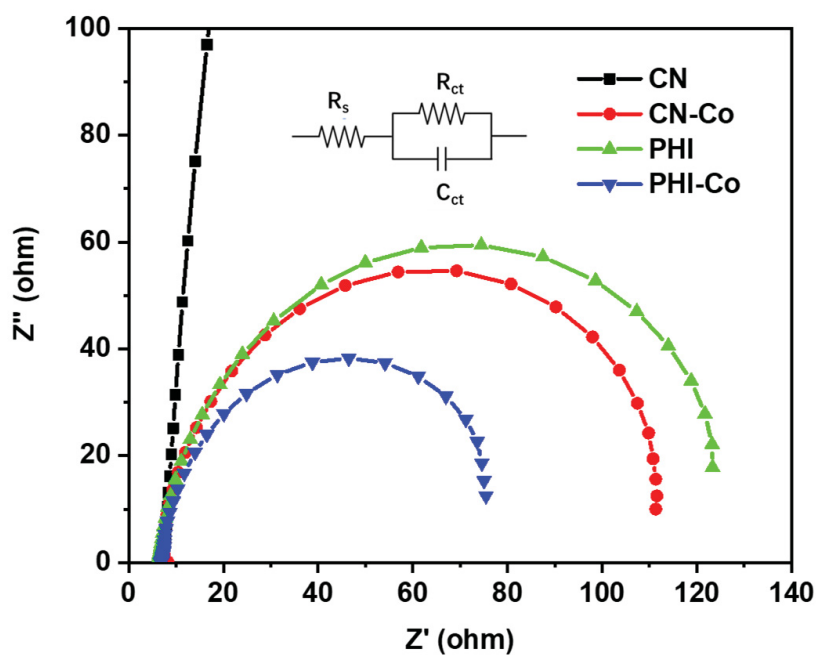


Figure 2-8 Nyquist plots of PHI-Co, PHI, CN-Co, CN in 1 M KOH electrolyte, measured under the static potential of 1.6 V vs RHE, and the corresponding equivalent circuit (inset).

Chapter 2. Cobalt intercalated poly(heptazine) imide for electrocatalytic oxygen evolution

In order to attain a better understanding of the kinetics of this PHI-Co catalytic OER process, electrochemical impedance (EIS) spectra were measured at 1.6 V vs RHE. The Nyquist plot with the semicircle at high frequency fits with the equivalent circuit diagram shown in **Figure 2-8 inset**, the diameter and phase angle of the semicircle stands for the charge transfer resistance (R_{ct}) and capacity (C_{ct}) at the interface of the catalyst and electrolyte, respectively⁶. As calculated from the Nyquist plots (**Figure 2-8**), the diameter of the semicircle (R_{ct}) is lowest for PHI-Co (84 Ω), compared with CN-Co (100 Ω), PHI (105 Ω), and CN (409 Ω), suggesting that PHI-Co has the fastest charge transfer between the catalyst and electrolyte.

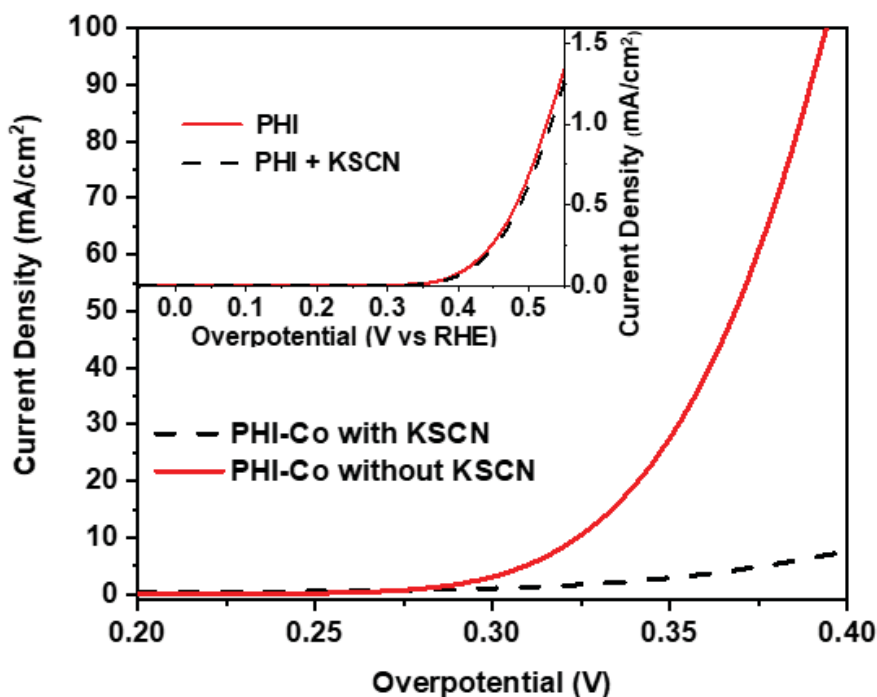


Figure 2-9 OER polarization curves of PHI-Co and PHI in 1 M KOH electrolyte before and after the addition of 10 mM KSCN.

To further confirm that Co^{2+} ions are responsible for the OER performance of PHI-Co, a metal center poisoning experiment was employed. 10 mM KSCN was injected into the electrolyte to poison the transition metal centers (**Figure 2-9**)¹⁹⁹. The addition of SCN^- to PHI-Co-catalyzed OER causes a drastic decrease in the current intensity. For instance, at an overpotential of 0.4

Chapter 2. Cobalt intercalated poly(heptazine) imide for electrocatalytic oxygen evolution

V, the current density of PHI-Co dropped by more than a factor of 10, from 117.5 mA/cm² to 8.3 mA/cm², leading to a remarkable increase of the overpotential ($j = 10$ mA/cm²) of more than 0.1 V. While the same poisoning test was also carried out with pure PHI (**Figure 2-9 inset**), no observable OER activity change can be observed, ruling out the possible influence of SCN⁻ on PHI. Therefore, the cobalt-species are verified as the active centers of PHI-Co for OER. As the existence of metallic cobalt or cobalt oxides in PHI-Co has been ruled out from the previous XRD, XPS, and STEM analysis, it can be concluded that the active sites in PHI-Co are Co²⁺ cations in the PHI structure.

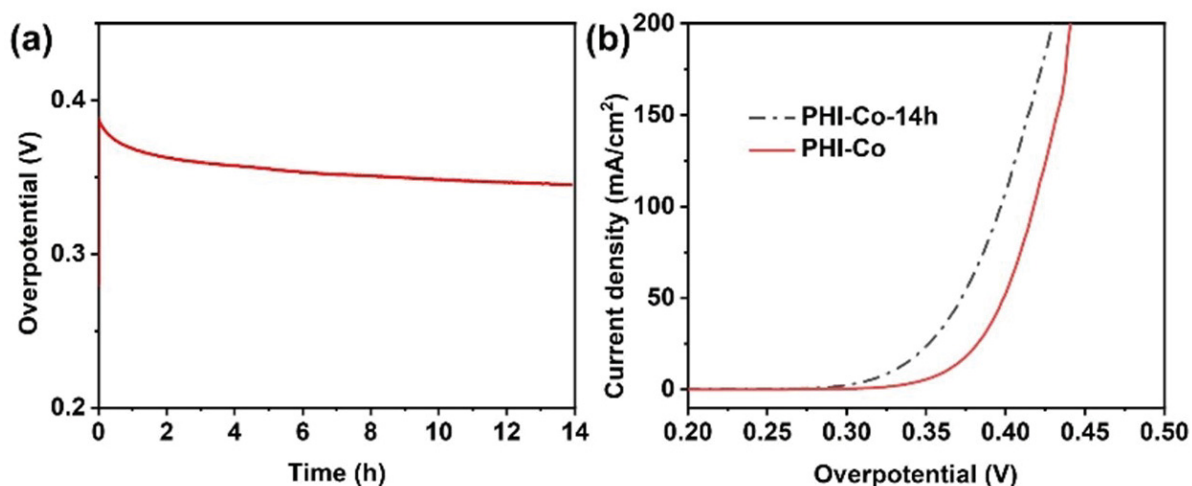


Figure 2-10. (a) Stability test of PHI-Co-0.5 in 1 M KOH for 14h. (b) Polarization curves of PHI-Co before and after stability test.

The stability of PHI-Co-0.5 was measured under constant current densities of 10 mA/cm² for 14 h (**Figure 2-10a**). During the chronopotentiometric stability test, the overpotential of PHI decreased constantly. By the end of the test, the OER polarization curve of the same sample was measured again and compared with the curve before the stability test (**Figure 2-10b**). It can be observed that after the stability test, the overpotential ($j = 10$ mA/cm²) of PHI-Co-0.5 had decreased by 0.04 V.

The chemical structure of PHI-Co before and after the stability test provides more insight into this phenomenon. XPS and IR spectra of the PHI-Co film on the electrode were recorded before

Chapter 2. Cobalt intercalated poly(heptazine) imide for electrocatalytic oxygen evolution

and after the stability test (**Figure 2-11**). Notably, the content of Co on the surface of the PHI-Co electrode has remarkably increased from 0.41 wt% to 1.13 wt% after the stability test (**Figure 2-11a**). This high content of Co on the surface of PHI after 14 h indicates that the cobalt ions from the inside of the PHI-Co slowly migrated to the surface. Meanwhile, no significant change is observed in the N 1s XPS spectrum and IR spectrum of PHI-Co-14h, compared with the catalyst before the stability test (**Figure 2-11b, c**), suggesting the basic structure of poly(heptazine) imide remains during this process. Therefore, the increased OER performance might only stem from the accumulation of the Co^{2+} on the surface.

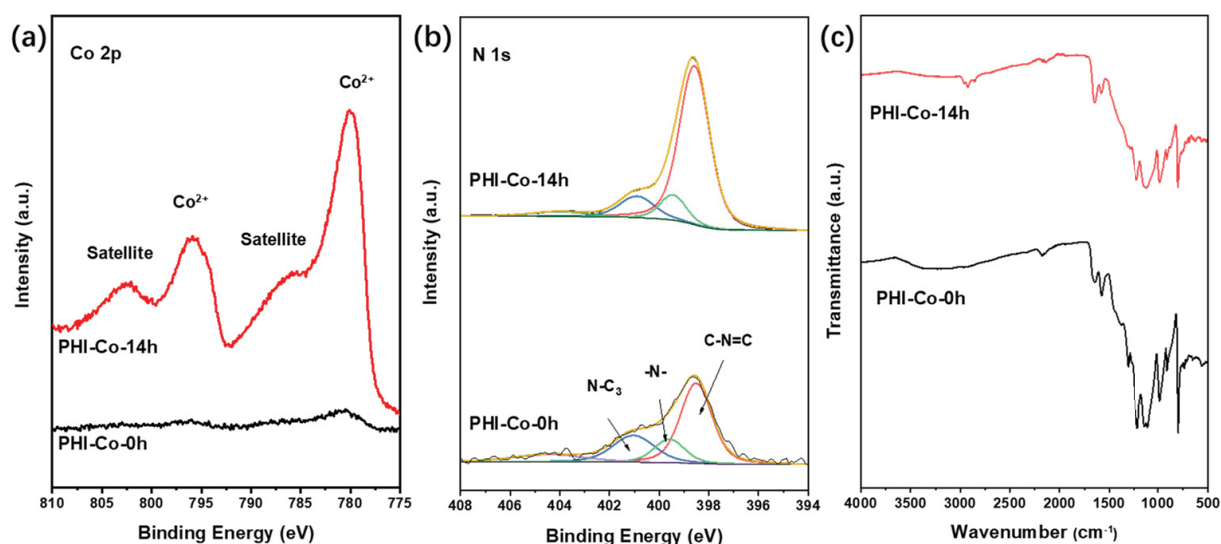


Figure 2-11 (a) Co 2p (b) N 1s XPS spectra and (c) IR spectra of PHI-Co before and after *approx.* 14 h of stability test.

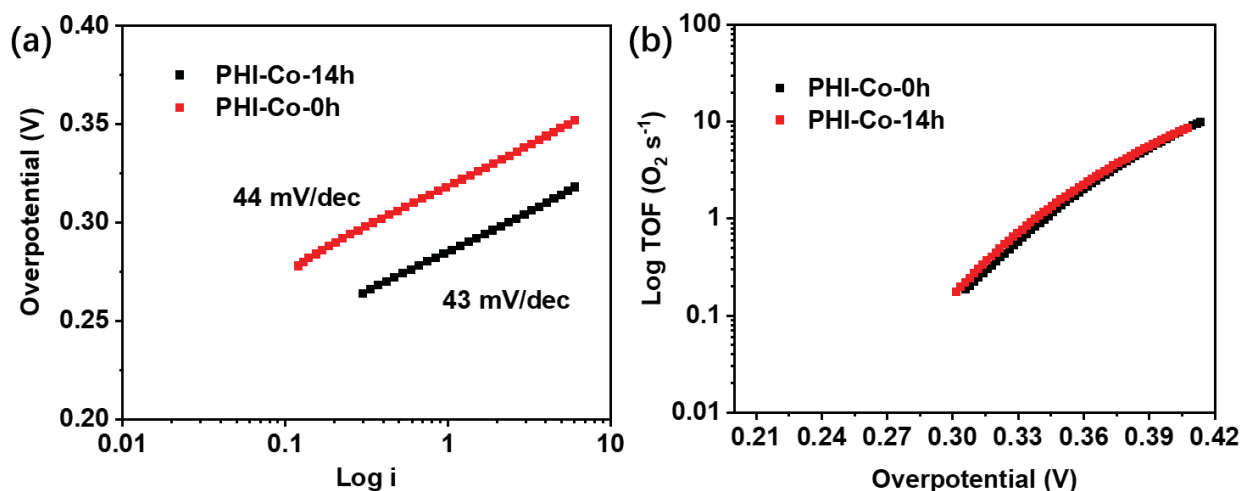


Figure 2-12 (c) Tafel plots of PHI-Co before and after stability test (d) TOF to overpotential plots of PHI-Co before and after stability test.

Based on the changed cobalt content on the surface obtained from the XPS results (**Figure 2-11a**), the Tafel slope and TOF before and after the stability test are derived and given in **Figure 2-12**. Despite the increased activity observed during the stability test, the kinetics of this reaction stays the same, and activity per cobalt active sites and the kinetics of the reaction barely changed as judged from Tafel slope and TOF before and after the stability test.

Conclusion

In summary, cobalt poly(heptazine imide) (PHI-Co) was synthesized via a simple mixed salt melt method. Co cations can be introduced into the PHI backbone in atomic dispersion and well controllable amounts by adjusting the Co source content in the salt template. The intercalation of Co cations largely enhanced the charge mobility in PHI's, enabling it to work as an electrocatalyst without carbon additives. Meanwhile, the atomically dispersed Co cations also provided a highly efficient metal active center, leading to significantly enhanced OER activity. Among the PHI-Co's, the overpotential ($j = 10 \text{ mA/cm}^2$) of the most active PHI-Co-0.5 is 0.324 V, which is not only standing among the best metal-doped polymer-based electrocatalysts but

Chapter 2. Cobalt intercalated poly(heptazine) imide for electrocatalytic oxygen evolution

also competitive with some state-of-the-art carbon-based electrocatalysts under similar conditions.

Chapter 2. Cobalt intercalated poly(heptazine) imide for electrocatalytic oxygen evolution

3 Cobalt intercalated poly(heptazine) imide as photocatalyst for water oxidation

Motivation

Photocatalytic water splitting is a low-cost and sustainable solution to produce hydrogen^{22,25}. Although progress in the photocatalytic hydrogen evolution is frequently made^{200–202}, the other half-reaction, i.e., photocatalytic water oxidation, is still the bottleneck of developing efficient visible-light-driven overall water splitting^{25,127}. Since photocatalytic water oxidation involves a four-electron process, photocatalysts with high water oxidation efficiency often require a very positive valence band. So far, photoactive catalysts such as BiVO₄, WO₃, and Bi₂WO₆ have been reported for photocatalytic water oxidation. However, most of these materials are toxic and require sophisticated synthetic processes^{20,31,122,128,129}. Therefore, heavy-metal-free, low-cost, and high-performance photocatalysts are still desired for visible-light-driven water oxidation.

Poly(heptazine imide) (PHI) is a highly active visible-light-responsive photocatalyst^{43,152,204}. It inherited the advantages of carbon nitrides, including a favorable band structure, excellent stability, abundant precursors, facile synthesis procedures, and excellent visible-light-driven hydrogen generation activity^{6,45}. However, as for carbon nitrides, the valence band position of conventional PHI is not “positive” enough, which has limited its potential for water oxidation^{28,203}.

From the last chapter, it can be seen that cobalt intercalated poly(heptazine) imide (PHI-Co) shows excellent oxygen generation activity as an electrocatalyst, because of the presence of atomically dispersed Co-cations in its matrix. The intercalated Co-cations in PHI backbones provided active centers for oxygen evolution reaction. Inspired by this result, in this chapter, PHI-Co was applied to visible-light-driven water oxidation. The as-prepared PHI-Co exhibited a photocatalytic oxygen generation activity of 589 $\mu\text{mol g}^{-1}\text{h}^{-1}$ under the illumination with visible light ($\lambda > 420 \text{ nm}$), and a high apparent quantum yield of 5.1%.

Results and Discussion

The preparation of PHI-Co has been described in **Chapter 2**. In brief, the PHI-Co was obtained by heating the CoCl_2 containing salt template (KCl/LiCl) with the tetrazole precursor at $550\text{ }^\circ\text{C}$ for 8 h in argon flow. Additionally, to understand the unique coordination between Co and PHI backbone, cobalt-doped polymeric carbon nitride (CN-Co) was prepared via conventional wet impregnation using $\text{Co}(\text{NO}_3)_2$ as cobalt source²⁰⁵. A detailed description of the aforementioned synthetic process can be found in **Chapter 7 Experimental Section**.

As will be shown below, a PHI-Co with a Co content of 0.08wt% (PHI-Co-0.1) shows the best photocatalytic performance. The cobalt-doped carbon nitride with a similar Co loading amount (0.12 wt%), is denoted as CN-Co-0.1 correspondingly. The content of cobalt in the PHI-Co photocatalysts and the CN-Co-0.1 reference are obtained from inductively coupled plasma optical emission spectrometry (ICP-OES).

The crystallinity of PHI-Co-0.1 was investigated via powder X-ray diffraction (PXRD) measurements, and compared with CN-Co-0.1, PHI (i.e. poly(heptazine) imide loaded exclusively with potassium ions) and pure CN (**Figure 3-1**). PHI shows the most pronounced peaks and thus seems to show a higher crystallinity than CN. In the XRD pattern of PHI, the diffraction peak at 8.3° , 14.1° , 23.8° , 27.0° and 36.3° , corresponding to $(\bar{1}10)$, (001) , $(\bar{1}20)$, $(0\bar{1}1)$, and $(23\bar{1}/32\bar{1})$ facets of the well-crystallized PHI structure, respectively¹⁵³. PHI-Co-0.1 exhibits similar XRD patterns as PHI. Meanwhile CN-Co-0.1 resembles the typical pattern of CN, where the diffraction peak at 27.0° can be ascribed to the layer stacking. The diffraction peak at 13.2° correspond to the (100) facet^{133,206}. The results suggest that the introduction of Co atoms did not influence the structure of either PHI or CN significantly.

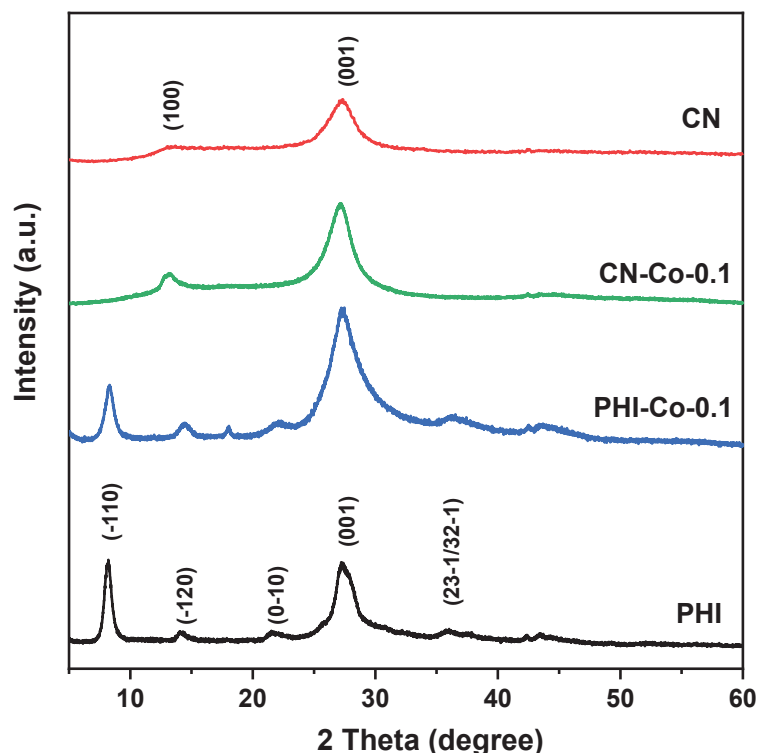


Figure 3-1. X-ray diffraction (XRD) patterns of PHI-Co-0.1, PHI, CN-Co-0.1, and CN.

The chemical states of elements in PHI-Co-0.1 were further studied by X-ray photoelectron spectra (XPS). Co ions in PHI-Co-0.1 and CN-Co-0.1 both show Co(II) oxidation states in their XPS Co 2p spectra (**Figure 3-2a**), which is an asymmetry doublet peak centered at 780.4 eV with a strong satellite feature centered at 785.4 eV^{154,169}. The XPS O 1s spectra of PHI-Co-0.1 and CN-Co-0.1 are presented in **Figure 3-2b**. No trace of Co-O bond can be observed at 529-530 eV¹⁵⁴.

In the N 1s XPS spectra of PHI-Co-0.1 (**Figure 3-2c**), the peaks at 398.4 eV and 401.2 eV can be assigned to the C-N=C (ring N in heptazine unit), N-C₃ (central N in heptazine unit), respectively, while contribution at 399.5 eV corresponds to N bridges between the heptazine rings. The other small peak appearing in the N 1s spectra at 403.8 eV indicates surface oxidation¹⁵⁵. The major contribution in the C 1s spectrum (**Figure 3-2d**) at 288.2 eV can be assigned to N-C=N in the heptazine unit, while 284.8 eV and 286.5 eV can be attributed to adventitious carbon and hydroxylated surface carbon atoms, respectively¹⁵². According to the

Chapter 3. Cobalt intercalated poly(heptazine) imide as photocatalyst for water oxidation

N 1s and C 1s XPS spectra of PHI-Co-0.1 and CN-Co-0.1 (Figure 3-2c, d), the catalysts share a very similar polymeric carbon nitride backbone, with heptazine units as basic building block²⁸.

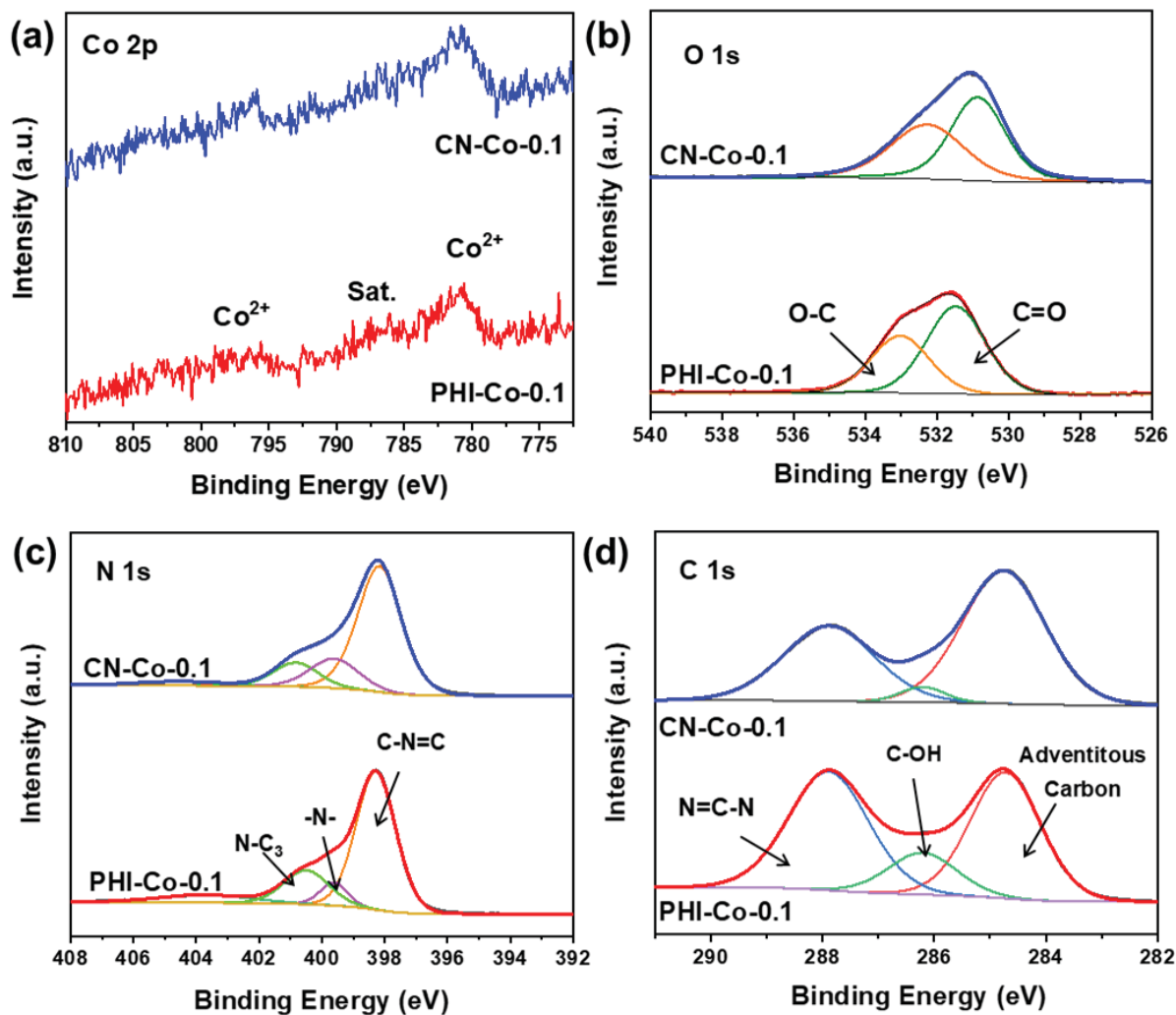


Figure 3-2. (a) Co 2p, (b) O 1s, (c) N 1s and (d) C 1s, XPS spectra of PHI-Co-0.1 and CN-Co-0.1, respectively.

Chapter 3. Cobalt intercalated poly(heptazine) imide as photocatalyst for water oxidation

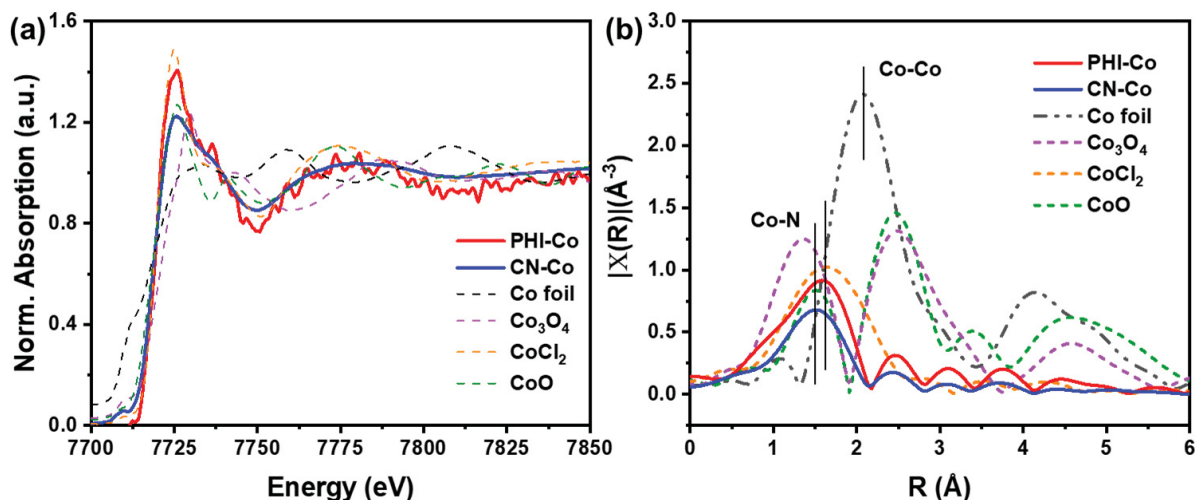


Figure 3-3. (a) Co edge XANES spectra of PHI-Co-0.1, CN-Co-0.1, CoO, Co₃O₄ CoCl₂, and Co foil. (b) k^3 -weighted R space plots EXAFS spectra for PHI-Co-0.1, CN-Co-0.1, and the references.

The chemical state of intercalated Co in PHI-Co and CN-Co further confirmed by X-ray absorption near-edge spectroscopy (XANES, **Figure 3-3a**), using CoO, Co₃O₄ CoCl₂, and metallic Co as the references. From the XANES spectra in **Figure 3-3a**, the chemical state of intercalated Co in PHI-Co-0.1 and CN-Co-0.1 can be identified as Co(II), which is in agreement with their XPS Co 2p spectra^{154,169}.

Extended X-ray Absorption Fine Structure (EXAFS) spectra were plotted in R space (**Figure 3-3a**), to understand the local atomic structure around Co atoms in PHI-Co-0.1 and CN-Co-0.1. In an EXAFS R plot, the peak positions usually correspond to the distance between the target atom (Co) and the neighboring atoms. In **Figure 3-3b**, the R plot of CN-Co-0.1 displays a major peak centered at 1.5 Å, which corresponds to a typical Co-N coordination^{169,184}. Due to the very similar bond length, the signal of Co-N and Co-O bonds are usually difficult to distinguish in EXAFS R plots^{169,184}. However, as observed in the O 1s XPS spectrum (**Figure 3-2d**), no contribution of O-metal bonds (centered at 529 eV) can be found in both of the O 1s spectra, excluding the existence of CoO particles or clusters in PHI-Co-0.1 and CN-Co-0.1¹⁵⁴. Notably, in the R plot of PHI-Co-0.1, the major peak is observed at 1.64 Å, indicating a slightly increased distance between Co atoms and the PHI polymeric lattice compared to Co in polymeric CN,

Chapter 3. Cobalt intercalated poly(heptazine) imide as photocatalyst for water oxidation

suggesting weaker coordination in PHI-Co samples comparing with CN-Co²⁰⁷. Additionally, no Co-Co coordination is observed in the R plot of PHI-Co-0.1 or CN-Co-0.1, suggesting that the Co atoms are dispersed individually in both PHI-Co-0.1 and CN-Co-0.1, which can also be confirmed by their annular dark-field scanning transmission electron microscopy (ADF-STEM) images (**Figure 3-4**).

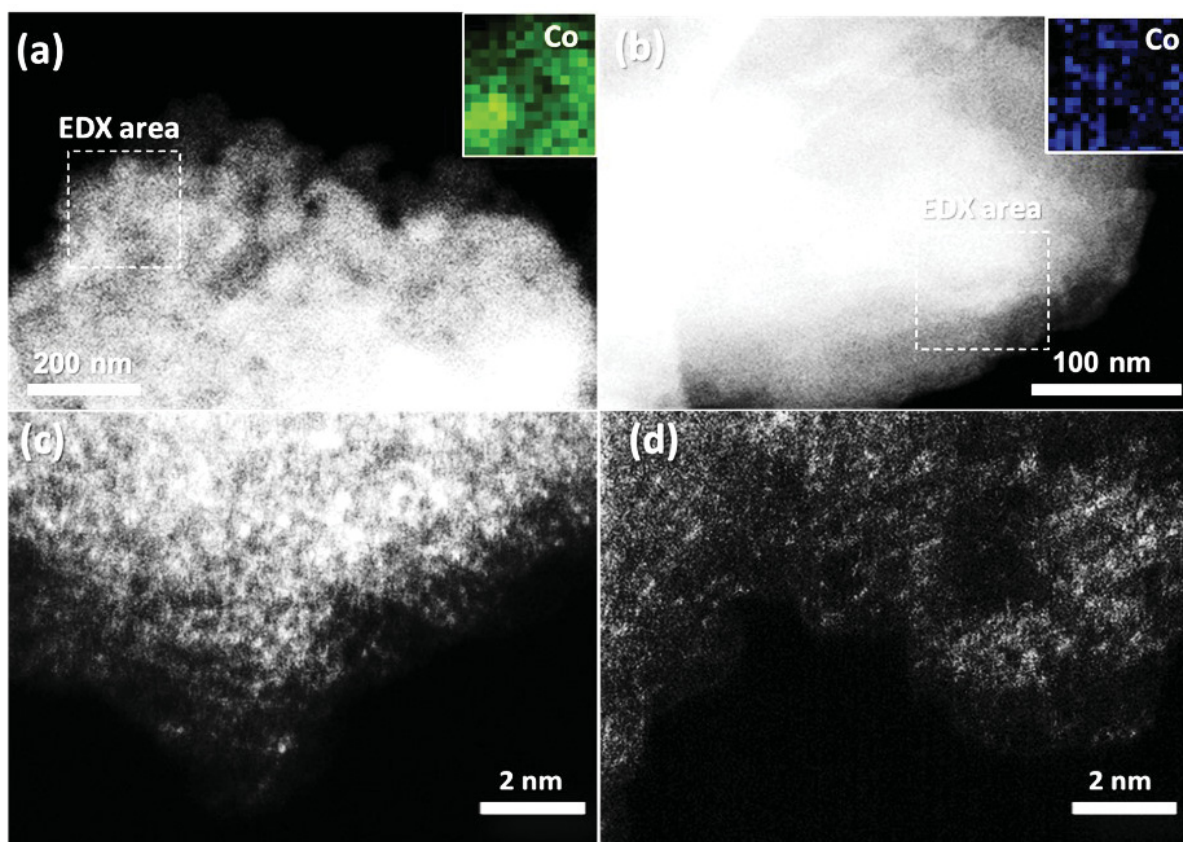


Figure 3-4. ADF-STEM images of (a) PHI-Co-0.1 and (b) CN-Co-0.1, with EDX elemental mapping of Co element inset at the upper right corner, the white rectangle indicates the area from which EDX maps were obtained. High-resolution ADF-STEM images of (c) PHI-Co-0.1 and (d) CN-Co-0.1.

Energy Dispersive X-ray (EDX) detector coupled with ADF-STEM was used to detect the distribution of Co ions in PHI-Co-0.1 and CN-Co-0.1. From EDX elemental mapping (**Figure 3-4a, b, inset**), the signal of Co can be detected over the measured part of the samples. Unlike

Chapter 3. Cobalt intercalated poly(heptazine) imide as photocatalyst for water oxidation

the uniform dispersion of Co in PHI-Co-0.1, which can be found all over the detected area, the distribution of Co atoms in CN-Co-0.1 is rather inhomogeneous. This is because of the different preparation processes of PHI-Co-0.1 and CN-Co-0.1. In the synthetic process of PHI-Co-0.1, Co cations were already introduced to the structure during the condensation of PHI, leading to a homogenous dispersion of Co in the PHI structure.

On the other hand, the CN-Co-0.1 sample was prepared via a post-synthesis modification, where the Co-atoms adsorbed first on the surface of the bulky CN substrate and further creates a stronger bond with CN via calcination. Due to this meager loading amount (0.012 wt%), the concentration of Co source for wet impregnation was also very low. Therefore, the final location of doped Co atoms on the CN surface is rather difficult to control and further results in the inhomogeneous dispersion of doped Co. However, in high-resolution ADF-STEM images of PHI-Co-0.1 and CN-Co-0.1 (**Figure 3-4c, d**), it can still be observed that the bright dots of cobalt atoms dispersed in the darker PHI and CN matrix at the atomic level, proving the size of the active site in both catalysts are with a similar scale.

UV-vis absorption of PHI-Co-0.1, CN-Co-0.1, PHI and CN was measured to investigate the light response region and optical bandgap width of the photocatalyst. The XPS valence band maximum (VBM) were employed to obtain the valence band maximum of the semiconductors mentioned above. When bandgap energy (E_g) and valence band maximum (E_{vb}) are both known, the position of conduction band minimum (E_{cb}) can be calculated via the following equation:

$$E_g = E_{cb} - E_{vb} \quad (3-1)$$

Chapter 3. Cobalt intercalated poly(heptazine) imide as photocatalyst for water oxidation

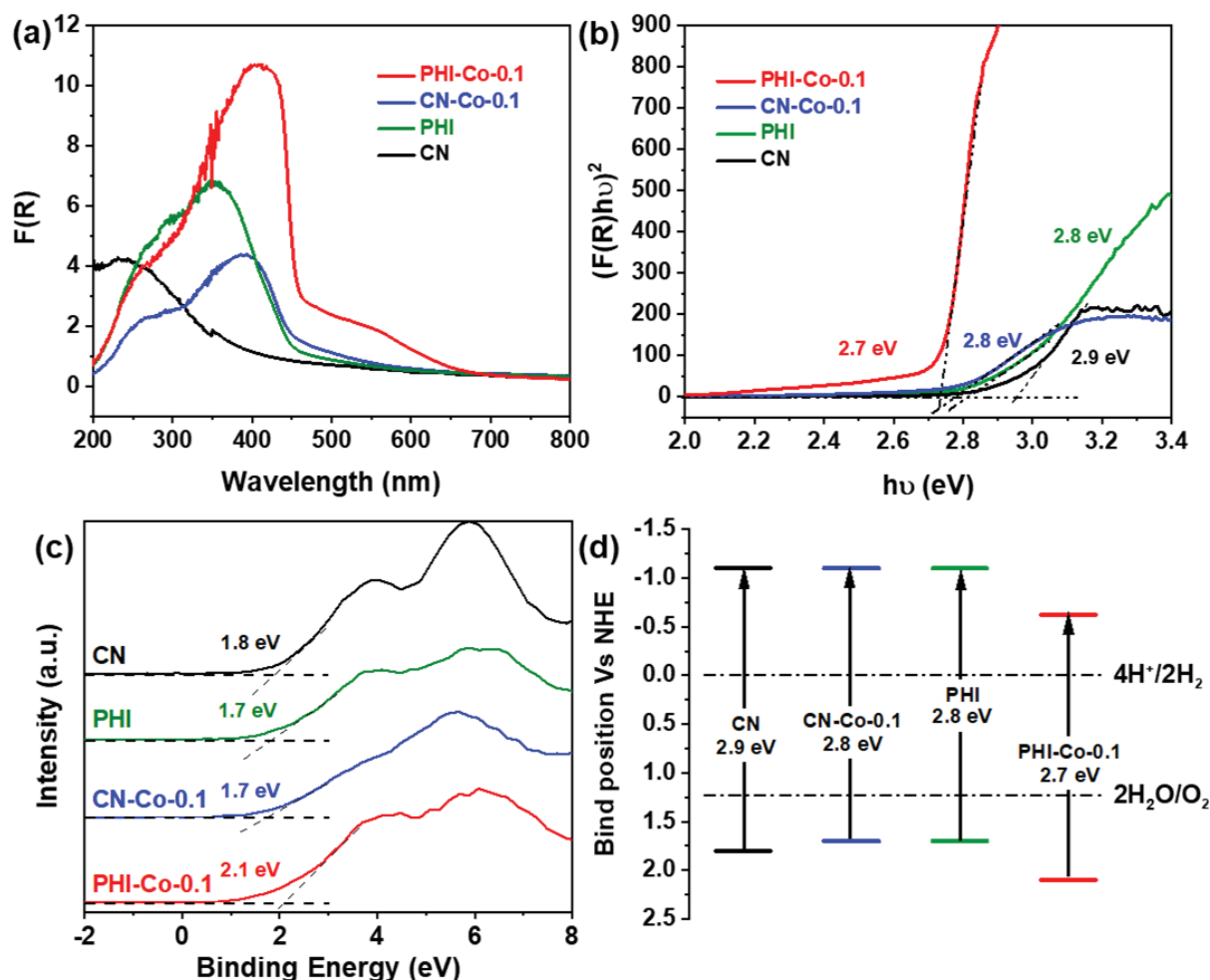


Figure 3-5. (a) UV-vis spectra of CN, CN-Co-0.1, PHI, PHI-Co-0.1, respectively. (b) Tauc plots of the catalysts derived from **Figure 3-5a**. (c) XPS VBM spectra of PHI-Co-0.1, PHI, CN, CN-Co-0.1. (d) Schematic band position of CN, CN-Co-0.1, PHI, and PHI-Co-0.1.

The UV-vis spectra in **Figure 3-5a** show that PHI exhibits a significantly enhanced light absorbance region compared to CN. PHI-Co shows a considerable pre-absorption band in the visible spectrum (460 nm - 680 nm), which might due to the intercalation of Co cations. This kind of additional, broad absorption band appearing before the absorbance edge can often be found in defected, metal-doped, or surface modified semiconductors, because some intraband gap states can be introduced during the modification¹⁸⁶. A similar but weaker pre-absorption band can also be observed in PHI (with K cations) and CN-Co, indicating that this optical pre-absorption might originate from the intercalated metal species in the polymeric structure.

Chapter 3. Cobalt intercalated poly(heptazine) imide as photocatalyst for water oxidation

The optical bandgap of the materials was calculated from the Tauc plot derived from the UV-vis absorbance measurements (**Figure 3-5b**), and the calculated bandgap widths are listed in **Table 3-1**. Typically, a Tauc plot shows the $h\nu$ on the abscissa. h is Planck constant, ν is the frequency of light. The calculation of ν follows the equation below:

$$\nu = c/\lambda \quad (3-2)$$

where c is the speed of light, λ is the wavelength from the ordinate of UV-vis spectra. The ordinate of a Tauc plot can be written as $(\alpha h\nu)^2$, where α is the absorption coefficient, which can be substituted by $F(R)$, Kubelka-Munk function, in the UV-vis spectrum. Kubelka-Munk function is developed to analyze the light absorption of inhomogeneous powder samples, which provides a simple mathematic relation between diffuse reflectance of the powder samples and their absorption coefficient^{6,170}. After the Tauc plot was derived, extrapolating the first linear region to the abscissa can obtain the optical bandgap width of the semiconductor.

To calculate the valence band maximum of PHI-Co-0.1, CN-Co-0.1, PHI and CN, XPS VBM spectra of these photocatalysts were measured (**Figure 3-5c**, **Table 3-1**). The band positions conducted from these combined measurements are summarized in **Figure 3-5d** and **Table 3-1**. Notably, despite exhibiting a very similar bandgap width compared to PHI, the valence band position of PHI-Co-0.1 has remarkably shifted to a more positive potential, which should increase its oxidation ability, thus favorable for water oxidation.

Table 3-1. Bandgap widths and band positions of PHI-Co, CN-Co, PHI, and CN.

Photocatalysts	Bandgap width (eV)	Valence band edge	Conduction band edge
PHI-Co-0.1	2.7	2.1	-0.6
CN-Co-0.1	2.7	1.8	-0.9
PHI	2.7	1.7	-0.9
CN	2.9	1.6	-1.3

Chapter 3. Cobalt intercalated poly(heptazine) imide as photocatalyst for water oxidation

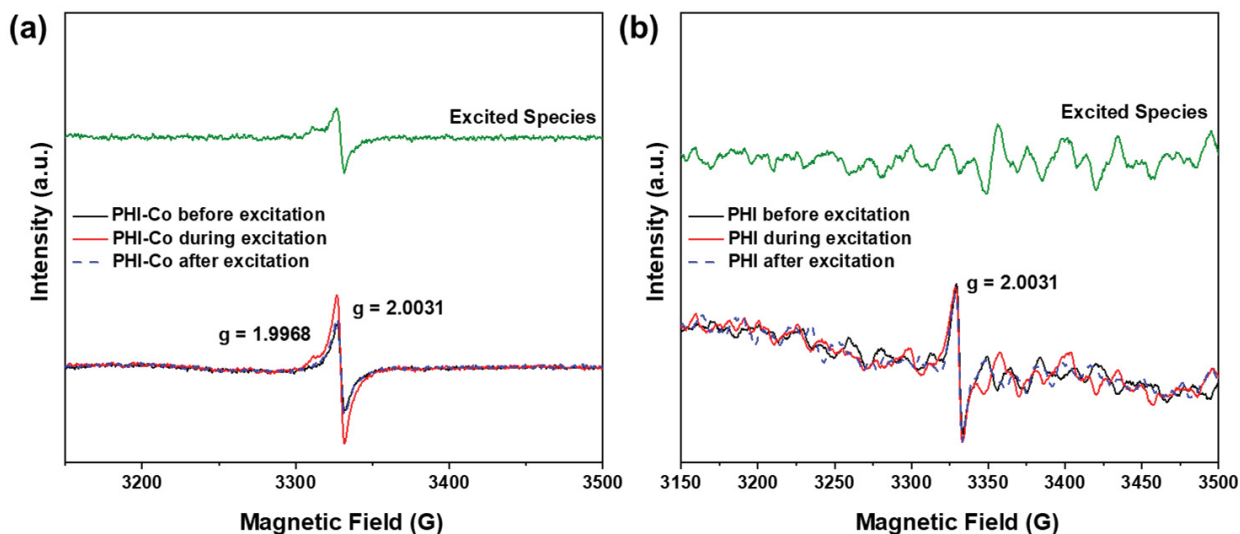


Figure 3-6. The EPR spectra of (a) PHI-Co-0.1, and (b) PHI before, during and after illumination of $\lambda > 420$ nm Xe lamp, measured with frequency 9.35 GHz

EPR studies were conducted to further understand the charge separation process in PHI-Co-0.1 and cobalt-free PHI. As depicted in **Figure 3-6a**, a narrow signal with Lorentzian lineshape can be observed at around 3331 G in the EPR spectrum of PHI-Co before illumination. In order to understand the nature of this signal, the g-factor is derived from the spectrum following the equation below:

$$g = hf / m_B B \quad (3-3)$$

where h is Planck's constant, f is the frequency where the EPR spectrum was measured, m_B is Bohr magneton, and B is the magnetic field in Tesla (where $1 \text{ T} = 1000 \text{ G}$)²⁰⁸. The g-factor value corresponding to the signal at 3331 G is 2.0031, which can be assigned to the heptazine-centered π radical¹⁵¹. The EPR spectrum of powder PHI-Co sample under illumination exhibits a significantly raised signal, comparing to its EPR spectrum in the dark, indicating a strong charge separation in PHI-Co during the illumination. Notably, a weak signal at 3316 G, corresponding to a g-value 1.9968 appears during the illumination. This signal can be assigned to the hyperfine structure of Co^{209} . On the contrary, no obvious change can be observed in the EPR spectra of PHI with or without illumination (**Figure 3-6b**), indicating the intercalation of Co has enhanced the charge separation.

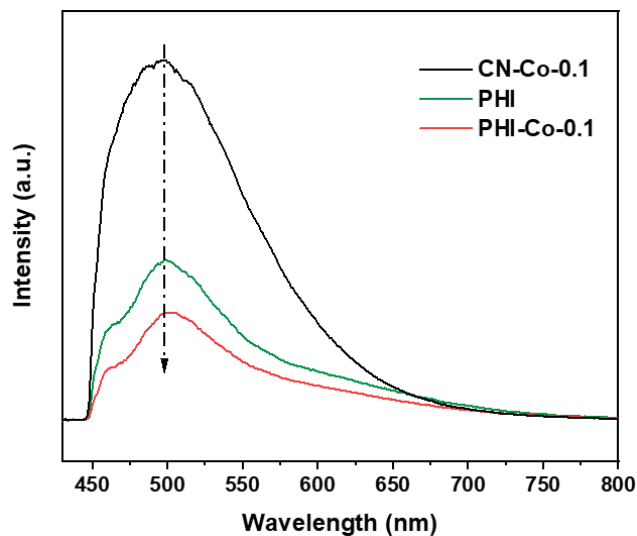


Figure 3-7. Photoluminescence spectra of PHI-Co-0.1, CN-Co-0.1, and PHI, excited by UV light with wavelength 395 nm.

After excited by UV light with a wavelength of 395 nm, the photoluminescence (PL) spectra of PHI-Co-0.1, CN-Co-0.1 and PHI are collected and presented in **Figure 3-7**. Comparing with CN-Co-0.1 and PHI, PHI-Co-0.1 shows a notably reduced intensity of its emission peak, indicates less recombination of the photo-induced charge carrier, which improves the energy conversion efficiency in PHI-Co-0.1.

Due to the abundant Co(II) active center, favorable band structure, and enhanced charge separation under visible-light illumination, PHI-Co is promising for photocatalytic water oxidation. Therefore, the photocatalytic water oxidation performance of PHI-Co's with different Co contents, CN-Co-0.1 and cobalt-free PHI was evaluated by measuring the oxygen generation of 20 mg catalysts under $\lambda > 420$ nm light irradiation in 100 mL of water in the presence of the sacrificial agent AgNO_3 and buffer La_2O_3 , which helps to stabilize the pH value around 8 - 8.5 (**Figure 3-8**).

In order to exclude the oxygen generated from the AgNO_3 sacrificial agents, which were observed in previous reports²¹⁰, the oxygen evolution of the photocatalysts were first measured for 30 min in dark in the presence of sacrificial agent AgNO_3 and buffer La_2O_3 . The oxygen generation of a blank sample, sacrificial agent AgNO_3 and buffer La_2O_3 without photocatalyst,

Chapter 3. Cobalt intercalated poly(heptazine) imide as photocatalyst for water oxidation

was also measured with visible light irradiation. The water oxidation activities shown in **Figure 3-8b** and apparent quantum yield shown below are all reported after excluding the oxygen generated by AgNO₃ sacrificial agent.

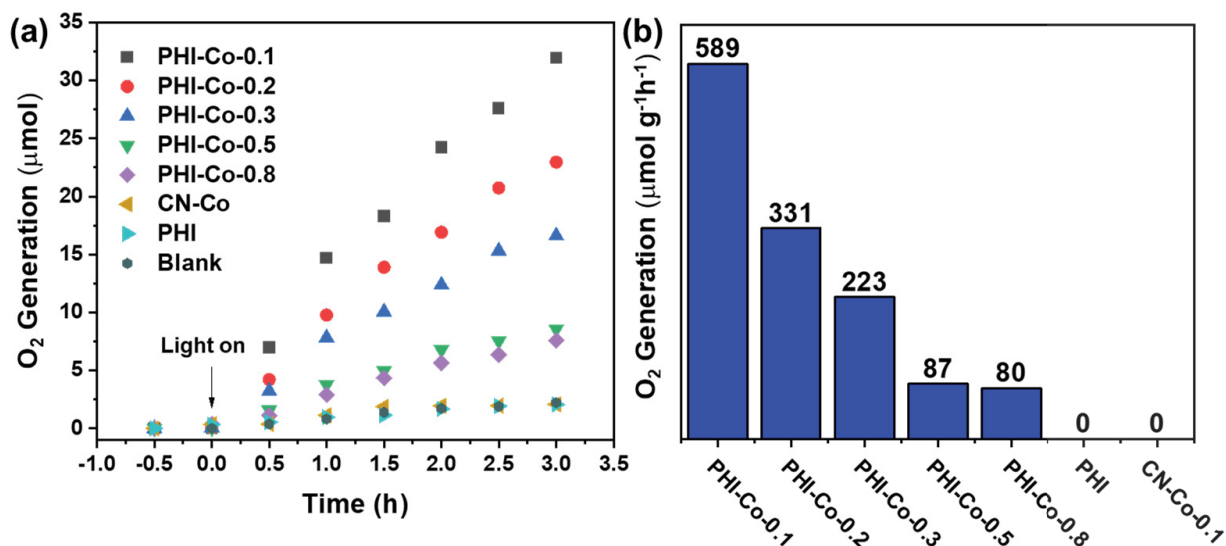


Figure 3-8. (a) Photocatalytic oxygen generation using 20 mg catalysts under >420 nm Xe lamp illumination in 100 mL of deionized water, in the presence of sacrificial agent AgNO₃ and buffer La₂O₃. A blank sample, sacrificial agent AgNO₃ and buffer La₂O₃ without catalyst is also tested. (b) Oxygen generation activity of the PHI-Co's, CN-Co-0.1 and PHI.

PHI-Co's with different Co contents generally exhibit excellent oxygen evolution activity while PHI and CN-Co were not active, proving that the intercalation of Co cations in the PHI backbone enables the PHI to catalyze the water oxidation reaction. Among the series, PHI-Co-0.1 exhibits the highest activity of 589 μmol g⁻¹h⁻¹, standing among the most efficient water oxidation photocatalysts^{25,31,122,128,129,203}.

The apparent quantum yield (AQY) of PHI-Co-0.1 was also calculated to understand the water oxidation activity of PHI-Co-0.1. The AQY is usually calculated via the equation below:

$$\text{AQY} = nR/I \quad (3-4)$$

Chapter 3. Cobalt intercalated poly(heptazine) imide as photocatalyst for water oxidation

In the equation n , R and I represent the number of electrons or holes consumed in the formation of one O_2 molecule, the quantity of gas molecules evolved within a certain time of measurement, and the number of incident photons reaching the photocatalytic system during the certain time of measurement, respectively²⁵.

The AQY is highly dependent on the wavelength of the incident light¹²². Due to the limited time, the AQY of PHI-Co-0.1 was only measured under the illumination of 420 nm monochromatic irradiation, which is a representative wavelength where the PHI-Co-0.1 photocatalyst exhibits the highest light absorbance intensity. For the AQY measurement, 20 mg PHI-Co-0.1 in 100 mL of water in the presence of the sacrificial agent $AgNO_3$ and buffer La_2O_3 . An AQY of 5.1% under 420 nm monochromatic irradiation is found in PHI-Co-0.1, which is higher than the other water oxidation photocatalysts in similar measuring conditions (1.1% for $Co_3O_4@carbon\ nitride$ ²⁰³, 2.6% for $BiVO_4:Mo$ ¹²², 2.3% for $Y_2Ti_2O_5S_2$ ²⁵, *etc.*). The high AQY of PHI-Co-0.1 indicates the high water oxidation activity of PHI-Co-0.1 is originated from the high energy conversion efficiency.

The photocatalytic water oxidation performance of PHI-Co can be assigned to different effects of the intercalated Co-ions. (1) Co(II) cations in the PHI lattice provide highly efficient active centers for water oxidation; (2) due to the intercalation of Co ions, the band position of PHI-Co shifts to more positive potentials favorable for oxygen generation from water, and (3) PHI-Co shows better charge separation and suppressed charge recombination compared to PHI and cobalt doped CN, and therefore resulting in higher energy conversion efficiency.

Conclusion

In conclusion, by introducing cobalt cations in the PHI structure, a high-performance, stable, low-cost PHI-Co photocatalyst was developed for water oxidation. The most active PHI-Co-0.1 (Co content: 0.08 wt%) has shown a visible-light-driven oxygen generation activity of $589\ \mu\text{mol h}^{-1}\ \text{g}^{-1}$. This excellent activity originated from the unique synergetic effects between PHI backbone and Co cations. On the one hand, by intercalating Co cations, the band structure of PHI-Co shifted to more positive positions, which is favorable for water oxidation. On the other

Chapter 3. Cobalt intercalated poly(heptazine) imide as photocatalyst for water oxidation

hand, the charge separation in PHI-Co is promoted under the visible-light irradiation, while the charge recombination process is suppressed. These synergetic effects lead to high energy conversion efficiency.

4 Nickel intercalated poly(heptazine) imide for photocatalytic hydrogen evolution

Motivation

Photocatalytic overall water splitting is a simple and cost-effective method to produce clean hydrogen fuel^{16,106,107}. The photocatalysts for overall water splitting need to have suitable band positions for both, hydrogen generation and water oxidation half-reactions. Meanwhile, the catalysts should show a relatively narrow bandgap width, in order to utilize the visible-light region of the solar spectrum⁷. Due to these critical demands, one-step overall water splitting is relatively difficult to achieve. Therefore, a two-step water splitting strategy was developed by combining two semiconductors and constructing a so-called Z-scheme structure^{118–120}.

Z-scheme photocatalysts are nature-inspired catalysts^{121–124}. Such a catalytic system contains one semiconductor catalyzing the hydrogen generation, while the other catalyzing the water oxidation half-reaction¹¹⁷. In the previous chapter, PHI-Co showed to be a promising candidate for the water oxidation half-reaction. To achieve overall water splitting, a suitable and easily accessible catalyst for the hydrogen generation half-reaction is needed as well.

As introduced before, PHI is an ionic carbon nitride prepared by a salt-melting-assisted method. By adjusting the salt template composition, the metal cations intercalated in the PHI backbone can be easily modified^{45–47}. Additionally, as observed in **Chapter 3**, introducing different metal cations in the PHI backbone can also lead to a remarkable band position shift, which allows the band position metal intercalated PHIs to be tuned into desired positions.

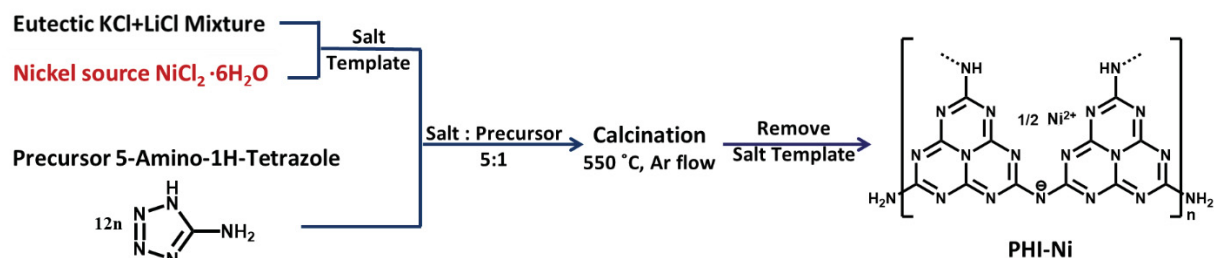
Thus, Ni cations were introduced into the PHI backbone in this chapter, yielding a high-performance nickel exchanged poly(heptazine) imide (PHI-Ni) photocatalyst for hydrogen evolution. The as-prepared PHI-Ni has a significantly narrower bandgap width compared to nickel-free PHI and exhibits a significantly more "negative" band position than PHI-Co, which is favorable for the hydrogen generation half-reaction. PHI-Ni-0.7 (Ni content 0.74 wt%)

Chapter 4. Nickel intercalated poly(heptazine) imide for photocatalytic hydrogen evolution

exhibits a photocatalytic hydrogen generation activity of $1996 \mu\text{mol g}^{-1}\text{h}^{-1}$ under illumination with visible light ($\lambda > 420 \text{ nm}$), which is 14-fold higher than Ni free PHI. The development of PHI-Ni photocatalyst comes one step closer to achieving overall water splitting with facile and non-toxic PHI-based photocatalysts.

Results and Discussion

The typical PHI-Ni synthetic process is very similar to the preparation of PHI-Co. NiCl_2 (0.2-1.5 wt%) as Ni source was added to the eutectic KCl-LiCl mixture to prepare the salt template. The mixture was then ground with 5-Aminotetrazole precursor and heated up to 550°C for 10 hours in argon flow to yield a reddish-brown PHI-Ni. The synthetic process of PHI-Ni is schematically depicted below (**Scheme 4-1**). Unless otherwise noted, the PHI-Ni in the following test refers to PHI-Ni-0.7, which contains 0.74 wt% of Ni cations, while the PHI-Co reference refers to PHI-Co-0.1 (with a Co content of 0.08 wt%).



Scheme 4-1. Synthetic process of PHI-Ni.

The contents of nickel cations in PHI-Ni's were investigated by inductively coupled plasma optical emission spectrometry (ICP-OES, **Table 4-1**). The content of Ni cations in PHI-Ni's varies from 0.20 wt% to 2.45 wt%, when 0.2-1.5 wt% of NiCl_2 was added to the salt template. The Ni cation content in PHI-Ni's increases proportionally to the increasing amount of corresponding metal salt in the salt template, depicting a similar trend as found for PHI-Co's in

Chapter 4. Nickel intercalated poly(heptazine) imide for photocatalytic hydrogen evolution

the previous chapters. This suggests that such a salt-melting method can control the type and amount of metal cations in the PHI backbones is by varying the type and amount of metal salt introduced to the salt template.

Table 4-1 Content of NiCl₂ in the salt template and corresponding content of Ni in the listed catalysts.

Sample	Ni in PHI-Ni (wt%)	NiCl ₂ in salt template (wt%)
PHI-Ni-0.2	0.20	0.2
PHI-Ni-0.4	0.42	0.4
PHI-Ni-0.7	0.74	0.6
PHI-Ni-1.2	1.23	1.0
PHI-Ni-2.5	2.45	1.5

X-ray powder diffraction (XRD) patterns of PHI-Ni with different Ni contents were measured and compared with transition-metal-free PHI to study their crystallinity (**Figure 4-1**). The refined XRD patterns of PHI (with K cations), calculated based on the PHI structure from a previous report¹⁵³ and the obtained experimental data is also plotted in **Figure 4-1**. Notably, the PHI-Ni-0.2 and PHI-Ni-0.4 exhibit significantly enhanced crystallinity compared to Ni-free PHI, suggesting the existence of a low amount of nickel salt might be favorable for the condensation of the tetrazole precursor. Except for the two major diffraction peaks at 8.3° and 27.0°, corresponding to the periodicity of heptazine units and interplanar stacking of the layers, respectively⁴⁹, the XRD patterns of PHI-Ni also exhibits notable peaks at 28.3° and 30.8°, which can both be found in the refined XRD patterns of PHI. The crystallinities of PHI-Ni's then decrease with the increase of intercalated Ni cation, the same trend is also observed in PHI-Co with increasing Co contents.

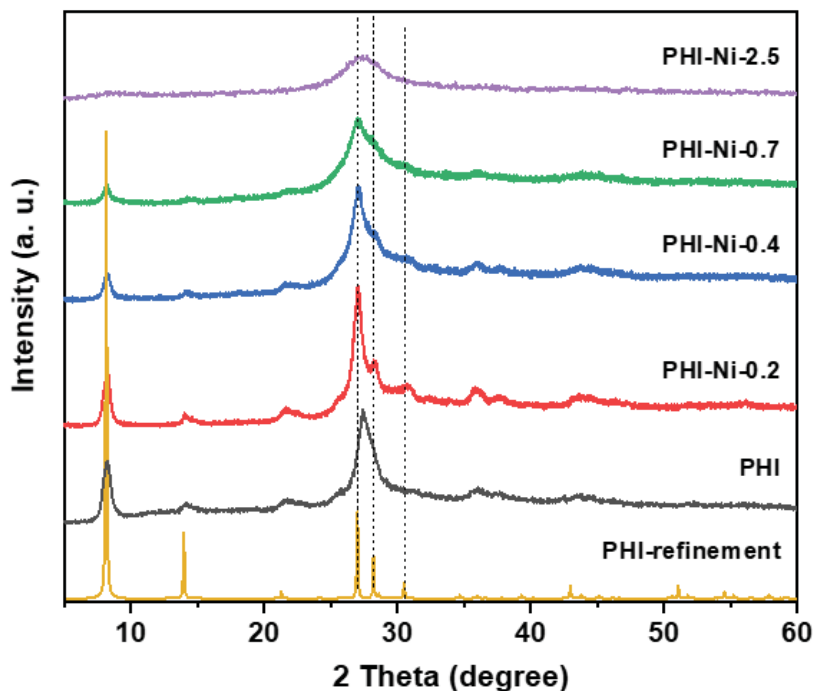


Figure 4-1 XRD patterns of PHI-Ni with different Ni contents and PHI.

The chemical states of the elements in PHI-Ni were studied via X-ray photoelectron spectroscopy (XPS, **Figure 4-2**). The N and C species found in the N 1s and C 1s PHI-Ni are very similar to those in PHI and PHI-Co (**Figure 4-2a, b**). The peaks at 398.5 eV and 400.7 eV in the PHI-Ni N 1s spectrum can be addressed to the C-N=C (ring N in heptazine unit) and N-C₃ (central N in heptazine unit), respectively¹⁵⁵, while the contribution in the C 1s spectrum at 288.0 eV corresponds to N-C=N, that is the ring C in heptazine unit. Besides these major contributions, the small contribution at 399.4 eV in N 1s spectra of PHI and PHI-Co, can be assigned to N bridges between the heptazine rings and the peaks in the C 1s spectrum at 284.8 eV and 286.4 eV corresponds to adventitious carbon and hydroxylated surface carbon atoms, respectively¹⁵². In **Figure 4-2c**, despite the lack of a signature satellite feature, a doublet peak in the XPS Ni 2p spectrum can be found at 854.1 eV, corresponding well with Ni(II) species^{156,211}. Meanwhile, no trace of nickel oxides can be found in the O 1s XPS spectrum (**Figure 4-2d**).

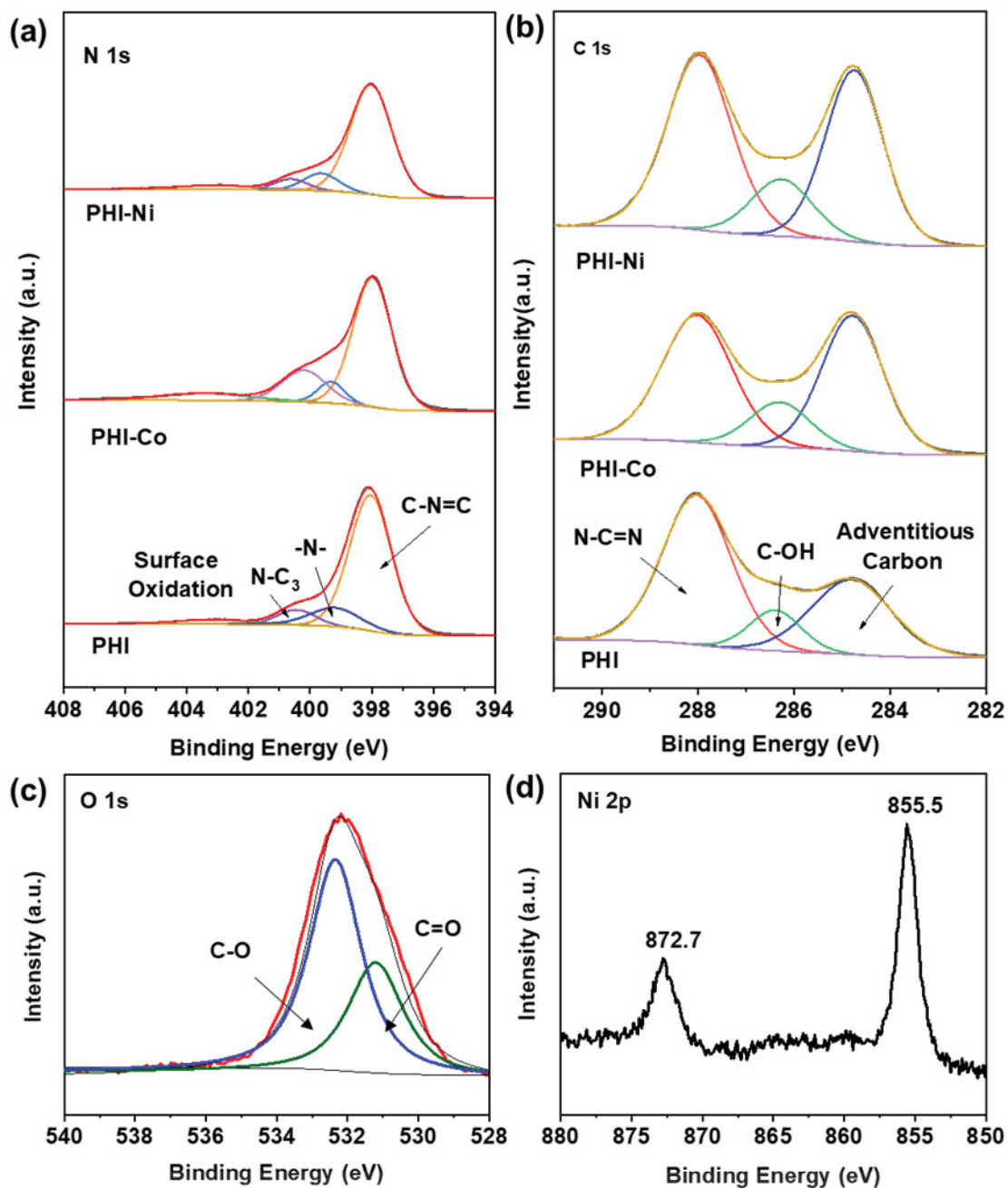


Figure 4-2 (a) N 1s, (b) C 1s, (c) Ni 2p and (d) O 1s XPS spectra of PHI-Ni compared with PHI-Co and PHI.

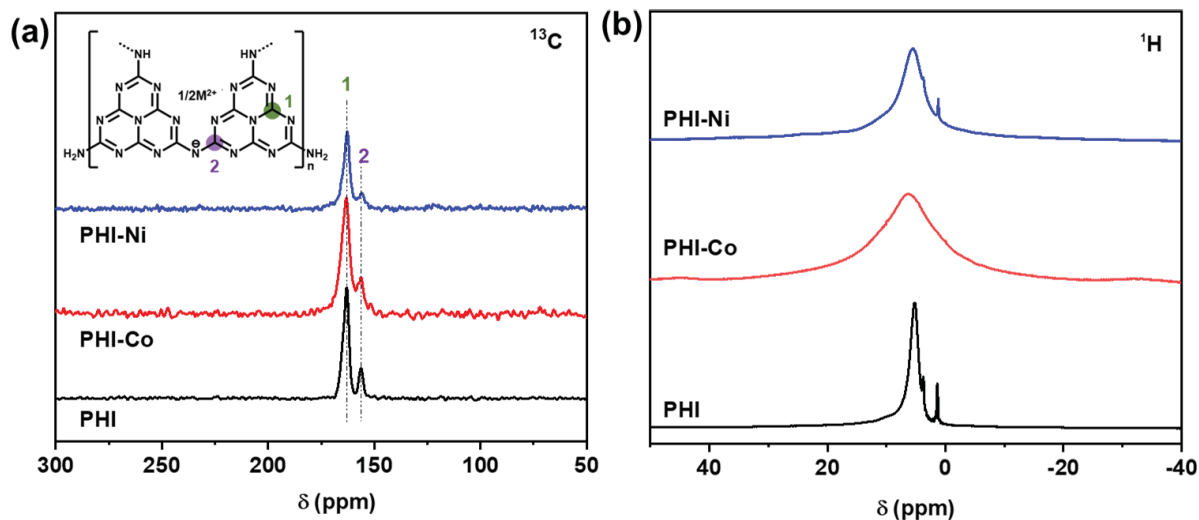


Figure 4-3 (a) ^{13}C and (b) ^1H NMR spectra of PHI-Ni, PHI-Co and PHI, respectively.

The similarity of the PHI-Ni, PHI-Co and PHI is further proved by their ^{13}C nuclear magnetic resonance (NMR) spectra (**Figure 4-3**). Typically, the C-N₃ (central carbon atom) in the heptazine unit exhibits a chemical shift of 157 ppm (1 in **Figure 4-3a**), and the signal at 163 ppm (2 in **Figure 4-3a**) is attributed to a peripheral carbon atom next to the imide bridges^[129]. The two ^{13}C signals can both be observed in all PHI, PHI-Co and PHI-Ni samples, once again suggests that the PHI basic structure stays intact when different cations are intercalated into the polymeric lattice. It can also be observed in **Figure 4-3b**, the ^1H NMR spectra of the PHI-Co and PHI-Ni are significantly broadened comparing with the ^1H NMR spectrum of PHI, and the resolution of the spectra notably decreased, which is due to the existence of paramagnetic Co(II) and Ni(II) in the structure²¹².

Chapter 4. Nickel intercalated poly(heptazine) imide for photocatalytic hydrogen evolution

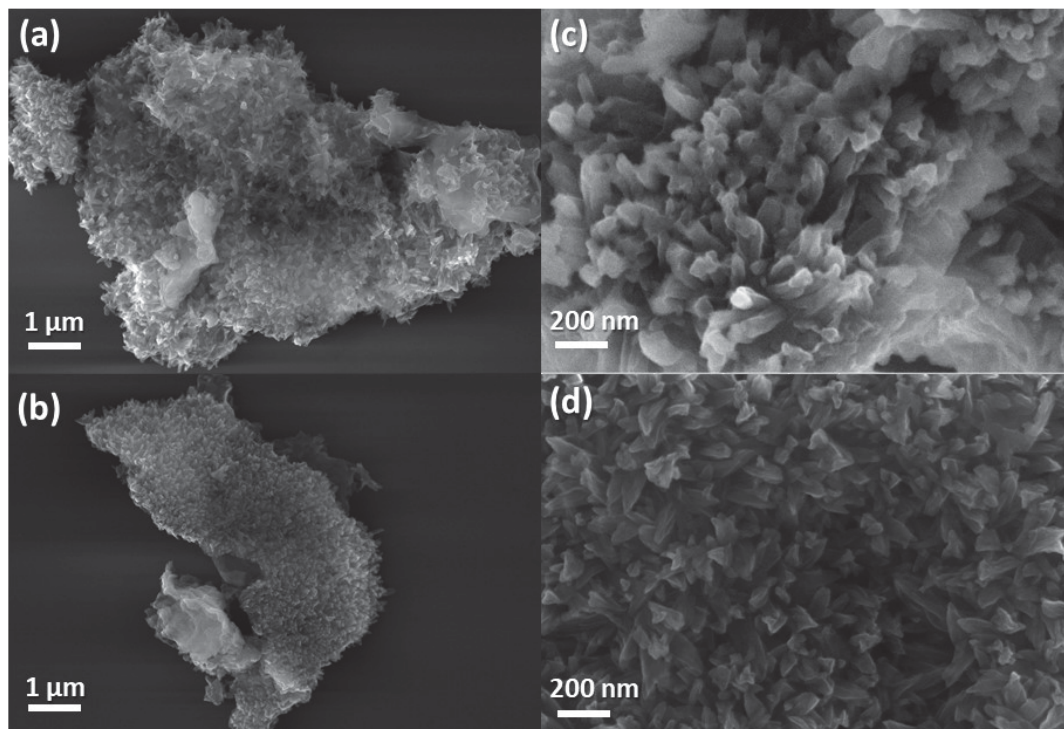


Figure 4-4 SEM images of (a, b) PHI in magnifications of 10kx and 50kx and (c, d) PHI-Ni in magnifications of 10k and 50k, respectively.

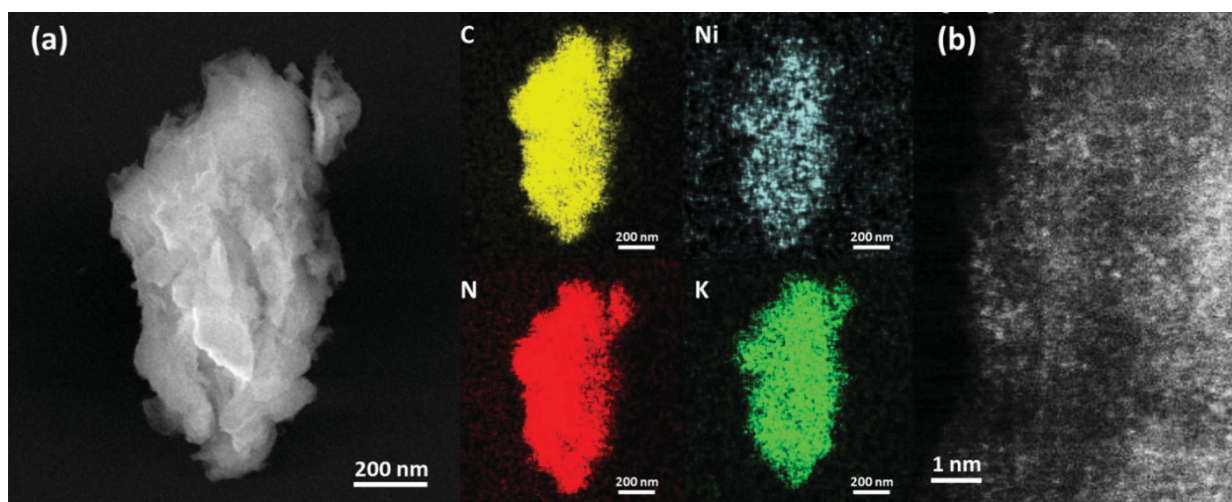


Figure 4-5 (a) SEM image of PHI-Ni with EDX elemental mapping with C, N, Ni, K inset on the right. (b) High-resolution ADF-STEM of PHI-Ni.

Chapter 4. Nickel intercalated poly(heptazine) imide for photocatalytic hydrogen evolution

PHI-Ni shows very similar morphology to PHI in scanning electron microscopy (SEM) measurements (**Figure 4-4**). No nanoparticles are observed at the magnification of 50k after the intercalation of Ni cations. The distribution of Ni cations in PHI-Ni was studied via an Energy Dispersive X-ray (EDX) detector coupled with the scanning electron microscope and annular dark-field scanning transmission electron microscopy (ADF-STEM, **Figure 4-5**). Note that due to the high voltage (15 KV) applied to collect the EDX signal for Ni element, the coral-like structure on the surface of PHI-Ni can no longer be observed in **Figure 4-5a**. The elemental mapping area (**Figure 4-5a inset**) shows that the signal of Ni can be observed homogeneously distributed over the entire sample. The annular dark-field scanning transmission electron microscopy (HR ADF-STEM) images of PHI-Ni (**Figure 4-5b**) show bright dots of metal cations dispersed in the darker PHI matrix, further confirming the Ni cations in PHI structure are dispersed individually at the atomic level.

UV-vis absorption and XPS valence band maximum (VBM) spectra of PHI-Ni were measured and compared with PHI-Co, PHI, and polymeric carbon nitride (CN) to study the light response region and band structure of PHI-Ni. From the UV-vis spectra it can be observed (**Figure 4-6a**), that PHI-Ni and PHI-Co exhibit broader light absorbance regions than PHI and CN. Between them, the reddish-brown PHI-Ni shows excellent absorption that almost covers the whole visible light spectrum.

The bandgap and band position of PHI-Ni, PHI-Co, and PHI were calculated from the Tauc plot (**Figure 4-6b**) and VBM spectra (**Figure 4-6c**). A band position diagram of PHI-Ni, PHI-Co, and PHI is depicted in **Figure 4-6d**. The calculated band positions are listed in **Table 4-2**. PHI-Ni exhibits a much narrower bandgap width comparing with PHI, leading to an extended light absorbance region. Meanwhile, unlike PHI-Co, PHI-Ni's conduction band remains in a relatively negative position, which can be favorable for the hydrogen evolution. This result again confirms that the intercalating of different metal cations can tune the band positions of PHI-based catalysts.

Chapter 4. Nickel intercalated poly(heptazine) imide for photocatalytic hydrogen evolution

Table 4-2 Bandgap widths and band positions of PHI-Ni, PHI-Co and PHI.

Photocatalysts	Band gap (eV)	Valence band edge	Conduction band edge
PHI-Ni	2.0	1.3	-0.7
PHI-Co	2.7	2.1	-0.6
PHI	2.7	1.5	-1.2

The shift of band positions in PHI-Co and PHI-Ni, compared with PHI might be due to the change of electron distribution in the structure. The highest occupied molecular orbital (HOMO) and (LUMO) of PHI, PHI-Co and PHI-Ni were stimulated via DFT calculation after introducing transition metal cations into the PHI structure. The DFT calculation is applied to PHI based on the molecular structure of PHI with potassium cations reported by Lotsch *et. al.*¹⁵³. For the calculation of PHI-Co and PHI-Ni, the K cations are completely exchanged by Co and Ni cations with the molar ratio of Co/Ni : K = 1:2, respectively. The HOMO and LUMO states of PHI, PHI-Co and PHI-Ni are presented in **Figure 4-7**. In PHI, the electrons are distributed on PHI polymeric lattice in both of the HOMO and LUMO state, while in PHI-Co and PHI-Ni, the electrons intend to accumulate on the transition metal cations, i.e. Co and Ni, respectively. The results indicate that when transition metal cations are introduced into the PHI lattice, the distribution of electrons can be altered accordingly, explaining the band position shift in PHI-Co-0.1 and PHI-Ni-0.7. It should be noted that in the best-performing PHI-Co-0.1 and PHI-Ni-0.7, a large number of K cations still exist in the structure, the actual electron distributions in the PHI-Co-0.1 and PHI-Ni-0.7 are possibly in between the ones calculated for pure PHI-K and PHI-Co or PHI-Ni, respectively.

Chapter 4. Nickel intercalated poly(heptazine) imide for photocatalytic hydrogen evolution

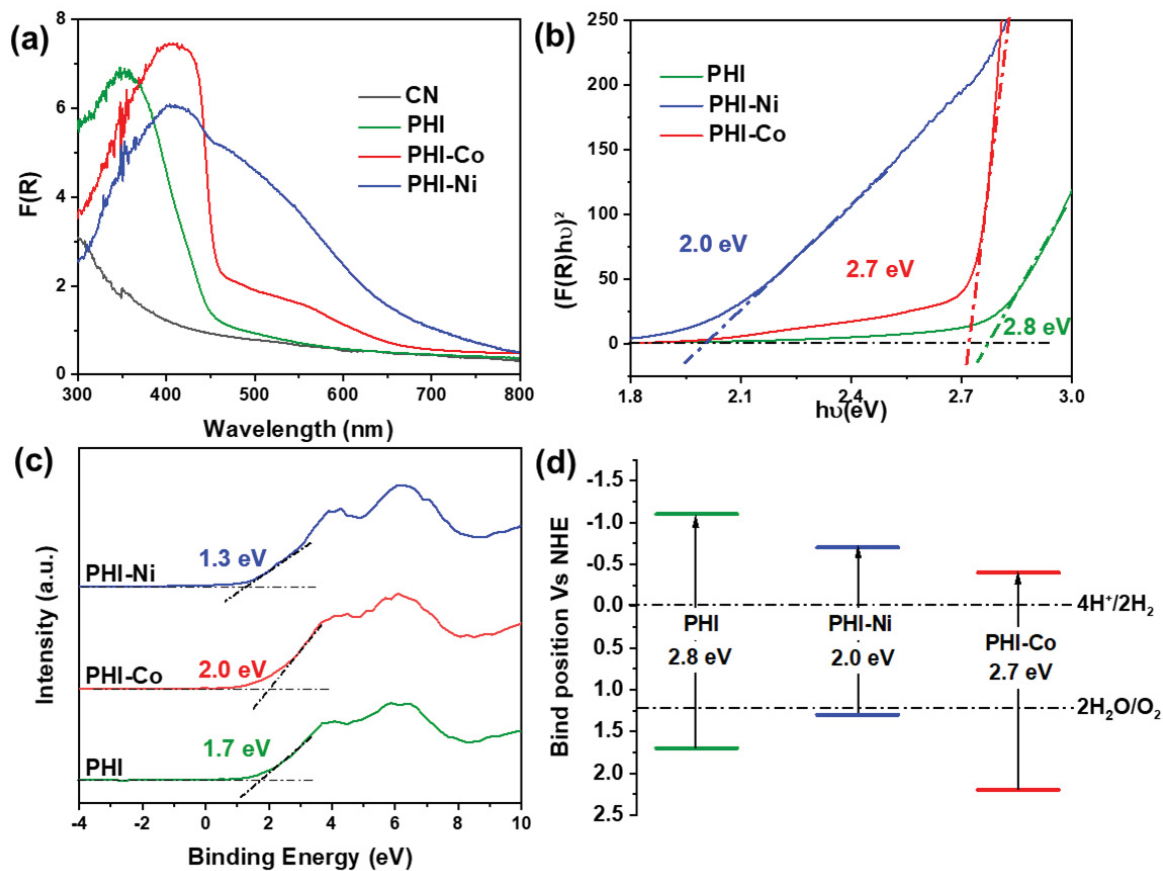


Figure 4-6 (a) UV-vis spectra of PHI-Ni, PHI-Co and PHI, respectively. (b) Tauc plots of the catalysts derived from **Figure 4-6a**. (c) XPS VBM spectra of PHI-Ni, PHI-Co and PH; (d) Schematic band position of PHI-Ni, PHI-Co and PHI.

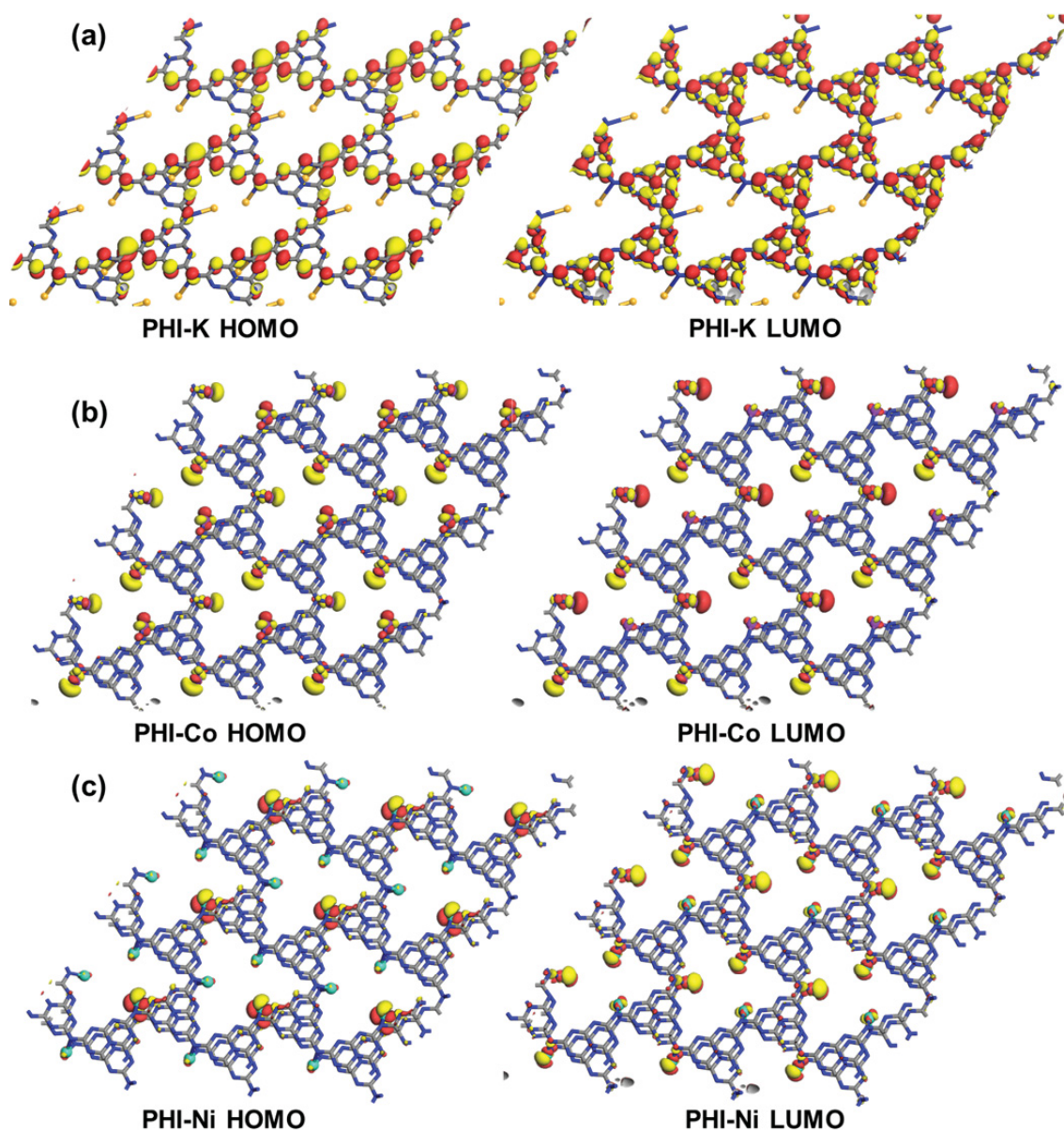


Figure 4-7 HOMO and LUMO of (a)PHI, (b)PHI-Co and (c) PHI-Ni.

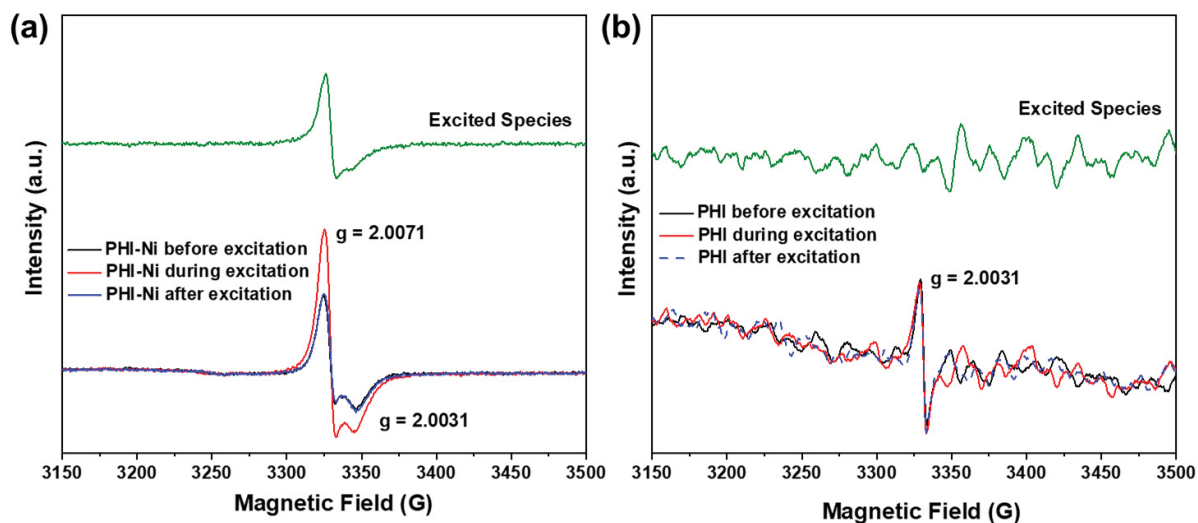


Figure 4-8 The EPR spectra of (a) PHI-Ni and (b) PHI before, during and after illumination of $\lambda > 420$ nm Xe lamp, the EPR spectra were measured with frequency ~ 9.3 GHz.

The optical property of PHI-Ni was further studied by an in-situ solid-state electron paramagnetic resonance (EPR) spectroscopy and compared with nickel-free PHI. In-situ EPR spectroscopy can be used to investigate charge separation processes of the samples during visible light radiation. As depicted in **Figure 4-8a**, two signals can be observed in the typical EPR spectrum of PHI-Ni, with g-factor values 2.0031 and 2.0071, respectively. The former signal corresponds to the heptazine-centered π radical, which can also be observed in the EPR spectrum of PHI¹⁵³. The latter signal can be attributed to the Ni²⁺ cations²⁰⁸. The EPR spectrum of powder PHI-Ni sample under illumination exhibits a raised signal comparing to its EPR spectrum in the dark. The enhanced signal under illumination indicates a strong charge separation in PHI-Ni. Meanwhile, no obvious signal intensity change can be observed in the EPR spectra of PHI before and during the illumination (**Figure 4-8b**), indicating the intercalation of Ni remarkably enhanced the charge separation.

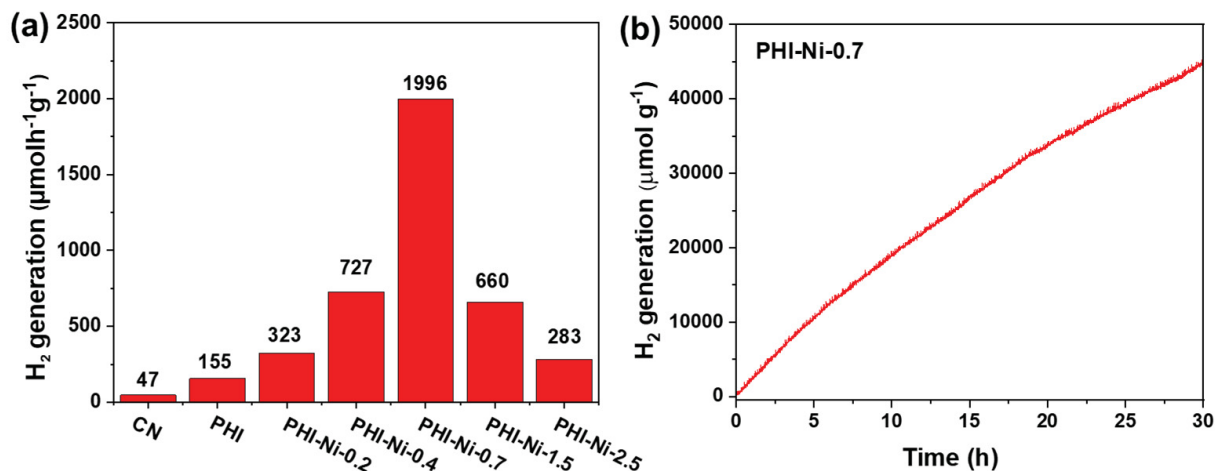


Figure 4-9 (a) Hydrogen generation activities of PHI-Ni with different Ni content comparing to nickel-free PHI under 300W Xe lamp illumination, 10 mg catalyst was measured with $\lambda > 420$ nm cutoff filter. 3 wt% Pt was applied as co-catalyst and 20 vol% triethanolamine (TEOA) was introduced as the sacrificial agent. (b) Best performed PHI-Ni-0.7 running a 30 h stability test under aforementioned measuring conditions.

The photocatalytic hydrogen generation activity of PHI-Ni with different Ni content was evaluated by photocatalytic hydrogen evolution in a pressure detecting reactor under 300W Xe lamp illumination, with 10 mg catalysts, $\lambda > 420$ nm cutoff filter, 3 wt% Pt as co-catalyst and 20 vol% triethanolamine (TEOA) as the sacrificial agent. As seen in **Figure 4-9a**, the PHI-Ni samples are generally more active than PHI in hydrogen generation reactions. The best-performing PHI-Ni-0.7 photocatalyst exhibited remarkable photocatalytic hydrogen generation activity of $1996 \mu\text{mol g}^{-1} \text{h}^{-1}$ under the illumination of visible light ($\lambda > 420$ nm), which is 14-fold higher than Ni free PHI and 42-fold higher than polymeric CN. The stability test of PHI-Ni-0.7 was run for 30 h with TEOA as the sacrificial agent with a starting concentration of 20 vol% (**Figure 4-9b**). After 20 h of the stability test, PHI-Ni-0.7 kept 90% of its activity, after 30 h, 75% of PHI-Ni-0.7's activity remained.

The catalyst was collected after the photocatalytic hydrogen generation reaction, and the crystallinity of the recovered sample was measured by XRD and compared with that of the pristine PHI-Ni-0.7. It can be observed in **Figure 4-10**, the crystallinity of PHI-Ni-0.7 mostly remains. The SEM images of PHI-Ni before and after the photocatalytic reaction is shown in

Figure 4-11. The morphology of PHI-Ni is unchanged after the photocatalytic reaction. No observable Ni nanoparticles nor agglomerated Pt co-catalysts can be found on the surface of PHI-Ni.

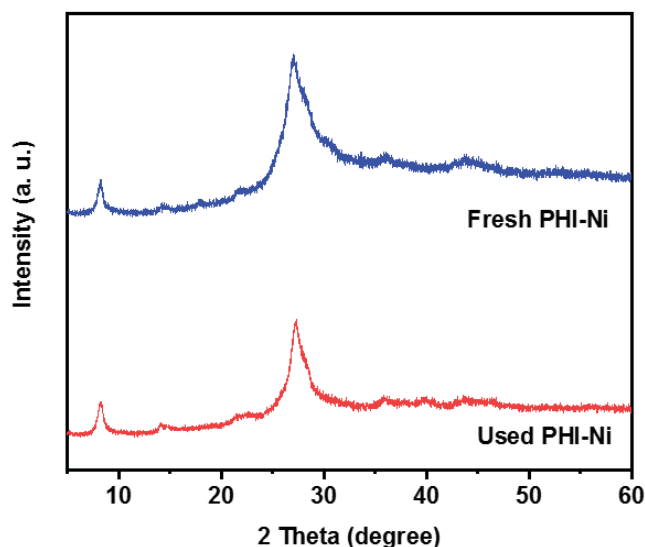


Figure 4-10 XRD patterns of PHI-Ni-0.7 before and after the photocatalytic reaction.

The photocatalytic hydrogen evolution activity of PHI-Ni is owed to the synergetic effects between the intercalated Ni ions and the PHI backbone. On the one hand, the intercalation of Ni enhances the light response region of the catalyst, while the conduction band position in the favorable potential for hydrogen generation remains. The intercalated Ni cations in the PHI structure serve as “electron wells”, changing the electron distribution in the HOMO and LUMO state of PHI-Ni, and, therefore, results in the shift of band position in PHI-Ni. On the other hand, the intercalation of Ni leads to better charge separation in the photocatalyst, leading to better use of the photo-induced charge carrier.

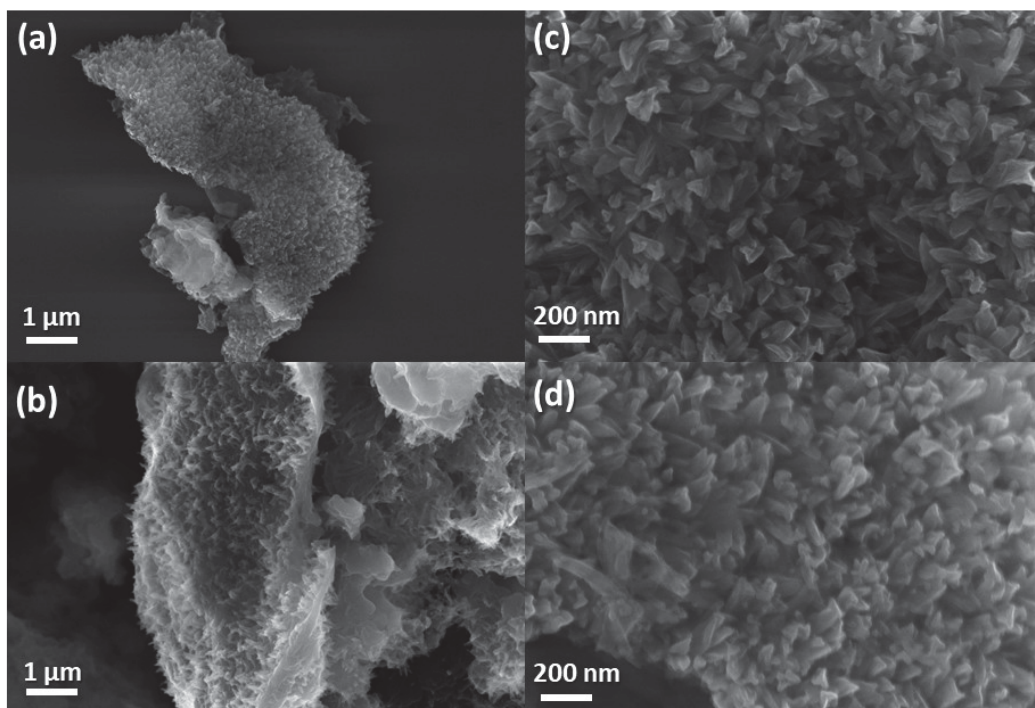


Figure 4-11 SEM images of PHI-Ni (a,b) before and (c,d) after photocatalytic reaction in magnifications of 10k and 50k, respectively.

Conclusion

In this chapter, by introducing nickel cations in the PHI structure, an efficient hydrogen generation photocatalyst was developed. The most active PHI-Ni-0.7 shows visible-light-driven hydrogen generation activity of $1996 \mu\text{mol g}^{-1} \text{h}^{-1}$, which is more than 14-fold higher than Ni-free PHI and 42-fold higher than polymeric CN.

Chapter 4. Nickel intercalated poly(heptazine) imide for photocatalytic hydrogen evolution

5 Exploration of transition-metal- and noble-metal-intercalated poly(heptazine) imides

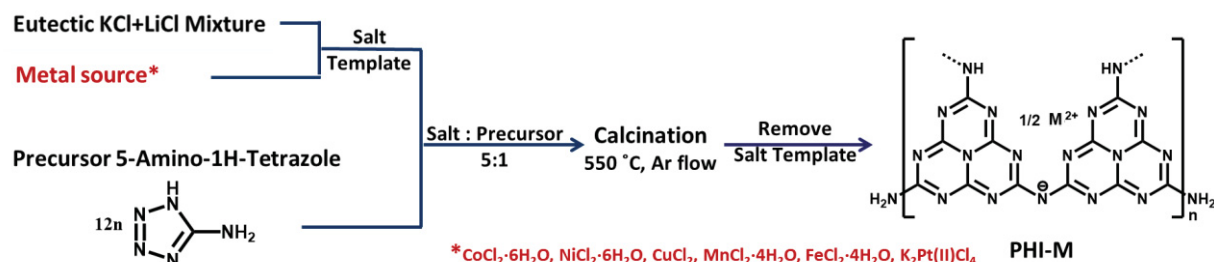
Motivation

Metal active sites are widely used in various catalytic applications^{41,60,213}. When the metal active sites are downsized to subnanoscale, their catalytic activity and selectivity can be significantly improved because of the surface atom unsaturation, and potential quantum size effects^{40,67,214}. To construct high-performance catalysts with these metal active sites, supporting materials that can disperse and stabilize the metal atoms/subnano clusters are in high demand^{98,164}.

PHI is prepared by the condensation of 5-aminotetrazole in presence of a eutectic LiCl-KCl salt-melt^{44,152}. In the PHI structure, the heptazine units are linked by negatively charged imide bridges⁴⁴. The salt-melt-assisted synthesis introduces a large number of K cations to the PHI structure to counterbalance the negative charge from the imide sites^{23,151}. These K cations can be replaced by a variety of alkali and transition metal cations via a post-synthesis ion exchange process⁴⁹. This intriguing property enables PHI to disperse and stabilize various metal active sites at an atomic level. This makes PHI a promising substrate material for designing highly efficient catalysts⁴⁰.

However, this post-synthesis ion exchange method usually requires a time-consuming dialysis process, and cannot efficiently control the amount of introduced metal cations⁴⁹. Therefore, in order to gain better control over the amount of the metal active sites in the metal-intercalated PHI, a modified salt-melt-assisted method was developed as described in the previous chapters. This salt-melt-assisted condensation process is shown in a generalized form **Scheme 5-1**. In such a synthetic process, the types and amounts of metal cations in the PHI product can be modified, by altering the types and amounts of metal salt in the salt template.

Chapter 5. Exploration of other transition metal and noble metal exchanged ploy(heptazine) imides



Scheme 5-1 Schematic synthesis procedure of transition- and noble-metal-intercalated PHI.

In this chapter, a selection of transition-metal-, noble-metal, and bi-metal-intercalated PHI was synthesized by this salt-template-assisted method, to prove its versatility for preparing metal intercalated PHIs. The structures of these metal-intercalated poly(heptazine) imides (denoted as PHI-M, M = Cu, Fe, Mn, Pt...) are investigated. Additionally, the optical band structure of many PHI-M's are measured, showing the same trend as observed in chapter 3 and chapter 4, *i.e.* the band structure of PHI can be tuned via introducing different cations into the PHI structure.

Results and discussions

Synthesis and structure of first-row transition metal intercalated poly(heptazine) imides

In this section, the first-row transition metals Cu, Fe and Mn, are introduced to the PHI polymeric lattice, respectively. The synthetic processes to produce these transition metal exchanged poly(heptazine) imides (noted as PHI-M, M= Cu, Mn, Fe) are very similar to that of PHI-Co and PHI-Ni in the previous chapters. CuCl₂, FeCl₂·4H₂O, MnCl₂·4H₂O as the sources of transition metal cations were added to the eutectic KCl-LiCl mixture, respectively, to prepare the salt template. The salt template was then ground with 5-Aminotetrazole precursor and heated up to 550°C for 8 h in argon flow. The resulting solids are washed with water for 24 h to obtain the PHI-M samples. A more detailed description of this synthetic procedure can be found in **Chapter 7 Experimental section**.

Chapter 5. Exploration of other transition metal and noble metal exchanged poly(heptazine) imides

The crystallinity of as-obtained PHI-Cu, PHI-Mn, and PHI-Fe were examined by X-ray powder diffraction (XRD, **Figure 5-1**). The layer stacking peak at 27° can still be observed, however, the intensity of the peak at 8° , which corresponds to the in-plane ordered heptazine ring, is reduced in the XRD patterns of PHI-Cu and PHI-Fe, and can barely be observed in PHI-Mn¹⁵². Some of the smaller and broader diffraction peaks in PHI centered at 14.1° , 23.8° and 36.3° , which can be assigned to the $(\bar{1}20)$, $(0\bar{1}1)$, and $(23\bar{1}/32\bar{1})$ facets¹⁵¹, can be observed in PHI-Cu and PHI-Fe, but not in PHI-Mn. A peak appears at 19.2° in the XRD pattern of PHI-Mn, which was not found in the XRD patterns of PHI-Cu, PHI-Fe and PHI. However, a small diffraction peak at the similar position was reported by Lotsch *et. al.* in their ampoule crystallized PHI¹⁵³. The different crystallinity of these PHI-M's indicates that different metal salts might influence the condensation of the PHI precursor.

The chemical states of elements in PHI-Cu were studied via XPS and AES (Auger electron spectroscopy) and presented in **Figure 5-2**. The N 1s and C 1s XPS spectra of PHI are also presented in **Figure 5-2a, b** as reference. In N 1s XPS spectra of PHI-Cu (**Figure 5-2a**), the peaks at 398.3 eV and 400.9 eV can be assigned to the C-N=C (ring N in heptazine unit), N-C₃ (central N in heptazine unit), respectively while the contribution at 399.6 eV corresponds to N bridges between the heptazine rings. The significant contribution in the C 1s spectrum at 287.9 eV can be assigned to N-C=N in the heptazine unit. The peaks at 284.8 eV and 286.5 eV can be attributed to adventitious carbon and hydroxylated surface carbon atoms, respectively (**Figure 5-2b**)¹⁵². The other small peaks appearing in the C 1s spectra at 288.8 eV and in the N 1s spectra at 404.1 eV indicate surface oxidation¹⁵⁵. All these peaks can also be found in the N 1s and C 1s spectra of PHI, indicating that PHI-Cu has the typical PHI backbone, in which imide bridges connected the heptazine ring units

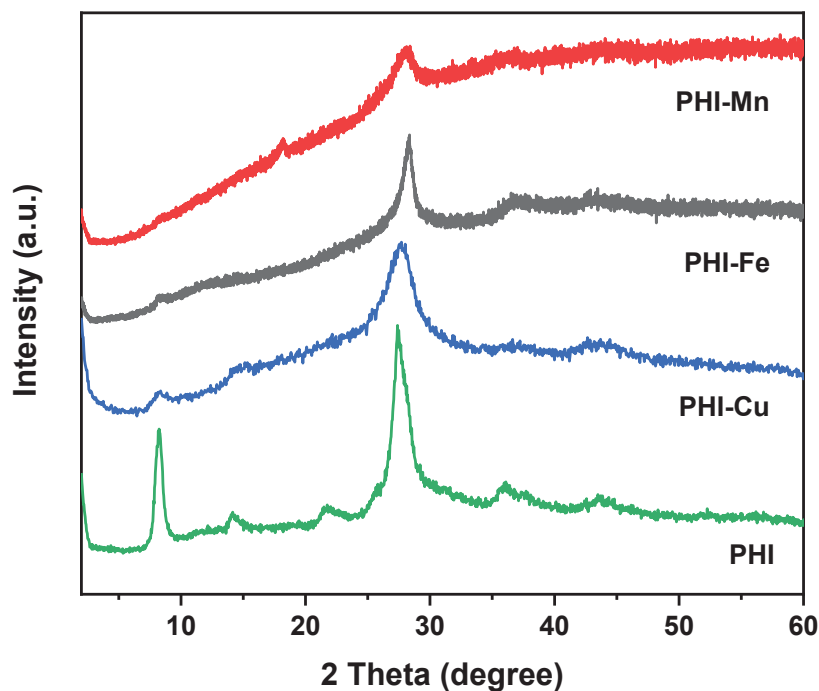


Figure 5-1 XRD patterns of PHI-Mn, PHI-Fe, PHI-Cu, and transition-metal-free PHI.

Cu cations in PHI-Cu can be detected from the Cu 2p XPS spectrum and LMM Auger peak (**Figure 5-2c,d**), showing 0.8 wt% of Cu. As observed in **Figure 5-2c**, the duplet peak in the XPS Cu 2p spectrum can be found at 932.4 eV with a weak satellite feature, which can be assigned to Cu(I) or Cu(0) oxidation states²¹⁵. The Cu(I) and metallic Cu share very similar peak positions in Cu 2p. Therefore, the Cu LMM spectrum is employed to identify Cu cation's oxidation state in PHI-Cu (**Figure 5-2d**). The Cu LMM Auger peak of PHI-Cu shows a peak at 570.2 eV, which is the typical signal for Cu(I), usually appearing at binding energy significantly higher than metallic Cu or CuO with Cu(II)²¹⁶. Meanwhile, no hint of metal oxidation contribution, which usually centers at 529-530 eV, can be observed in the O 1s spectrum of PHI-Cu (**Figure 5-2e**), confirming that the Cu exists as Cu⁺ cations in the PHI structure¹⁵⁴.

Despite CuCl₂ metal salt with an oxidation state of Cu(II) was introduced in the salt template, the Cu(II) has been reduced to Cu(I) in the PHI structure. This might happen because the condensation of tetrazole occurs at high temperatures and in an inert atmosphere without

Chapter 5. Exploration of other transition metal and noble metal exchanged ploy(heptazine) imides

moisture. In such conditions, Cu(I) with a d10 system with completely filled orbitals should be more stable than Cu(II) with d9 configuration. Besides, the condensation of tetrazole generates NH_3 with high reducibility^{44,152}, which might help to convert the Cu(II) into Cu(I) during the condensation. Eventually, this oxidation state of Cu(I) remains in PHI-Cu.

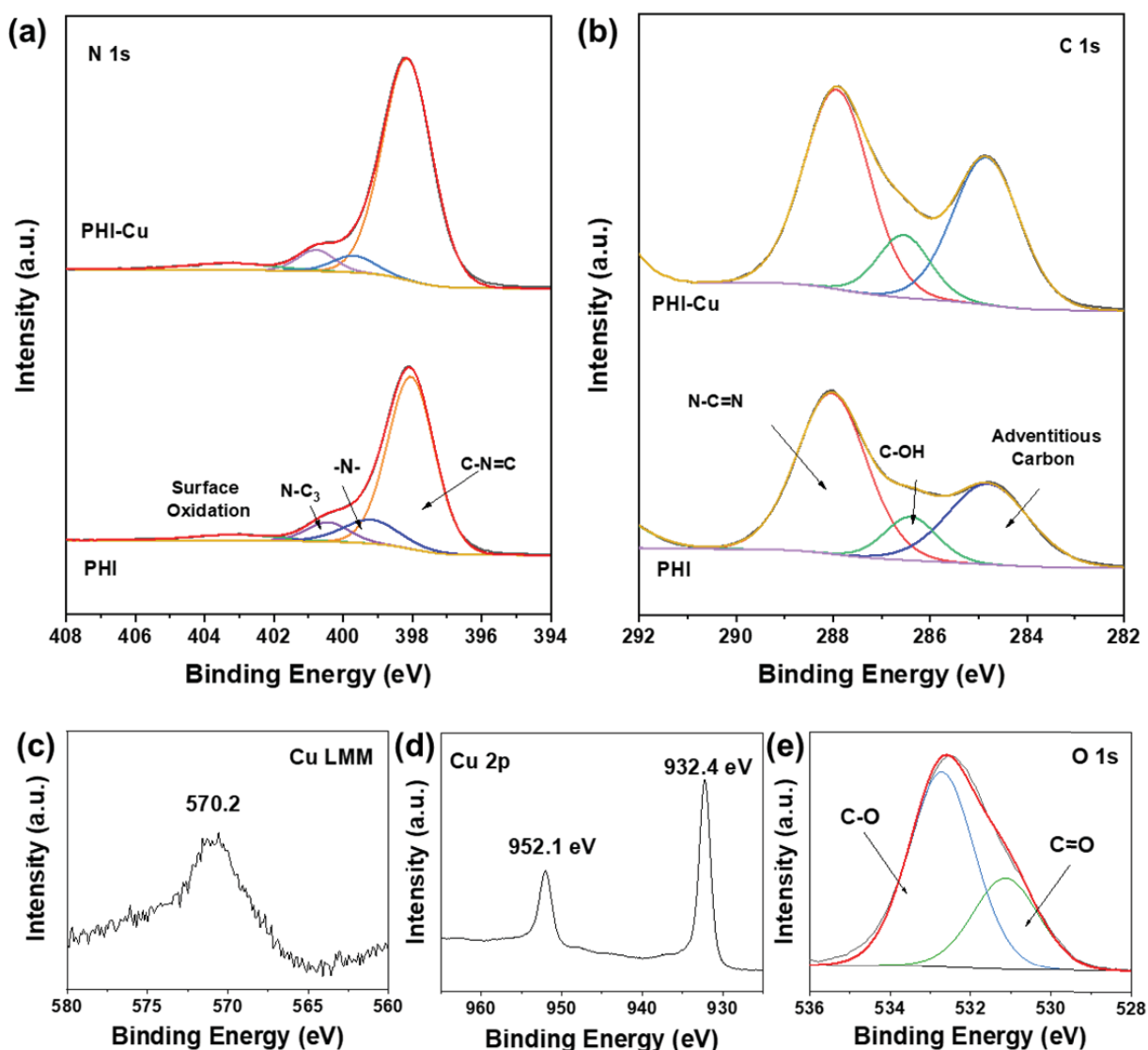


Figure 5-2 (a) N 1s, (b) C 1s, spectra of PHI-Cu and PHI. (c) Cu 2p, (b) Cu LMM and (e) O 1s spectra of PHI-Cu.

Chapter 5. Exploration of other transition metal and noble metal exchanged ploy(heptazine) imides

The chemical states of elements in PHI-Fe were investigated via XPS spectra and shown in **Figure 5-3**. The N 1s and C 1s spectra of PHI-Fe are very similar to the corresponding N 1s and C 1s spectra of PHI, indicating that after the intercalation of Fe, the basic structure of PHI backbone can be nicely preserved (**Figure 5-3a, b**).

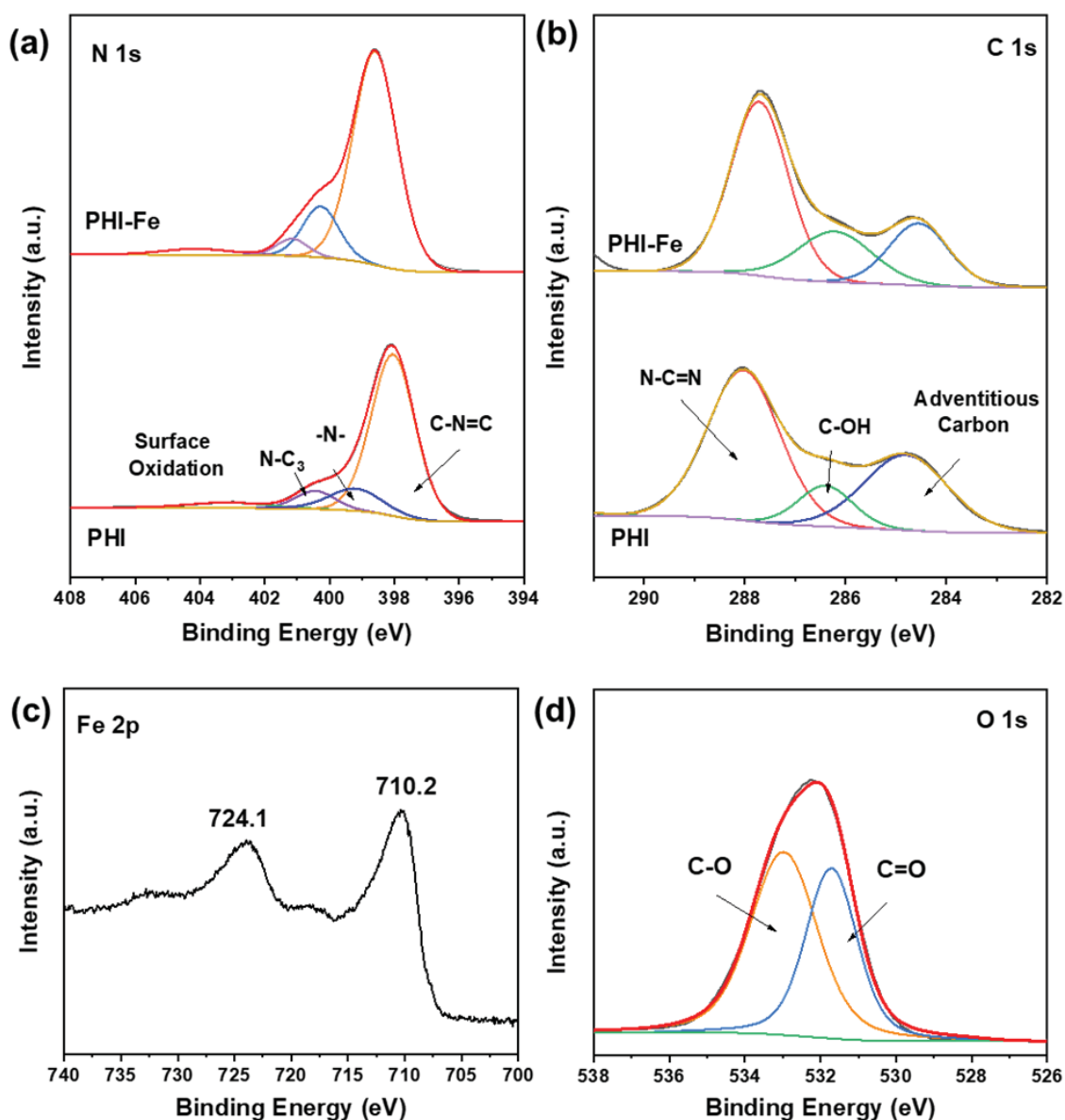


Figure 5-3 (a) N 1s (b) C1s spectrum of PHI-Fe and PHI. (c) Fe 2p and (d) O 1s XPS spectrum of PHI-Fe.

Chapter 5. Exploration of other transition metal and noble metal exchanged poly(heptazine) imides

The Fe content in PHI-Fe can be estimated from the XPS measurements. On the surface of PHI-Fe 0.8 wt% of Fe is detected. The duplet peak in the Fe 2p spectrum of PHI-Fe at 709.7 eV with broad satellite feature indicates the cations in PHI-Fe are presented in Fe(II) oxidation state (**Figure 5-3c**)²¹⁷. Meanwhile, no Fe-O bond, which typically locates at 529-530 eV, can be observed in its O 1s spectrum (**Figure 5-3d**), suggesting that the Fe remains Fe²⁺ cations in the PHI structure¹⁵⁴.

The structure of PHI-Mn can be investigated by XPS measurements and shown in **Figure 5-4**. The N 1s and C 1s spectra of PHI-Mn are compared with that of PHI (**Figure 5-4a,b**). The peaks at 398.6 eV and 400.7 eV in the N 1s spectrum, corresponding to the C-N=C (ring N in heptazine unit), N-C₃ (central N in heptazine unit), and the peak at 287.9 eV, which can be assigned to N₂-C=N in the heptazine unit, can all be found in PHI-Mn. The major peak at 284.8 eV in C 1s corresponds to adventitious carbon¹⁵⁵. This signal is originated from the samples exposed to open air, therefore, the remarkable enhancement of this signal does not correlate to any structural change of the sample²¹⁸.

The existence of Mn in the PHI structure can be confirmed by the Mn 2p spectrum (**Figure 5-4c**). A 0.5 wt% Mn content is detected on the surface of the PHI-Mn. In **Figure 5-4c**, a doublet peak centered at 541.2 eV can be spotted, which can usually be assigned to Mn²⁺. Additionally, no signal of Mn-O can be found in its O 1s spectrum (**Figure 5-4d**), indicating that most Mn cations intercalated in PHI-Mn as Mn²⁺^[130].

To sum up, a selection of the first-row transition metals are introduced into the PHI structure via adding the corresponding metal salts in the salt template. Except for Cu which was reduced to Cu(I) in the PHI structure, Mn and Fe remains Mn(II) and Fe(II) as in the metal salt. No trace of metal oxides was found in any of the mentioned PHI-M's.

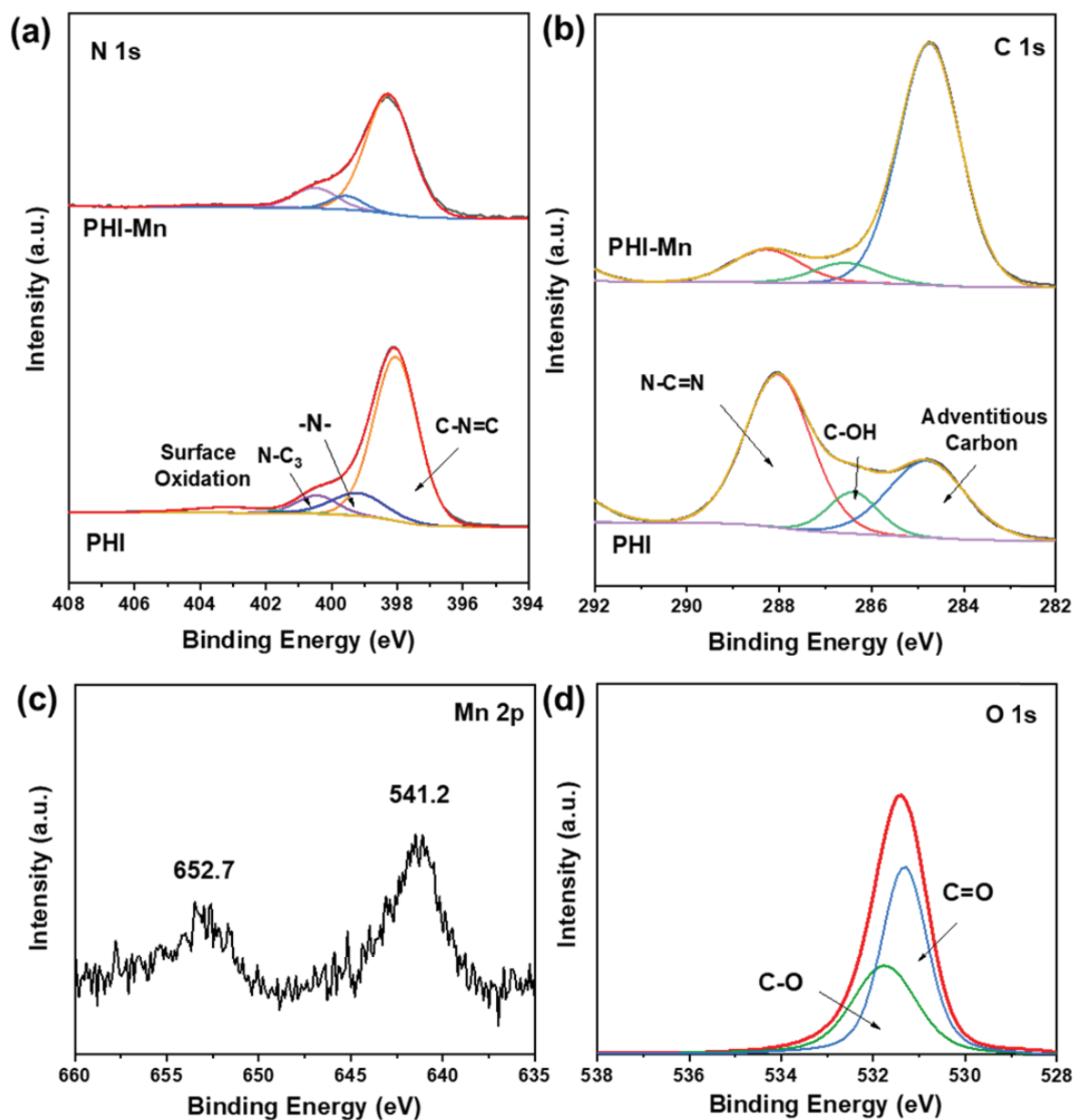


Figure 5-4 (a) N 1s (b) C1s XPS spectrum of PHI-Mn and PHI (c) Mn 2p (d) O 1s XPS spectrum of PHI-Mn.

Synthesis and structure of Pt exchanged poly(heptazine) imides.

To further explore the photocatalytic potential of PHI-based catalysts and inspired by the highly efficient metallic Pt in catalysis^[7], the Pt cations were attempted to be introduced into the PHI

Chapter 5. Exploration of other transition metal and noble metal exchanged ploy(heptazine) imides

backbone. The synthesis of PHI-Pt is very similar to the preparation of transition metal PHI-M's as described before. $K_2Pt(II)Cl_4$ (0.1 wt%) as Pt source was added to the eutectic KCl-LiCl mixture to prepare the salt template. The salt template is heated up with the 5-Aminotetrazole precursor to $550^\circ C$ for 6 hours in argon flow to yield dark brown PHI-Pt powders. The detailed synthetic process can be found in **Chapter 7 Experimental section**.

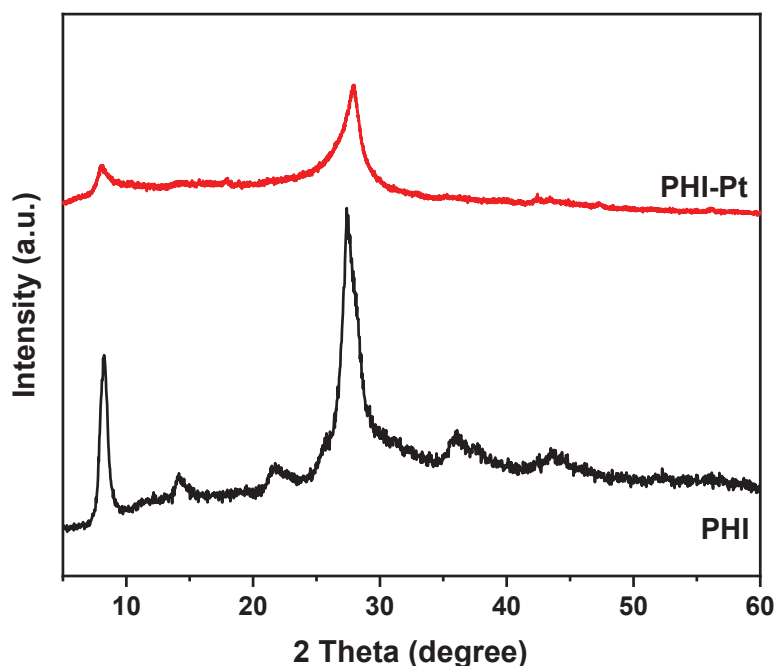


Figure 5-5 PHI-Pt's crystallinity comparing with platinum-free PHI.

The crystallinity of the as-obtained PHI-Pt is examined by its XRD patterns (**Figure 5-5**). Despite a reduced crystallinity, both the layer stacking peak at 27.0° and periodicity of heptazine ring at 8.3° can be easily observed, indicating the backbone of PHI remains after the intercalation of Pt cations¹⁵². In the XRD patterns of PHI-Pt, the diffraction peak corresponding to the layer stacking shifted to 27.6° , indicating that the layer distance is slightly increased. This might be due to the relatively large atom size of Pt, therefore, the intercalating of Pt might influence the layer stacking of PHI-Pt.

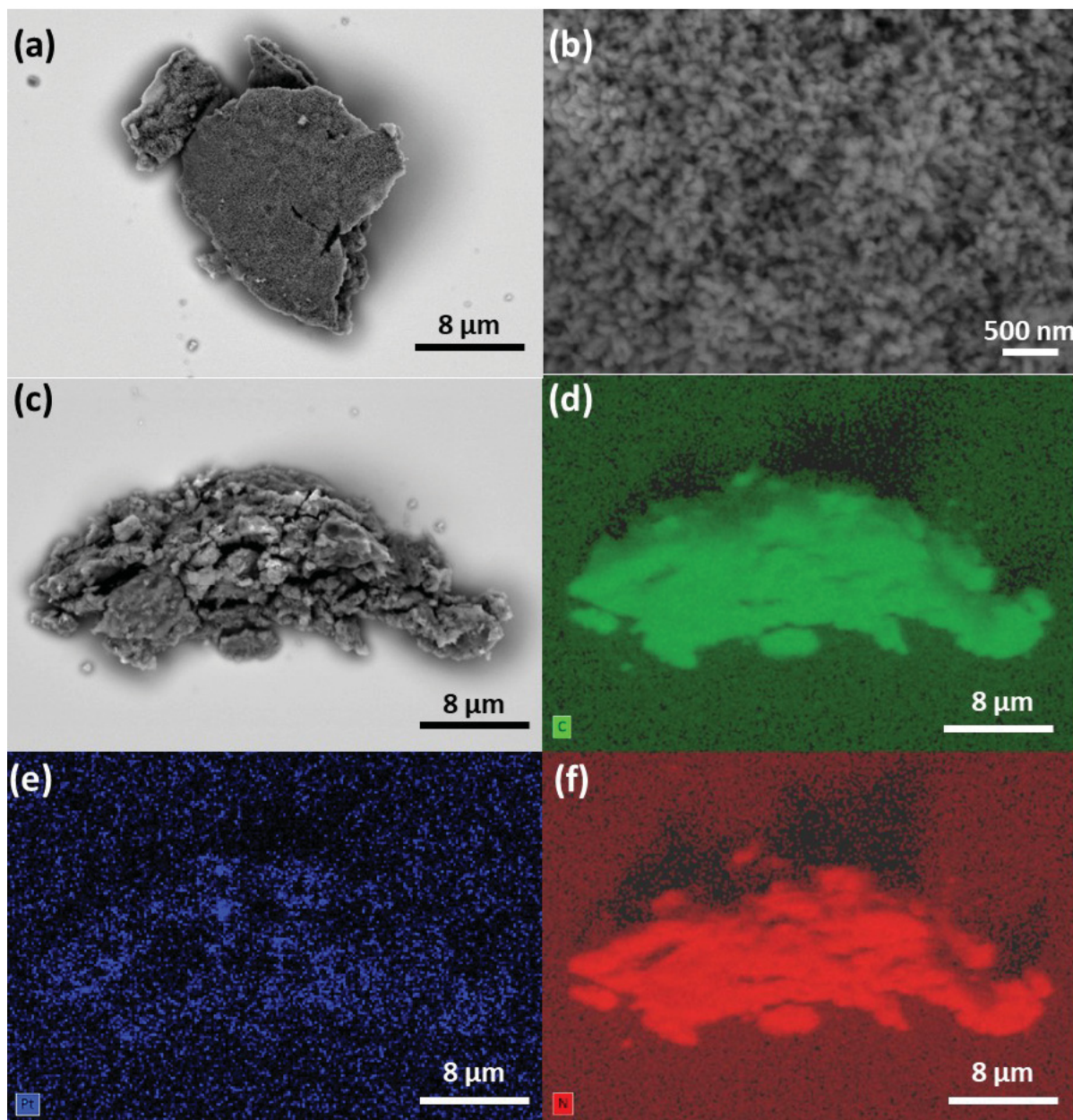


Figure 5-6 (a,b) typical morphology of PHI-Pt in magnifications of 3k and 10 k, respectively. The images were taken with the back-scatter detector. (c) PHI-Pt in magnification of 5k. (d-f) C, Pt, N EDX elemental mapping of **Figure 5-6c** area.

The morphology of PHI-Pt was investigated via SEM images collected by a backscatter electron detector, and the distribution of Pt cations is presented by EDX (energy-dispersive X-ray spectroscopy) elemental mapping coupled with the microscope (**Figure 5-6**). It can be observed that the coral-like morphology of PHI-Pt still looks similar to the typical morphology of PHI.

Chapter 5. Exploration of other transition metal and noble metal exchanged poly(heptazine) imides

The backscattered mode image presents uniform brightness without significantly bright metal agglomerations being spotted. Due to the rather low loading amount of Pt (0.3 wt%), the EDX elemental mapping shows very low contrast.

The chemical states of the elements in PHI-Pt were studied via its XPS spectra (**Figure 5-7**). As observed in **Figure 5-7a,b**, the N 1s and C 1s spectra of PHI-Pt show the same N and C species as those in N 1s and C 1s spectrum of PHI, indicating that after the intercalation of Pt cations, the PHI backbones remains unchanged.

The doublet peak in the Pt 4f spectrum (**Figure 5-7c**) of PHI-Pt at 72.9 eV reveals the oxidation state of Pt is Pt^{2+} , which is the same as in the K_2PtCl_4 metal source. The O 1s spectrum of PHI-Pt is also presented in **Figure 5-7d**. No trace of metal oxide can be detected, further proving that the Pt cations exist in PHI-Pt as Pt cations.

In short, Pt cations can be intercalated into the PHI structure. The Pt cations detected in the PHI structure are with an oxidation state of Pt (II), same as in the Pt salt. The Pt intercalated PHI presents a very similar structure as Pt-free PHI, just the crystallinity of PHI-Pt has slightly decreased. Meanwhile, after the intercalation of Pt, the diffraction peak corresponding to the layer stacking shifted to 27.6° , indicating that the layer distance is slightly increased.

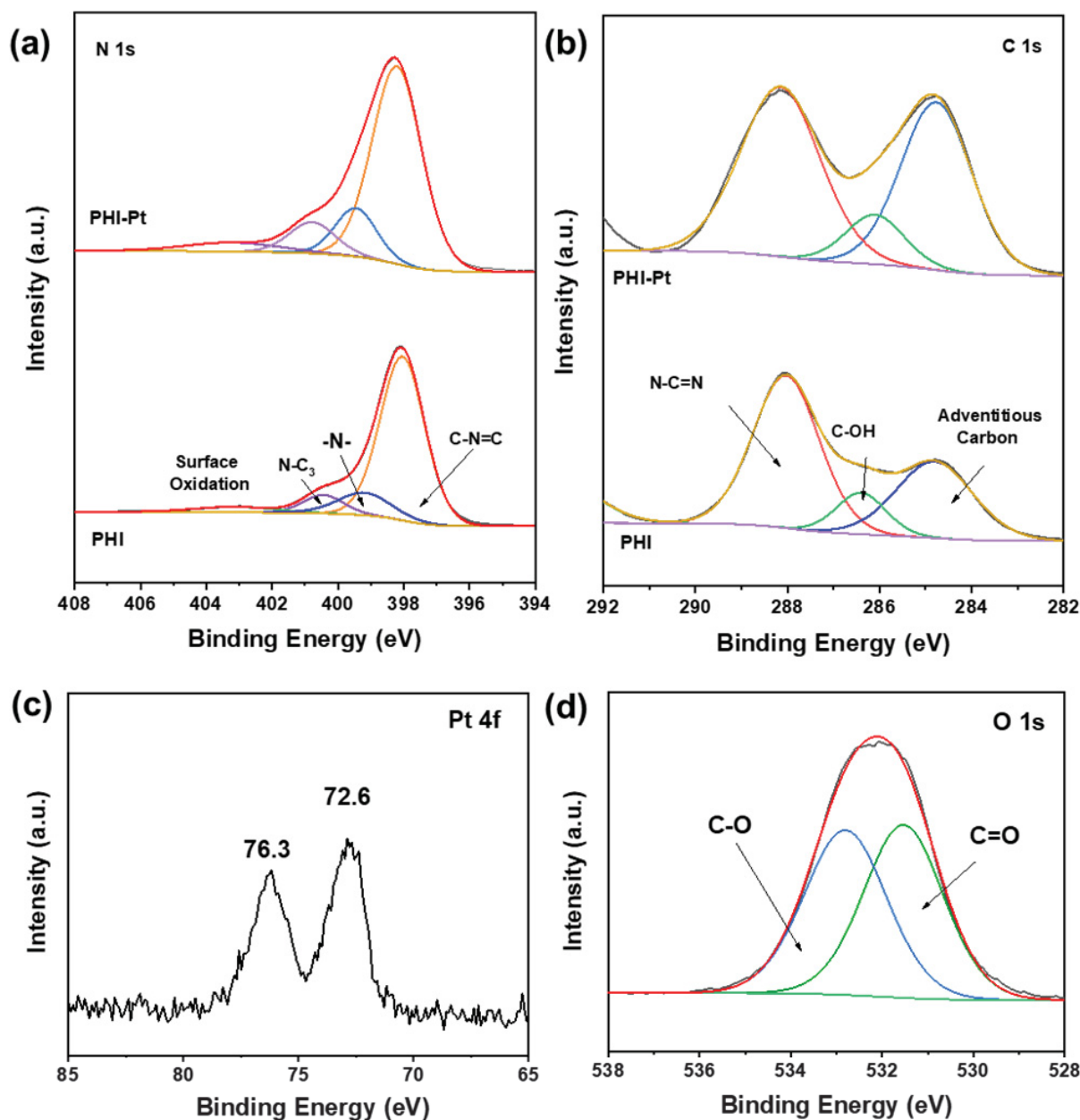


Figure 5-7 (a) N 1s (b) C 1s and (c) Pt 4f and (d) O 1s XPS spectrum of PHI-Pt.

Synthesis and structure of Co, Ni, and Co, Pt bi-metal intercalated poly(heptazine) imides

The previous chapters showed that PHI-Co is an outstanding water oxidation photocatalyst, while PHI-Ni is highly active for catalyzing hydrogen generation. Therefore, Co and Ni cations

Chapter 5. Exploration of other transition metal and noble metal exchanged ploy(heptazine) imides

were introduced into the PHI backbone simultaneously to further develop PHI-based overall water splitting photocatalysts. Meanwhile, as metallic Pt nanoparticles are the most commonly used and highly efficient co-catalyst for photocatalytic hydrogen evolution, PHI-Pt, Co were also prepared as a potential PHI-based overall water splitting photocatalyst.

The synthesis of bi-metal PHI-Co,Ni, and PHI-Co,Pt is very similar to the preparation of single metal PHI-Co, PHI-Ni, and PHI-Pt. In a typical process of preparing bi-metal PHI-Co,Ni, $\text{CoCl}_2 \cdot 6\text{H}_2\text{O}$ and $\text{NiCl}_2 \cdot 6\text{H}_2\text{O}$ were added to the eutectic KCl-LiCl salt template as Co and Ni sources, respectively. The as-obtained salt mixture was heated up with the 5-Aminotetrazole precursor to 550°C for 8 h in argon flow and eventually yield dark brown PHI-Co, Ni powders. To prepare PHI-Co,Pt, $\text{CoCl}_2 \cdot 6\text{H}_2\text{O}$ and K_2PtCl_4 were applied as Co and Pt sources, respectively. The metal source was added to the salt template, *i.e.* the eutectic KCl-LiCl mixture. The as-obtained salt template was mixed with the 5-Aminotetrazole precursor, heated up to 550°C for 8 h in argon flow, and produced reddish-brown PHI-Co, Pt powders.

The crystallinity of the as-obtained PHI-Co,Ni, and PHI-Co,Pt are examined by XRD (**Figure 5-8**). Despite a reduced crystallinity, both the layer stacking peak at 27° and the periodicity of heptazine rings at 8° can be easily observed from both of the bi-metal intercalated PHIs. A peak appears at 19.2° in the XRD pattern of PHI-Co, Pt. A small diffraction peak at a similar position can also be found for ampoule crystallized PHI in the previous report¹⁵³.

The structure of PHI-Co,Ni can be investigated by XPS measurements and the results are presented in **Figure 5-9**. The existence of both Co and Ni cations in PHI-Co,Ni can be detected from the Ni 2p and Co 2p XPS spectra (**Figure 5-9a,b**). From the XPS results, the Co and Ni contents in the PHI-Co,Ni are estimated to be 1.1 wt% and 2.3 wt%, respectively. As observed in **Figure 5-9a**, the Ni in the Ni 2p spectrum shows a doublet peak centered at 854.1 eV, corresponding well to the typical Ni(II) contribution^{156,211}. The doublet peak in **Figure 5-9b** exhibits the same shape as found in PHI-Ni. While the doublet peak in XPS Co 2p spectrum (**Figure 5-9b**) can be found at 780.4 eV with strong satellite features centered at 785.4 eV, corresponding well with the typical Co(II) oxidation state¹⁸⁵. All the N and C species in PHI-Co,Ni can be found in the typical XPS spectra PHI (**Figure 5-9c, d**). The slight shifts of the peaks are mainly due to the change of chemical environment after the Co and Ni intercalation.

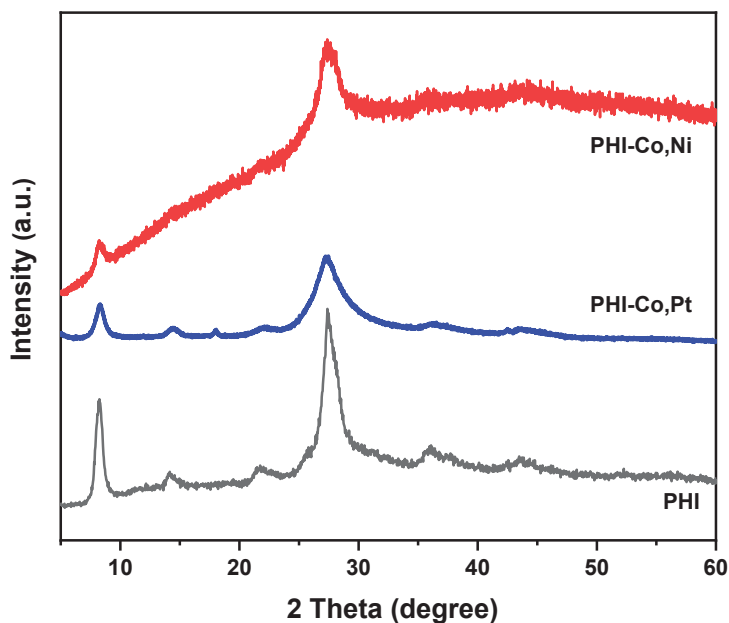


Figure 5-8 XRD patterns of PHI-Co, Ni, PHI-Co, Pt comparing with PHI.

The chemical states of elements in PHI-Co,Pt were also studied via the XPS spectra (**Figure 5-10**). The existence of both Co and Pt cations in PHI-Co,Pt can be observed from the Pt 4f and Co 2p XPS spectra, respectively (**Figure 5-10a,b**), the content of Pt and Co can be detected to be 0.9 wt% and 2.0 wt% on the surface of PHI-Co,Pt. The doublet peak in the Pt 4f spectrum (**Figure 5-10a**) of PHI-Pt at 72.8 eV reveals the oxidation state of Pt is still Pt(II). The doublet peak in the XPS Co 2p spectrum (**Figure 5-10b**) is 780.4 eV with strong satellite features centered at 785.4 eV, which is in agreement with the typical Co(II) oxidation state¹⁸⁵. The N and C species in the N 1s and C 1s spectra of PHI-Co,Pt can all be found in the corresponding N 1s and C 1s spectra of PHI (**Figure 5-10c, d**), indicating that the PHI-Co,Pt and PHI share very similar polymeric structure. However, compared to the C 1s spectrum of PHI, a rather noticeable intensity reduction of the peak 284.8 eV can be observed. This contribution is originated from the samples exposed to open air, which does not correlate to a structural change of the material²¹⁸.

Chapter 5. Exploration of other transition metal and noble metal exchanged ploy(heptazine) imides

In short, when adding two different metal sources into the salt template simultaneously, the bi-metal intercalated PHI-Co, Ni, and PHI-Co,Pt can be synthesized. Both of the metal cations can be detected via their XPS spectra while the PHI basic structure stays intact.

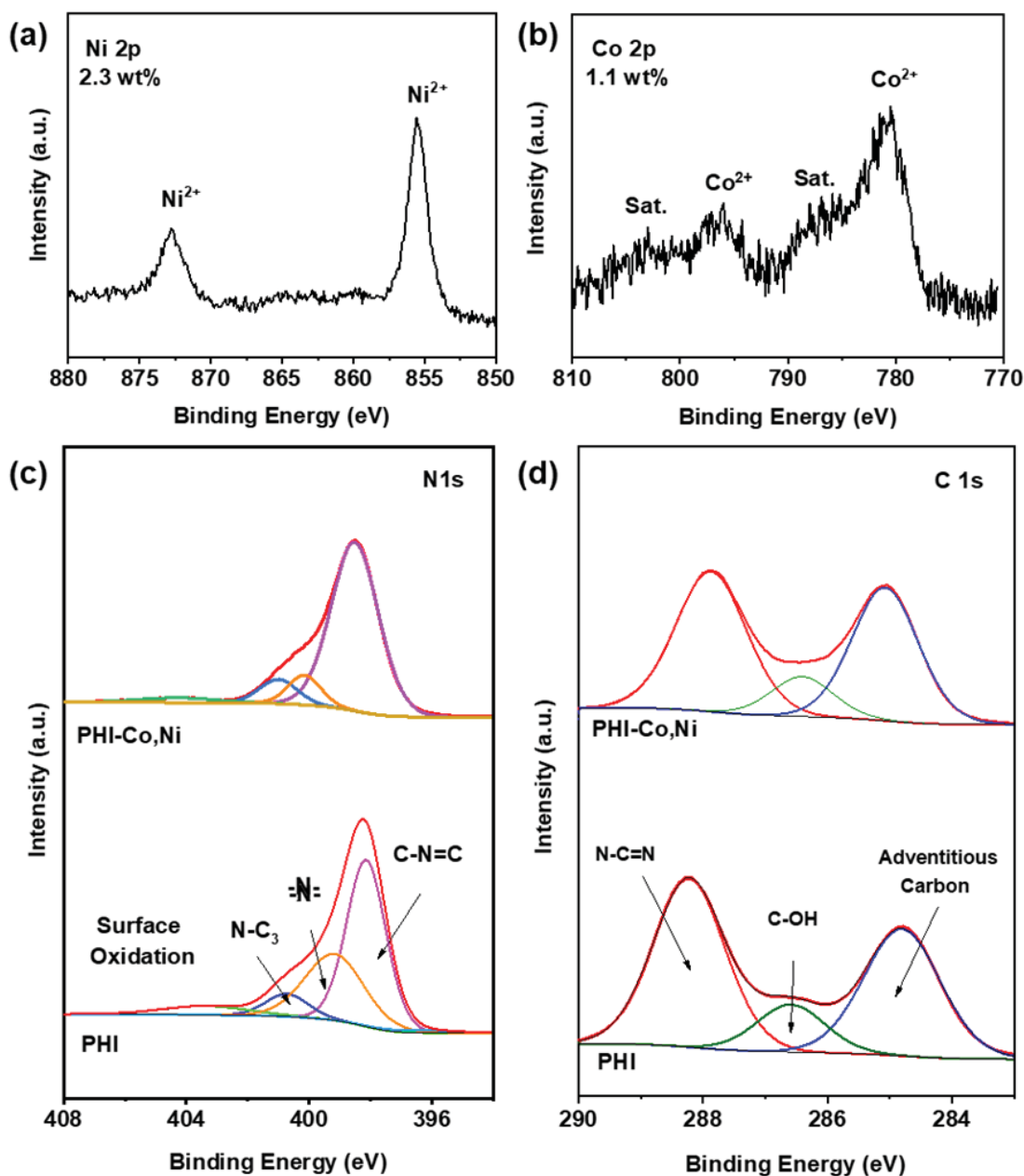


Figure 5-9 (a) Ni 2p (b) Co 2p (c) C 1s and (d) N 1s XPS spectrum of PHI-Co,Ni.

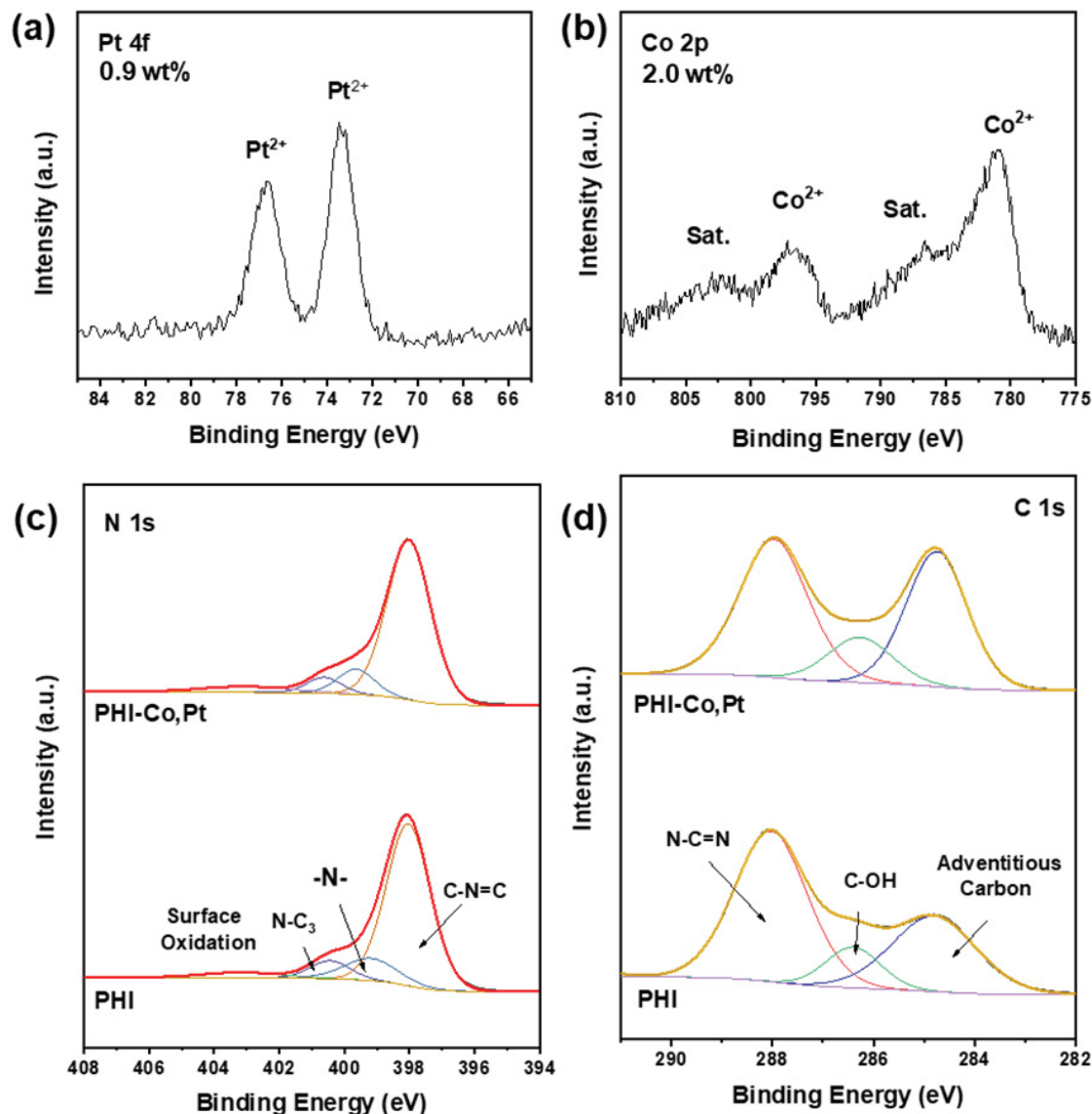


Figure 5-10 (a) Co 2p (b) Pt 4f, (c) N 1s and (d) C 1s XPS spectrum of PHI-Co,Pt.

Bandgap position tuning of PHI via the intercalating different metal cations

As observed in the previous chapters for PHI-Co and PHI-Ni, the different intercalation metal cations can lead to a bandgap width changing and band position shifting of the PHI-based photocatalysts. In this section, this phenomenon was further studied by calculating the optical

Chapter 5. Exploration of other transition metal and noble metal exchanged ploy(heptazine) imides

band positions of PHI-Pt, PHI-Co,Ni, PHI-Pt,Co, and comparing them with PHI-Co, PHI-Ni, and PHI.

The UV-vis absorption of PHI-Pt, PHI-Co,Ni, PHI-Pt,Co were measured and plotted together with PHI (**Figure 5-11a**). The intercalation of transition metal and noble metal cations has largely increased the light response region of PHI-based photocatalysts, compared with the original K intercalated PHI. The bandgap width is estimated according to the absorbance edge of these PHI-M's, and the values are listed in **Table 5-1**.

The valence band positions of PHI-Pt, PHI-Co,Ni, PHI-Pt,Co were investigated via their XPS VBM spectra (**Figure 5-11b**) and summarized in **Table 5-1**. When bandgap energy (E_g) and valence band maximum (E_{vb}) are both known, the position of the conduction band minimum (E_{cb}) can be calculated via the following equivalent:

$$E_g = E_{cb} - E_{vb} \quad (5-1)$$

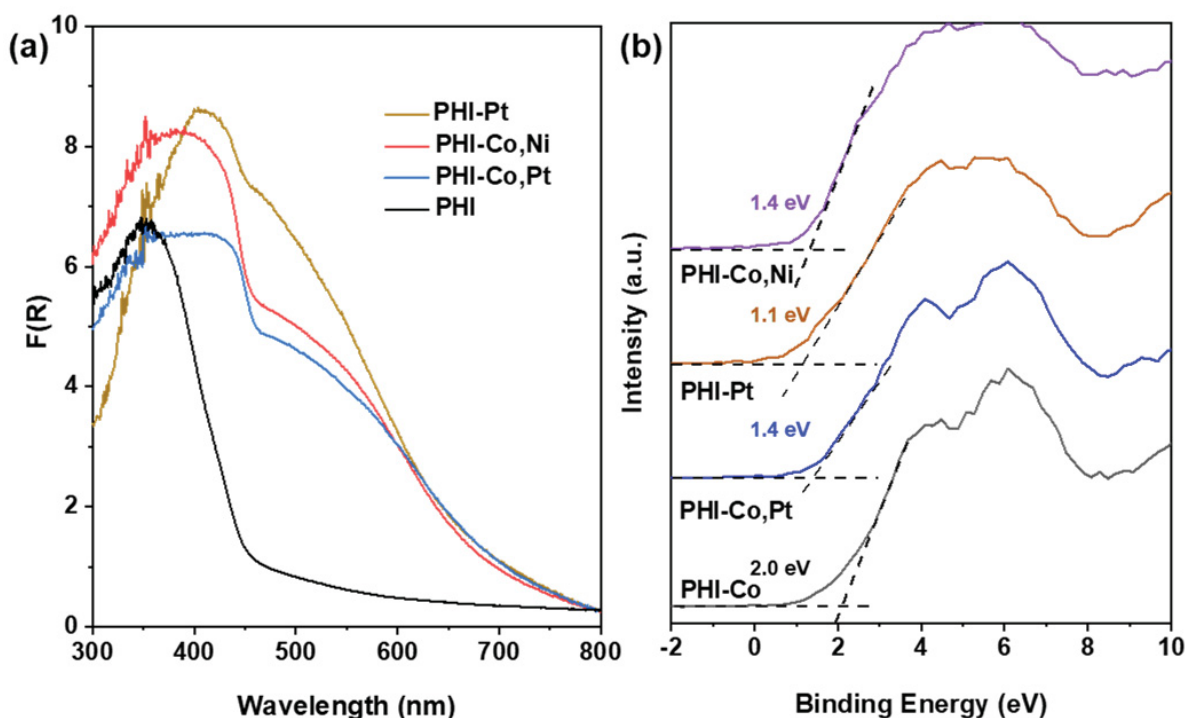


Figure 5-11 (a) UV-vis absorption spectra of PHI-Pt, PHI-Co,Ni, PHI-Pt,Co plotted with PHI. (b) VBM XPS spectrum of PHI-Pt, PHI-Co,Ni, PHI-Pt,Co.

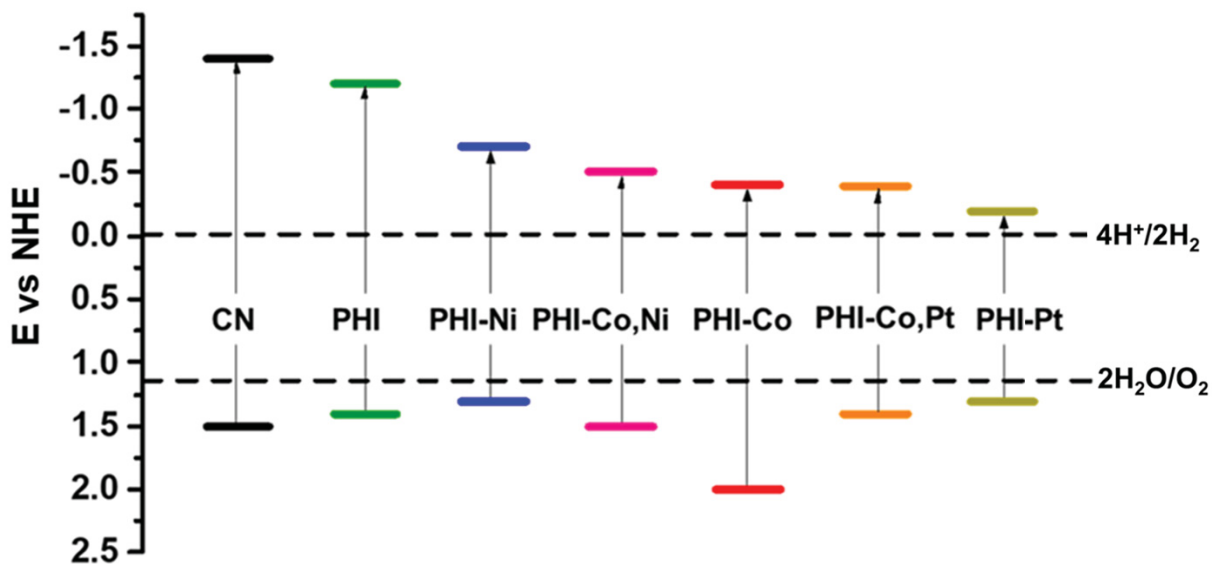
Chapter 5. Exploration of other transition metal and noble metal exchanged poly(heptazine) imides

The band positions of PHI-Pt, PHI-Co, Ni, PHI-Pt,Co are calculated as described above and schematically plotted together with CN, PHI, PHI-Co, and PHI-Ni in **Scheme 5-2**. The corresponding values of the optical bandgap width (E_g), valence band maximum (E_{vb}), and conduction band minimum (E_{cb}) are summarized in **Table 5-1**. Intercalating different cations in the PHI backbone can indeed tune the bandgap width and band position of the PHI-based materials.

First of all, the intercalation of different transition-metal- and noble-metal- cations lead to narrower optical bandgap of PHI-M's, compared to PHI. Additionally, the band positions of PHI-M's can be tuned by intercalating different metal cations. More specifically, with the intercalation of Co, the valence band maximum of PHI-Co shifts to a more significantly positive position, which is suitable for photocatalytic water oxidation. The intercalation of Ni in PHI-Ni also leads to a much narrower bandgap. At the same time, the conduction band minimum remains in a position that can provide enough driving force for photocatalytic hydrogen generation.

When Co and Ni were intercalated simultaneously, the PHI-Co,Ni shows a band position influenced by both Co and Ni. Compared to PHI-Ni, PHI-Co,Ni's band structure shifted to a more positive position; compared to PHI-Co, PHI-Co,Ni has a much narrower bandgap width, and less positive valence band position. The same trend can be observed in bi-metal PHI-Co,Pt. The intercalation of Pt cation results in a very narrow bandgap width of PHI-Pt, while when Co and Pt were intercalated together, the bandgap is broadened.

Chapter 5. Exploration of other transition metal and noble metal exchanged ploy(heptazine) imides



Scheme 5-2 The band positions of PHI-Pt, PHI-Co,Ni, PHI-Pt,Co, plotted with PHI-Co, PHI-Ni, PHI, and CN.

Table 5-1. Bandgap widths and band positions of PHI-Pt, PHI-Co, Pt, and PHI-Co, Ni.

Photocatalysts	Co Content (wt%)	Ni Content (wt%)	Bandgap Width (eV)	Valence band edge	Conduction band edge
PHI	-	-	2.7	1.5	-1.2
PHI-Ni	-	0.7	2.0	1.3	-0.7
PHI-Co,Ni	1.1	2.3	2.1	1.5	-0.6
PHI-Co	0.1	-	2.7	2.1	-0.6
PHI-Co,Pt	2.0	0.9	1.9	1.4	-0.5
PHI-Pt	-	0.3	1.4	1.1	-0.3

Conclusions

In this chapter, transition-metal- and noble-metal-intercalated PHI was successfully synthesized via the salt melting method. By varying the composition of the salt template, the intercalated metal cations in the PHI structure can be modified. The existence of the introduced metal cations can be detected by XPS. The metals stay in PHI-M's as metal ions instead of forming metal oxides.

Intercalating different metal cations can tune the band positions of PHI-M's. When two different metal cations were introduced in the PHI backbone, the band structure of the bi-metal PHI-M shows the influence of both cations.

Unfortunately, due to the very limited time, the PHI-M's presented in this chapter were not yet tested for any catalytic reactions. Therefore, applying the PHI-M's to various catalytic reactions, such as water splitting, CO₂ reduction, dry reforming of methane, *etc.*, will be important topics for further research on PHIs.

6 Conclusions and Outlook

In this thesis, a facile, salt-melt-assisted method was developed to synthesize various transition-metal-, and noble-metal-intercalated poly(heptazine) imide. Via this method, the types and amounts of metal cations in the PHI backbone can be modified by changing the composition of the salt template. As observed by the STEM measurements of PHI-Co and PHI-Ni, the intercalated metal cations are dispersed homogeneously and atomically in the PHI polymeric lattice.

Among the PHI-M's, PHI-Co shows excellent electrocatalytic OER activity. The overpotential ($j = 10 \text{ mA/cm}^2$) of the most active PHI-Co-0.5 (Co content: 0.45 wt%) is 0.324 V, standing among the best polymer-based electrocatalysts under similar conditions. This excellent activity results from the intercalation of Co cations. On the one hand, the intercalated Co cations provide highly efficient metal active centers for oxygen evolution reaction. On the other hand, PHI-Co exhibits significantly enhanced charge mobility comparing with PHI and polymeric carbon nitride.

An outstanding photocatalytic water oxidation activity is also observed for PHI-Co. The most active PHI-Co-0.1 (Co content: 0.08 wt%) shows a visible-light-driven oxygen generation activity of $589 \mu\text{mol h}^{-1} \text{ g}^{-1}$. A high apparent quantum yield of 5.1% is obtained under 420 nm of monochromatic light. The photocatalytic water oxidation performance of PHI-Co can be assigned to different effects of the intercalated Co-ions. On the one hand, PHI-Co shows a more positive valence band maximum than PHI, which is favorable for water oxidation. On the other hand, the charge separation in PHI-Co is promoted under visible-light irradiation, while the charge recombination process is suppressed. This also helps to improve energy conversion efficiency.

PHI-Ni exhibits a high performance as photocatalyst for hydrogen evolution. The most active PHI-Ni-0.7 (Ni content 0.74 wt%) shows a visible-light-driven hydrogen generation activity of $1996 \mu\text{mol g}^{-1} \text{ h}^{-1}$, which is more than 14-fold higher than for Ni-free PHI and 42-fold higher than polymeric CN. This excellent activity can also be attributed to the synergetic effects

between the PHI backbone and Ni cations. The intercalation of Ni cations leads to the narrower bandgap width, increasing the light-response region of the photocatalyst. Meanwhile, the conduction band minimum of PHI-Ni remains at a position favorable for hydrogen evolution. Better charge separation is also observed in PHI-Ni, which can be attributed to the intercalation of Ni cations.

Nonetheless, several topics related to PHI-M's await to be studied. For instance:

- (1) As found in the previous chapters, intercalating different metal cations in the PHI lattice can tune the optical band positions of the yield PHI-M. The HOMO and LUMO calculation of PHI-Co, PHI-Ni, and PHI-K implied that the intercalation of different metal cations can influence the electron distribution in the PHI-M, which consequently changes the HOMO and LUMO position of the PHI-M. However, the reason for the band structure shift in PHI-M's has not been fully understood.

In order to understand the band structure shift in PHI-M's, on the one hand, the optical band structure of PHI-M's should be confirmed via more characterizations. For instance, AQY of PHI-M's under several different incident-light wavelengths should be measured, this characterization would help differentiate the absorbance edge of the semiconductor from the pre-absorption band that was originated from the intercalated metal.

On the other hand, the HOMO and LUMO of PHI-Co, PHI-Ni in this thesis are calculated based on a model, in which all the K cations in the PHI structure are completely exchanged by Co or Ni. However, in the best-performing PHI-Co and PHI-Ni, there are still large amounts of K cations remaining in the structure. Therefore, the simulation of HOMO and LUMO states of PHI-Co and PHI-Ni should be further refined to fit better with the experimental results.

Furthermore, the HOMO and LUMO of other PHI-M's are also waiting to be calculated, in order to reveal the changes of electron distribution originated from the intercalation of different metals.

- (2) As learned from **Chapter 2** and **Chapter 3**, PHI-Co and PHI-Ni happen to be efficient catalysts for water oxidation and H₂ generation, respectively. Therefore, constructing a Z-scheme photocatalytic system with PHI-Co and PHI-Ni is promising to achieve overall

water splitting. In order to design a PHI-Co/PHI-Ni Z-scheme photocatalytic system, a suitable shuttle redox couple or conductive layer need to be chosen, and co-catalysts applied on both catalysts needs to be optimized.

- (3) Except for PHI-Co and PHI-Ni, many other transition-metal-, noble-metal- and bi-metal intercalated PHI-M's are prepared in this thesis. However, due to the limited time, their activities in catalytic reactions were not yet tested. Therefore, applying these PHI-M's to catalytic reactions such as water splitting, CO₂ reduction, dry reforming of methane, *etc.*, will be interesting for future research on PHI-M's.

To sum up, the thesis provides a facile and universal method to obtain transition-metal-, noble-metal- and bi-metal-intercalated PHI. The as-obtained PHI-Co and PHI-Ni are highly efficient electro- and photocatalysts for water splitting reaction. Due to the unique structure, PHI exhibits the potential to serve as the substrate material for designing highly efficient single-site catalysts in a variety of reactions.

7 Experimental Section

7.1 Catalysts synthesis

Chemicals

5-aminotetrazole (97%, Sigma Aldrich), $\text{CoCl}_2 \cdot 6\text{H}_2\text{O}$ (98%, Abcr), $\text{NiCl}_2 \cdot 6\text{H}_2\text{O}$ (99.95%, Alfa Aesar), CuCl_2 (97%, Aldrich), $\text{MnCl}_2 \cdot 4\text{H}_2\text{O}$ (98+%, Sigma-Aldrich), $\text{FeCl}_2 \cdot 4\text{H}_2\text{O}$ (99+%, Acros), K_2PtCl_4 (99%, Alfa Aesar), KCl (analytical grade, Merck), LiCl (99%, extra pure, Acros Organics), cyanamide (99%, Sigma Aldrich), Ir/C (20 wt%, FuelCellStore), KSCN (98.5% Alfa Aesar), KOH (98%, Sigma Aldrich), $\text{Co}(\text{NO}_3)_2$ (99.9%, Abcr), AgNO_3 (99.9%, Abcr), La_2O_3 (analytical grade, Sigma), K_2PtCl_4 (8wt% in H_2O), triethanolamine (TEOA, 99%, Roth). All the reagents were used as received.

Preparation of transition-metal-free PHI

The preparation of PHI was based on the former report^[27]. In a typical process, 5-aminotetrazole was mixed and ground with KCl and LiCl in a glove box. The weight ratio of 5-aminotetrazole to the salt template is 1 to 5. The weight ratio of KCl to LiCl is determined by their eutectic composition. The mixture was then transferred into a porcelain crucible and covered with lids. The covered crucible was placed in an argon oven and calcined under atmospheric pressure at 550 °C for 8 h with a ramp rate of 2.3°/min. Another sample with a longer calcination time, 10h, was also prepared as the reference for PHI-Ni in chapter 4. The obtained products were washed with deionized water (500 mL) for 24 h to remove the salt templates, vacuum filtered, washed extensively with deionized water, and dried at 100°C for 2 h.

Preparation of PHI-Co

Chapter 7. Experimental Section

The preparation of PHI-Co follows the same synthetic process as PHI, except for a slight change of salt template: 0.5-5 wt% of $\text{CoCl}_2 \cdot 6\text{H}_2\text{O}$ were added to the eutectic KCl-LiCl salt template, respectively, to prepare cobalt poly(heptazine) imide with different cobalt content. The weight ratio of 5-aminotetrazole to salt template kept 1 to 5. The mixture was calcined under argon flow for 6h at 550°C . The following steps stayed the same as described for preparing PHI.

Preparation of PHI-Ni

The preparation of PHI-Ni follows a very similar process as the PHI-Co mentioned above. Instead of the cobalt source $\text{CoCl}_2 \cdot 6\text{H}_2\text{O}$, nickel source $\text{NiCl}_2 \cdot 6\text{H}_2\text{O}$ was introduced to the eutectic KCl-LiCl salt template. 0.2-1.5 wt% of $\text{NiCl}_2 \cdot 6\text{H}_2\text{O}$ were added to the salt template to prepare nickel poly(heptazine) imide with different nickel content. The precursor 5-aminotetrazole was mixed with the salt template with a weight ratio of 1 to 5. The mixture was sintered under argon flow in a Muffle furnace for 10h, to gain good crystallinity, and the washing process stayed the same with PHI and PHI-Co.

Preparation of PHI-Cu

The synthesis of PHI-Cu is very similar to that of PHI-Co and PHI-Ni. More specifically, 1 wt% of CuCl_2 as Cu source was introduced to the eutectic KCl-LiCl mixture to prepare the salt template. The precursor 5-aminotetrazole were mixed with the salt template with a weight ratio of 1:5 (precursor to the salt template) in a glove box, and then transferred into a porcelain crucible and covered with lids. The crucible was placed in an argon oven and calcined under atmospheric pressure at 550°C for 8 h with a ramp rate of $2.3^\circ/\text{min}$. The obtained solid was washed with deionized water (500 mL) for 24 h to remove the salt templates, and then vacuum filtered, washed extensively with deionized water, and dried at 100°C for 2 h.

Preparation of PHI-Mn

PHI-Mn's preparation follows a similar synthetic process as PHI-Cu above: 1 wt% of $\text{MnCl}_2 \cdot 4\text{H}_2\text{O}$ were employed as Mn source and added to the eutectic KCl-LiCl salt template. The salt template was mixed and ground with the precursor 5-aminotetrazole in the glove box, the calcination and washing process stayed the same as with PHI-Cu.

Preparation of PHI-Fe

1 wt% of $\text{FeCl}_2 \cdot 4\text{H}_2\text{O}$ as Fe source was added to the eutectic KCl-LiCl salt mixture, to prepare the salt template for PHI-Fe synthesis. Other than the salt template adjustment, the other synthesis steps, such as mixing the salt template and the precursor, the calcination, and removal of the salt template, were kept the same as the synthesis of PHI-Cu.

Preparation of PHI-Pt

In general, PHI-Pt's synthetic procedure is very similar to that of the aforementioned first-row transition metal intercalated PHIs, except for the Pt source applied was K_2PtCl_4 . 0.5 wt% K_2PtCl_4 were added into the eutectic KCl-LiCl to prepare the salt template. The rest of the synthesis steps remain the same as in the synthesis of PHI-Cu.

Preparation of PHI-Co, Ni

0.5 wt% $\text{CoCl}_2 \cdot 6\text{H}_2\text{O}$ and 0.6 wt% $\text{NiCl}_2 \cdot 6\text{H}_2\text{O}$, as Co and Ni sources, were mixed with the eutectic KCl-LiCl to prepare the salt template. The salt template was then mixed with the precursor 5-aminotetrazole in the glove box with the weight ratio of salt template to precursor 5 to 1. The mixture was transferred into a crucible covered by a lid and calcined under atmospheric pressure in argon flow at 550 °C for 8 h with the ramp rate of 2.3°/min. The salt template was then washed out from the samples with deionized water (500 mL) for 24 h. The

Chapter 7. Experimental Section

obtained samples were vacuum filtered, washed extensively with deionized water, and dried at 100°C for 2 h.

Preparation of PHI-Pt, Co

The preparation of PHI-Pt, Co highly resembles the synthetic process of PHI-Co, Ni. 0.5 wt% $\text{CoCl}_2 \cdot 6\text{H}_2\text{O}$ and 0.5 wt% K_2PtCl_4 , as Co and Pt sources, were mixed with the eutectic KCl-LiCl to prepare the salt template. The salt template was then mixed with the precursor and calcined under argon flow with the same procedure and parameter applied to synthesize PHI-Co, Ni. The salt template was removed from the PHI-Pt, Co by wash and filtration in the preparation of PHI-Co, Ni.

Preparation of polymeric CN

Carbon nitride was obtained by calcining 3 g cyanamide in an argon oven under atmospheric pressure at 550°C for 8 h with the ramp rate of 2.3°/min. The obtained products were then removed from the crucible and ground into a fine powder.

Preparation of CN-Co

Cobalt-doped carbon nitride was prepared via a wet impregnation method. 1 g of carbon nitride was loaded by incipient wetness impregnation with a solution of cobalt nitrate in water, resulting in the solids with loading of 0.52 wt% and 0.12 wt% of Co, respectively. The solid was dried in vacuum and transferred to an oven. The calcination was done at 400°C with a heating rate of 3.12°C min⁻¹ under an argon flow of 3.5 mL/min for 2 hours, to yield yellow CN-Co powder.

7.2 Structural characterizations

X-ray powder diffraction (XRD) XRD patterns for the samples were measured on a Bruker D8 Advance instrument with Cu K α radiation ($\lambda=1.54 \text{ \AA}$) at a generator voltage of 40 kV and a generator current of 50 mA with a scanning speed of 1 $^{\circ}$ /min from 5 $^{\circ}$ to 60 $^{\circ}$.

X-ray photoelectron spectroscopy (XPS) XPS spectra were obtained via Thermo Fisher Scientific ESCALAB 250Xi, with the spot size 400 μm . The valence band maximum (VBM) spectra were measured in -2 eV to 10 eV.

Scanning electron microscopy (SEM) and energy-dispersive X-ray spectroscopy (EDX) The typical SEM images were collected on Gemini SEM 500 low vacuum high-resolution SEM, with a high voltage of 8 kV and in-lens detector and backscattered detector. The EDX elemental mapping was detected by the EDX detector coupled with SEM, collected at the working distance of 8 nm, with a high voltage of 20 kV.

Inductively coupled plasma optical emission spectrometry (ICP-OES) The cobalt and potassium content of PHI-Co's were measured by Varian ICP-OES 715 ES Agilent elemental wavelengths for cobalt is 228.615 nm and potassium 766.491 nm.

Nuclear Magnetic Resonance (NMR) spectroscopy The NMR experiments were performed on a Bruker Avance III wide-bore spectrometer operating at a static magnetic field of 9.4 T, with ^1H Larmor frequency of 400 MHz. The spectrometer was equipped with 3.2 mm (^1H - ^{13}C - ^{15}N) triple resonance probe heads, with the magic angle spinning (MAS) rate set to 15000 Hz. The experiments were carried out at room temperature without cooling. After calibration to account for frictional heating, the sample temperature is expected to be no more than 300K. Experiments were conducted with ^1H 90 $^{\circ}$ pulse length 2.5 μs , ^{13}C 90 $^{\circ}$ pulse length 3.9 μs , 75 kHz ^1H decoupling. 2000 μs ^1H - ^{13}C contact pulse was used for cross-polarization (CP) experiments.

Chapter 7. Experimental Section

A Gaussian-window function was employed with zero-filling (8192 points). Eventually, the spectrum was complex Fourier transformed, and the real spectrum was utilized.

Infrared spectroscopy (IR) The IR spectra of the catalysts were measured on a Nicolet iS50 FT-IR-spectrometer in ATR mode with 64 scans and a resolution of 2 cm^{-1} .

Electron paramagnetic resonance (EPR). Electron paramagnetic resonance (EPR) spectra were measured on a BrukerEMXnanoX-band device operating at an excitation frequency of ~ 9.3 GHz and 100mW microwave power.

Scanning transmission electron microscopy (STEM) For STEM observations, a suspension of the sample in ethanol was sonicated for 15 minutes and then drop-casted to the Cu grid with lacey carbon support and dried for 5 minutes. The STEM study was performed using a double Cs corrected JEOL JEM-ARM200F (S)TEM operated at 80kV and equipped with a cold-field emission gun and high-angle silicon drift Energy Dispersive X-ray (EDX) detector (solid angle up to 0.98 steradians with a detection area of 100 mm^2). Annular Dark Field Scanning Transmission Electron Microscopy (ADF-STEM) images were collected at a probe convergence semi-angle of 25mrad. The so-called "beam shower procedure was performed with a defocused beam at a magnification of $8,000\times$ for 30 min; it was necessary for reducing hydrocarbon contamination during subsequent imaging at high magnification.

X-ray absorption near edge structure (XANES) The XANES measurements of the Co K edge at 7709 eV were carried out with a self-developed wavelength-dispersive spectrometer in von Hámos geometry ^[2]. The spectrometer is equipped with a microfocus 30 W Mo X-ray tube, a curved Highly Annealed Pyrolytic Graphite mosaic crystal with a bending radius of 300 mm and a thickness of $20\text{ }\mu\text{m}$, and a hybrid photon counting CMOS detector of the type EIGER R 500K by Dectris with 512×1030 pixel and a pixel size of $75\text{ }\mu\text{m} \times 75\text{ }\mu\text{m}$. The tube was operated with a high voltage of 14.8 kV and a current of $1905\text{ }\mu\text{A}$. The references Co, CoO,

and CoCl_2 were prepared on adhesive tape by applying the material in powder form. The References Co_3O_4 were mixed with the binding material Hoechst wax C micropowder and pressed into pellets with 12 mm diameter by applying a force of 5 ton with a hydraulic pellets press. The samples PHI-Co and CN-Co were prepared with the hydraulic pellet press with a diameter of 12 mm but without the use of Hoechst wax C micropowder. The measurement times vary, depending on Co concentration and thickness of the prepared sample, between 10 h and 12.5 h, while the measurement time of the sample PHI-Co-0.2 with 0.2 wt. % Co was 15 h. For further analysis, the spectra were normalized by using ATHENA of the Demeter software package.

7.3 Activity evaluation

Electrochemical performances

Three-electrodes cell and electrodes. Electrochemical performances of the samples were measured in a three-electrode cell connecting with Gamry Reference 600 Potentiostat at room temperature. A rotating disk electrode (RDE) with a glassy carbon disk (5.0 mm diameter), a graphite rod, and Ag/AgCl (4.0 M KCl) electrode served as working, counter, and reference electrodes, respectively. All measured potentials were converted to a reversible hydrogen electrode (RHE) according to the following equation:

$$E_{\text{RHE}} = E_{\text{Ag/AgCl}} + 1.010. \quad (8-1)$$

The catalyst ink applied in measurement was obtained by mixing 10 mg of each catalyst with 1.0 ml Nafion ethanol solution (0.5 wt%) under 48 h stirring.

The working electrode was prepared by pipetting 10 μL of catalyst ink (10 mg/mL) onto the glassy carbon disk of RDE to form a catalyst film with a mass loading of 0.5 mg/cm².

The oxygen evolution reaction (OER) activity. First of all, the OER polarization curves were measured in N_2 -saturated 1.0 M KOH electrolyte between 0.0 V and 0.5 V (vs RHE) with a sweep rate of 5 mV/s with RDE rotating speed of 1600 r.p.m, measured with the LSV program.

Chapter 7. Experimental Section

The IR-drop correction during the measurement was done automatically by an electrochemical working station, with an $R = 5.8 \Omega$ as the resistance of electrolyte; the IR-drop was compensated in-time by the Gamry software. The Tafel slope was extracted from the polarization curve by setting X-axis as $\text{Log } i$ (where i stands for current density) and Y-axis as overpotential. The first linear-like part of these converted curves was drawn as Tafel plots, usually a 0.1 V region including the onset potential.

Electrochemical impedance spectroscopy (EIS) for OER was carried out in N_2 -saturated 1.0 M KOH electrolyte from 10 kHz to 0.1 Hz with a 5 mV AC potential with RDE rotating speed of 1600 r.p.m. PHI-Co's stability was tested by chronoamperometry at a constant applied current of 2 mA (c.a. current density approx. 10 mA/cm^2).

Photocatalytic water oxidation activity The photocatalytic water oxidation half-reactions were carried out in a gas-closed circulation system. For each test, 20 mg catalyst was dispersed in 100 mL deionized water with 108.72 mg sacrificial agent AgNO_3 and 32 mg buffer La_2O_3 (pH=8.5) in a Pyrex cell with a side window. The reaction was run under the illumination of a 300 W of Xe arc lamp with a visible-light ($\lambda > 420 \text{ nm}$) filter. The generated oxygen was measured by an on-line gas chromatograph (GC-8A, Shimadzu) with a thermal conductivity detector (TCD) according to the standard curve.

Photocatalytic hydrogen evolution activity The photocatalytic hydrogen evolution half-reactions were carried out in a gas-closed circulation system. For each test, 10 mg catalyst was dispersed in 14 mL deionized water with 2mL sacrificial agent triethanolamine (TEOA) in a batch reactor (volume 35 mL) with a side window. The reaction was run under the illumination of a 300 W of Xe arc lamp with a visible-light ($\lambda > 420 \text{ nm}$) filter. The generated hydrogen was measured by off-line gas chromatography (GC-8A, Shimadzu) with a thermal conductivity detector (TCD) according to the standard curve.

7.4 Calculations

Turn over frequency calculation

The TOF of the samples was calculated by current density with the following equation. The obtained values were plotted against overpotential in the manuscript.

$$\text{TOF} = I/\alpha nF \quad (8-2)$$

Where I is the current density, α is 4 for OER due to the four-electron reaction, F is Faraday constant. N is the molar concentration of active sites, which was directly converted from the mol% of cobalt measured by XPS (Table S0 below). Due to the XPS measurement's surface-sensitive nature, this data should represent the cobalt amount on the surface of PHI-Co.

Band position calculation

The photocatalysts' optical bandgap (E_g) were calculated by the Tauc plot derived from UV-vis analysis. Typically, a Tauc plot shows the $h\nu$ on the abscissa, where h is Planck constant, ν is the frequency of light. The calculation of ν follows the equation below:

$$\nu = c/\lambda \quad (8-3)$$

Where c is the speed of light, λ is the wavelength from the UV-vis spectra.

On the other hand, the Tauc plot's ordinate can be written as $(\alpha h\nu)^{1/r}$, where α is absorption coefficient, which can often be substituted by $F(R)$ in the UV-vis spectrum. For direct allowed transitions, $r = 1/2$.

Usually, extrapolating the first linear region of the Tauc plot to the X-axis yields the optical bandgap's energy of the semiconductor.

The valence band maximum (VBM) spectra can be obtained through the -2~10 eV region spectra of XPS. Extrapolating the first linear region of VBM spectra and compared with semiconductor with known band structure can calculate the position of valence band maximum(E_{vb}) of the semiconductor.

When bandgap energy (E_g) and valence band maximum(E_{vb}) both known, the position of conduction band minimum (E_{cb}) can be calculated via the following equivalent:

$$E_g = E_{cb} - E_{vb} \quad (8-4)$$

HOMO and LUMO positions

The structure was simulated using Materials Studio 18, DFTB+, 3ob function. The DFT calculation is applied to PHI based on the molecular structure of PHI with potassium cations reported by Lotsch *et. al.*¹⁵³, where all the heptazine units are connected by imide bridges, and all the negative charges of PHI is fully counterbalanced by K cations, forming an imide to K cations 1:1 ratio. For the calculation of PHI-Co and PHI-Ni, the K cations are completely exchanged by Co and Ni cations, respectively. The exchange ratio was 2:1 Co/Ni to K.

Supporting Information

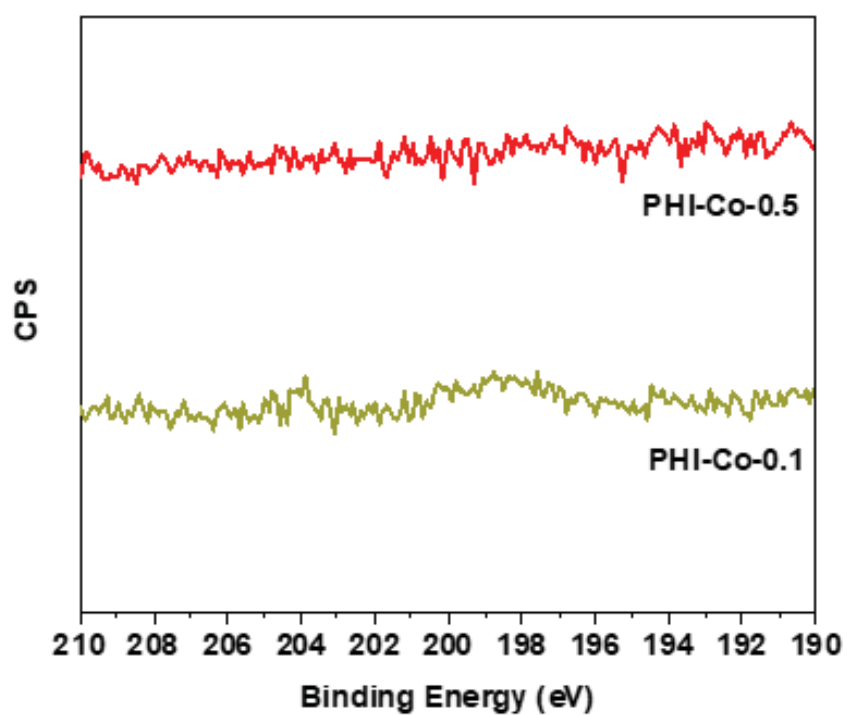


Figure S1 Cl 2p XPS spectra of PHI-Co with different Co contents.

References

1. Lewis, N. S. & Nocera, D. G. Powering the planet: Chemical challenges in solar energy utilization. *Proceedings of the National Academy of Sciences of the United States of America* (2006) 103, 43, 15729-15735.
2. Lal, R. Soil carbon sequestration impacts on global climate change and food security. *Science* (2004) 304, 5677, 1623-1627.
3. Galloway, J. N. *et al.* Transformation of the nitrogen cycle: Recent trends, questions, and potential solutions. *Science* (2008) 320, 5878, 889-892.
4. Wang, Q. *et al.* Scalable water splitting on particulate photocatalyst sheets with a solar-to-hydrogen energy conversion efficiency exceeding 1%. *Nature Materials* (2016) 15, 611–615.
5. Indra, A. *et al.* Boosting Visible-Light-Driven Photocatalytic Hydrogen Evolution with an Integrated Nickel Phosphide–Carbon Nitride System. *Angewandte Chemie - International Edition* (2017) 56, 6, 1653-1657.
6. Ye, M. Y. *et al.* 0D/2D Heterojunctions of Vanadate Quantum Dots/Graphitic Carbon Nitride Nanosheets for Enhanced Visible-Light-Driven Photocatalysis. *Angewandte Chemie - International Edition* (2017) 56, 8407–8411.
7. Maeda, K. & Domen, K. Photocatalytic water splitting: Recent progress and future challenges. *Journal of Physical Chemistry Letters* (2010) 1, 18, 2655–2661.
8. Rostrup-Nielsen, J. R., Sehested, J. & Nørskov, J. K. Hydrogen and synthesis gas by steam- and CO₂ reforming. *Advances in Catalysis* (2002) 47, 65-139.
9. Cortright, R. D., Davda, R. R. & Dumesic, J. A. Hydrogen from catalytic reforming of biomass-derived hydrocarbons in liquid water. *Nature* (2002) 418, 964–967.
10. Chen, S., Takata, T. & Domen, K. Particulate photocatalysts for overall water splitting. *Nature Reviews Materials* (2017) 2, 17050.
11. Artero, V., Chavarot-Kerlidou, M. & Fontecave, M. Splitting water with cobalt. *Angewandte Chemie - International Edition* (2011) 50, 32, 7238-7266.
12. Wang, Z., Li, C. & Domen, K. Recent developments in heterogeneous photocatalysts for solar-driven overall water splitting. *Chemical Society Reviews* (2019) 48, 2109-2125.
13. Yan, Y., Xia, B. Y., Zhao, B. & Wang, X. A review on noble-metal-free bifunctional heterogeneous catalysts for overall electrochemical water splitting. *Journal of Materials Chemistry A* (2016) 4, 17587-17603.

References

14. Zhang, G., Lan, Z. A. & Wang, X. Surface engineering of graphitic carbon nitride polymers with cocatalysts for photocatalytic overall water splitting. *Chemical Science* (2017) 8, 5261-5274.
15. Hou, J. *et al.* Electrical Behavior and Electron Transfer Modulation of Nickel–Copper Nanoalloys Confined in Nickel–Copper Nitrides Nanowires Array Encapsulated in Nitrogen-Doped Carbon Framework as Robust Bifunctional Electrocatalyst for Overall Water Splitting. *Advanced Functional Materials* (2018) 28, 37, 1803278.
16. Chen, S., Takata, T. & Domen, K. Particulate photocatalysts for overall water splitting. *Nature Reviews Materials* (2017) 2, 17050.
17. Yan, Y., Xia, B. Y., Zhao, B. & Wang, X. A review on noble-metal-free bifunctional heterogeneous catalysts for overall electrochemical water splitting. *Journal of Materials Chemistry A* (2016) 4, 17587-17603.
18. Monte-Pérez, I. *et al.* Temperature Dependence of the Catalytic Two- versus Four-Electron Reduction of Dioxygen by a Hexanuclear Cobalt Complex. *Journal of the American Chemical Society* (2017) 139, 15033–15042.
19. Pinhassi, R. I. *et al.* Hybrid bio-photo-electro-chemical cells for solar water splitting. *Nature Communications* (2016) 7, 12552.
20. Gong, H. *et al.* Pt@Cu₂O/WO₃ composite photocatalyst for enhanced photocatalytic water oxidation performance. *Applied Catalysis B: Environmental* (2018) 237, 309-317.
21. Liu, D. *et al.* Synergistic Effect of Atomically Dual-metal Doped Catalyst for Highly Efficient Oxygen Evolution. *Journal of Materials Chemistry A* 6840–6846 (2018) 6, 6840-6846.
22. Pachfule, P. *et al.* Diacetylene Functionalized Covalent Organic Framework (COF) for Photocatalytic Hydrogen Generation. *Journal of the American Chemical Society* (2018) 140, 4, 1423-1427.
23. Qiu, C. *et al.* Highly Crystalline K-Intercalated Polymeric Carbon Nitride for Visible-Light Photocatalytic Alkenes and Alkynes Deuterations. *Advanced Science* (2019) 6, 1, 1801403.
24. Cobo, S. *et al.* A Janus cobalt-based catalytic material for electro-splitting of water. *Nature Materials* (2012) 11, 802–807.
25. Wang, Qian, *et al.* Oxysulfide photocatalyst for visible-light-driven overall water splitting. *Nature materials* (2019) 18, 827-832.
26. Kim, J., Yin, X., Tsao, K. C., Fang, S. & Yang, H. Ca₂Mn₂O₅ as Oxygen-Deficient Perovskite Electrocatalyst for Oxygen Evolution Reaction. *Journal of the American Chemical Society* (2014) 32, 3439-3446.

27. Li, S., *et al.*, A. Active Salt/Silica-Templated 2D Mesoporous FeCo-Nx-Carbon as Bifunctional Oxygen Electrodes for Zinc–Air Batteries. *Angewandte Chemie - International Edition* (2018) 57, 1856-1862.
28. Ye, M. Y. *et al.* Cobalt-Exchanged Poly(Heptazine Imides) as Transition Metal–Nx Electrocatalysts for the Oxygen Evolution Reaction. *Advanced Materials* (2020) 32, 9, 1903942.
29. Xu, Y. *et al.* Ultrathin two-dimensional cobalt-organic framework nanosheets for high-performance electrocatalytic oxygen evolution. *Journal of Materials Chemistry A* (2018) 6, 22070-22076.
30. Ishikawa, A. *et al.* Oxysulfide $\text{Sm}_2\text{Ti}_2\text{S}_2\text{O}_5$ as a stable photocatalyst for water oxidation and reduction under visible light irradiation ($\lambda \leq 650$ nm). *Journal of the American Chemical Society* (2002) 124, 13547-53.
31. Chung, H. Y., *et al.* Balancing the crystallinity and specific surface area of bismuth tungstate for photocatalytic water oxidation. *Molecular Catalysis* (2020) 487, 110887.
32. Zhang, Z., *et al.* Intercalated graphitic carbon nitride: A fascinating two-dimensional nanomaterial for an ultra-sensitive humidity nanosensor. *Nanoscale* (2014) 6, 9250-9256.
33. Dontsova, D. *et al.* Triazoles: A New Class of Precursors for the Synthesis of Negatively Charged Carbon Nitride Derivatives. *Chemistry of Materials* (2015) 27, 5170–5179.
34. Maeda, K. *et al.* Photocatalytic activities of graphitic carbon nitride powder for water reduction and oxidation under visible light. *Journal of Physical Chemistry C* (2009) 113, 12, 4940–4947.
35. Tian, J. *et al.* Ultrathin graphitic carbon nitride nanosheets: A low-cost, green, and highly efficient electrocatalyst toward the reduction of hydrogen peroxide and its glucose biosensing application. *Nanoscale* (2013) 5, 8921-8924.
36. Xu, C. *et al.* Sulfur-doped graphitic carbon nitride decorated with graphene quantum dots for an efficient metal-free electrocatalyst. *Journal of Materials Chemistry A* (2015) 3, 1841-1846.
37. Tian, S. *et al.* Temperature-Controlled Selectivity of Hydrogenation and Hydrodeoxygenation in the Conversion of Biomass Molecule by the Ru1/mpg-C3N4 Catalyst. *Journal of the American Chemical Society* (2018) 140, 11161–11164.
38. Masa, J., Xia, W., Muhler, M. & Schuhmann, W. On the Role of Metals in Nitrogen-Doped Carbon Electrocatalysts for Oxygen Reduction. *Angewandte Chemie - International Edition* (2015) 54, 35, 10102-10120.
39. Tang, Y. *et al.* Cobalt and nitrogen codoped ultrathin porous carbon nanosheets as bifunctional electrocatalysts for oxygen reduction and evolution. *Carbon* (2019) 141, 704–711.

References

40. Yang, L. *et al.* Unveiling the high-activity origin of single-atom iron catalysts for oxygen reduction reaction. *Proceedings of the National Academy of Sciences* (2018) 115, 6626–6631.
41. Artyushkova, K., Serov, A., Rojas-Carbonell, S. & Atanassov, P. Chemistry of Multitudinous Active Sites for Oxygen Reduction Reaction in Transition Metal-Nitrogen-Carbon Electrocatalysts. *Journal of Physical Chemistry C* (2015) 119, 46, 25917–25928.
42. Merschjann, C. *et al.* Complementing Graphenes: 1D Interplanar Charge Transport in Polymeric Graphitic Carbon Nitrides. *Advanced Materials* (2015) 27, 48, 7993–7999.
43. Wirnhier, E. *et al.* Poly(triazine imide) with intercalation of lithium and chloride ions [(C₃N₃)₂(NH_xLi_{1-x})₃.LiCl]: A crystalline 2D carbon nitride network. *Chemistry - A European Journal* (2011) 17, 11 3213–3221.
44. Savateev, A. *et al.* Potassium Poly(heptazine imides) from Aminotetrazoles: Shifting Band Gaps of Carbon Nitride-like Materials for More Efficient Solar Hydrogen and Oxygen Evolution. *ChemCatChem* (2017) 9, 167–174.
45. Wang, X. *et al.* A metal-free polymeric photocatalyst for hydrogen production from water under visible light. *Nature Materials* (2009) 8, 76–80.
46. Jun, Y. S., Hong, W. H., Antonietti, M. & Thomas, A. Mesoporous, 2D hexagonal carbon nitride and titanium nitride/carbon composites. *Advanced Materials* (2009) 21, 42, 4270–4274.
47. Cao, S., Low, J., Yu, J. & Jaroniec, M. Polymeric Photocatalysts Based on Graphitic Carbon Nitride. *Advanced Materials* (2015) 27, 13, 2150–2176.
48. Chen, Z. *et al.* “The Easier the Better” Preparation of Efficient Photocatalysts—Metastable Poly(heptazine imide) Salts. *Advanced Materials* (2017) 29, 1–8.
49. Savateev, A., Pronkin, S., Willinger, M. G., Antonietti, M. & Dontsova, D. Towards Organic Zeolites and Inclusion Catalysts: Heptazine Imide Salts Can Exchange Metal Cations in the Solid State. *Chemistry - An Asian Journal* (2017) 12, 1517–1522.
50. Zoulias, E. & Varkaraki, E. A review on water electrolysis. *Tcjst* (2004).
51. Rossmeisl, J., Qu, Z. W., Zhu, H., Kroes, G. J. & Nørskov, J. K. Electrolysis of water on oxide surfaces. *Journal of Electroanalytical Chemistry* (2007) 607, 1–2, 83–89.
52. Robinson, H. M. Electrolysis. *Southern Medical Journal* (1947). 40, 7, 619–23.
53. Zeng, K. & Zhang, D. Recent progress in alkaline water electrolysis for hydrogen production and applications. *Progress in Energy and Combustion Science* (2010) 36, 3, 307–326.
54. Rashid, M. M., Mesfer, M. K. al, Naseem, H. & Danish, M. Hydrogen Production by Water Electrolysis: A Review of Alkaline Water Electrolysis, PEM Water Electrolysis and High Temperature Water Electrolysis. *International Journal of Engineering and Advanced Technology* (2015).

-
55. Li, X., Hao, X., Abudula, A. & Guan, G. Nanostructured catalysts for electrochemical water splitting: Current state and prospects. *Journal of Materials Chemistry A* (2016) 4, 11973-12000.
 56. Zou, X. & Zhang, Y. Noble metal-free hydrogen evolution catalysts for water splitting. *Chemical Society Reviews* (2015) 44, 5148-5180.
 57. Li, X., Hao, X., Abudula, A. & Guan, G. Nanostructured catalysts for electrochemical water splitting: Current state and prospects. *Journal of Materials Chemistry A* (2016) 4, 11973-12000.
 58. Gerken, J. B. *et al.* Electrochemical water oxidation with cobalt-based electrocatalysts from pH 0-14: The thermodynamic basis for catalyst structure, stability, and activity. *Journal of the American Chemical Society* (2011) 133, 14431-42.
 59. Bajdich, M., García-Mota, M., Vojvodic, A., Nørskov, J. K. & Bell, A. T. Theoretical investigation of the activity of cobalt oxides for the electrochemical oxidation of water. *Journal of the American Chemical Society* (2013) 135, 36, 13521-13530.
 60. Zou, X. & Zhang, Y. Noble metal-free hydrogen evolution catalysts for water splitting. *Chemical Society Reviews* (2015) 2015, 44, 5148-5180.
 61. Cheng, N. *et al.* Platinum single-atom and cluster catalysis of the hydrogen evolution reaction. *Nature Communications* (2016) 7, 13638.
 62. Zeng, M. & Li, Y. Recent advances in heterogeneous electrocatalysts for the hydrogen evolution reaction. *Journal of Materials Chemistry A* (2015) 3, 14942-14962.
 63. Eftekhari, A. Electrocatalysts for hydrogen evolution reaction. *International Journal of Hydrogen Energy* (2017) 7, 1, 19-29.
 64. Vesborg, P. C. K., Seger, B. & Chorkendorff, I. Recent development in hydrogen evolution reaction catalysts and their practical implementation. *Journal of Physical Chemistry Letters* (2015) 6, 951-957.
 65. Zheng, Y., Jiao, Y., Jaroniec, M. & Qiao, S. Z. Advancing the electrochemistry of the hydrogen- Evolution reaction through combining experiment. *Angewandte Chemie - International Edition* (2015) 127, 52-66.
 66. Greeley, J., Jaramillo, T. F., Bonde, J., Chorkendorff, I. & Nørskov, J. K. Computational high-throughput screening of electrocatalytic materials for hydrogen evolution. *Nature Materials* (2006) 5, 11, 909-913.
 67. Cheng, N. *et al.* Platinum single-atom and cluster catalysis of the hydrogen evolution reaction. *Nature Communications* (2016) 7, 1-7.
 68. Lu, Q. *et al.* Highly porous non-precious bimetallic electrocatalysts for efficient hydrogen evolution. *Nature Communications* (2015) 6, 1, 1-8.
 69. Zheng, Y. *et al.* Hydrogen evolution by a metal-free electrocatalyst. *Nature Communications* (2014) 5, 1-8.

References

70. Liu, H. *et al.* Recent Advances on Black Phosphorus for Energy Storage, Catalysis, and Sensor Applications. *Advanced Materials* (2018) 30, 25, 1800128
71. Jia, Jin, *et al.* Ultrathin N-doped Mo₂C nanosheets with exposed active sites as efficient electrocatalyst for hydrogen evolution reactions. *ACS nano* (2017) 11, 12, 12509-12518.
72. Ang, Huixiang, *et al.* 3D hierarchical porous Mo₂C for efficient hydrogen evolution. *Small* (2016) 12, 21, 2859-2865.
73. Miao, Ran, *et al.* Mesoporous iron sulfide for highly efficient electrocatalytic hydrogen evolution. *Journal of the American Chemical Society* (2017) 139, 39, 13604-13607.
74. Jing, Feng, *et al.* Highly active and dual-function self-supported multiphase NiS–NiS₂–Ni₃S₂/NF electrodes for overall water splitting. *Journal of Materials Chemistry A* (2018) 6, 29, 14207-14214.
75. Dong, Xusha, *et al.* Hard template-assisted N, P-doped multifunctional mesoporous carbon for supercapacitors and hydrogen evolution reaction. *Journal of Materials Science* (2021) 56, 3, 2385-2398.
76. Liu, Y., Jiang, H., Zhu, Y., Yang, X. & Li, C. Transition metals (Fe, Co, and Ni) encapsulated in nitrogen-doped carbon nanotubes as bi-functional catalysts for oxygen electrode reactions. *Journal of Materials Chemistry A* (2016) 4, 5, 1694-1701.
77. Tong, Y. *et al.* A Bifunctional Hybrid Electrocatalyst for Oxygen Reduction and Evolution: Cobalt Oxide Nanoparticles Strongly Coupled to B,N-Decorated Graphene. *Angewandte Chemie - International Edition* (2017) 56, 25, 7121-7125.
78. ikkarolla, S. K. & Papakonstantinou, P. CuCo₂O₄ nanoparticles on nitrogenated graphene as highly efficient oxygen evolution catalyst. *Journal of Power Sources* (2015) 281, 243-251.
79. Xu, Y., Kraft, M. & Xu, R. Metal-free carbonaceous electrocatalysts and photocatalysts for water splitting. *Chemical Society Reviews* (2016) 45, 11, 3039-3052.
80. Yan, D. *et al.* Defect Chemistry of Nonprecious-Metal Electrocatalysts for Oxygen Reactions. *Advanced Materials* (2017) 29, 48, 1606459.
81. Jiao, Y., Zheng, Y., Jaroniec, M. & Qiao, S. Z. Origin of the electrocatalytic oxygen reduction activity of graphene-based catalysts: A roadmap to achieve the best performance. *Journal of the American Chemical Society* (2014) 136, 11, 4394-4403.
82. Bockris, J. O. & Otagawa, T. The Electrocatalysis of Oxygen Evolution on Perovskites. *Journal of The Electrochemical Society* (1984) 131, 2, 290.
83. Mefford, J. T. *et al.* Water electrolysis on La_{1-x}Sr_xCoO_{3-δ} perovskite electrocatalysts. *Nature Communications* (2016) 7, 1, 1-11.
84. Gong, M. *et al.* An advanced Ni-Fe layered double hydroxide electrocatalyst for water oxidation. *Journal of the American Chemical Society* (2013) 135, 23, 8452-8455.

85. Shakeel, M., Arif, M., Yasin, G., Li, B. & Khan, H. D. Layered by layered Ni-Mn-LDH/g-C₃N₄ nanohybrid for multi-purpose photo/electrocatalysis: Morphology controlled strategy for effective charge carriers separation. *Applied Catalysis B: Environmental* (2019) 242, 485-498.
86. Suen, N. T. *et al.* Electrocatalysis for the oxygen evolution reaction: Recent development and future perspectives. *Chemical Society Reviews* (2017) 46, 2, 337-365.
87. Sun, H. *et al.* Self-Supported Transition-Metal-Based Electrocatalysts for Hydrogen and Oxygen Evolution. *Advanced Materials* (2020) 32, 3, 1806326.
88. Jamesh, M. I. & Sun, X. Recent progress on earth abundant electrocatalysts for oxygen evolution reaction (OER) in alkaline medium to achieve efficient water splitting – A review. *Journal of Power Sources* (2018) 400, 31-68.
89. Xia, B. Y. *et al.* A metal-organic framework-derived bifunctional oxygen electrocatalyst. *Nature Energy* (2016) 1, 1, 1-8.
90. McKone, J. R., Marinescu, S. C., Brunschwig, B. S., Winkler, J. R. & Gray, H. B. Earth-abundant hydrogen evolution electrocatalysts. *Chemical Science* (2014) 5, 3, 865-878.
91. Yagi, S. *et al.* Covalency-reinforced oxygen evolution reaction catalyst. *Nature Communications* (2015) 6, 1, 1-8.
92. Zhu, Y. *et al.* Enhancing Electrocatalytic Activity of Perovskite Oxides by Tuning Cation Deficiency for Oxygen Reduction and Evolution Reactions. *Chemistry of Materials* (2016) 28, 6, 1691-1697.
93. Bode, H., K. Dehmelt, and J. Witte. Zur kenntnis der nickelhydroxidelektrode—I. Über das nickel (II)-hydroxidhydrat. *Electrochimica Acta* (1966) 11, 8, 1079-1087.
94. Zheng, Y. R. *et al.* Cobalt diselenide nanobelts grafted on carbon fiber felt: an efficient and robust 3D cathode for hydrogen production. *Chemical Science* (2015) 6, 8, 4594-4598.
95. Tian, J., Liu, Q., Asiri, A. M., Alamry, K. A. & Sun, X. Ultrathin graphitic C₃N₄ nanosheets/graphene composites: Efficient organic electrocatalyst for oxygen evolution reaction. *ChemSusChem* (2014) 7, 8, 2125-2130.
96. Jiang, Q. *et al.* Facile Synthesis of Black Phosphorus: an Efficient Electrocatalyst for the Oxygen Evolving Reaction. *Angewandte Chemie - International Edition* (2016) 128, 44, 14053-14057.
97. Wurster, B., Grumelli, D., Hötger, D., Gutzler, R. & Kern, K. Driving the Oxygen Evolution Reaction by Nonlinear Cooperativity in Bimetallic Coordination Catalysts. *Journal of the American Chemical Society* (2016) 138, 11, 3623-3626.
98. Xia, B. Y. *et al.* A metal-organic framework-derived bifunctional oxygen electrocatalyst. *Nature Energy* (2016) 1, 1, 1-8.

References

99. Li, J. *et al.* Nanoparticle Superlattices as Efficient Bifunctional Electrocatalysts for Water Splitting. *Journal of the American Chemical Society* (2015) 137, 45, 14305-14312.
100. Du, X., Yang, Z., Li, Y., Gong, Y. & Zhao, M. Controlled synthesis of Ni(OH)₂/Ni₃S₂ hybrid nanosheet arrays as highly active and stable electrocatalysts for water splitting. *Journal of Materials Chemistry A* (2018) 6, 16, 6938-6946.
101. Zhu, M., Shao, Q., Qian, Y. & Huang, X. Superior overall water splitting electrocatalysis in acidic conditions enabled by bimetallic Ir-Ag nanotubes. *Nano Energy* (2019) 56, 330-337.
102. Li, M. *et al.* Ni Strongly Coupled with Mo₂C Encapsulated in Nitrogen-Doped Carbon Nanofibers as Robust Bifunctional Catalyst for Overall Water Splitting. *Advanced Energy Materials* (2019) 9, 10, 1803185.
103. Schmidt, O. *et al.* Future cost and performance of water electrolysis: An expert elicitation study. *International Journal of Hydrogen Energy* (2017) 42, 52, 30470-30492.
104. Zhang, J. *et al.* Single-Atom Au/NiFe Layered Double Hydroxide Electrocatalyst: Probing the Origin of Activity for Oxygen Evolution Reaction. *Journal of the American Chemical Society* (2018) 140, 11, 3876-3879.
105. Fujishima, A. & Honda, K. Electrochemical photolysis of water at a semiconductor electrode. *Nature* (1972) 238, 5358, 37-38.
106. Pelaez, M. *et al.* A review on the visible light active titanium dioxide photocatalysts for environmental applications. *Applied Catalysis B: Environmental* (2012) 125, 331-349.
107. Abe, R. Recent progress on photocatalytic and photoelectrochemical water splitting under visible light irradiation. *Journal of Photochemistry and Photobiology C: Photochemistry Reviews* (2010) 11, 4, 179-209.
108. Xing, J., Fang, W. Q., Zhao, H. J. & Yang, H. G. Inorganic photocatalysts for overall water splitting. *Chemistry - An Asian Journal* (2012) 7, 4, 642-657.
109. Varshni, Y. P. Temperature dependence of the energy gap in semiconductors. *Physica* (1967) 34.
110. Vella, E., Messina, F., Cannas, M. & Boscaino, R. Unraveling exciton dynamics in amorphous silicon dioxide: Interpretation of the optical features from 8 to 11 eV. *Physical Review B - Condensed Matter and Materials Physics* (2011) 83.
111. Maeda, K. Z-scheme water splitting using two different semiconductor photocatalysts. *ACS Catalysis* (2013) 3, 7, 1486-1503.
112. Maeda, K. Photocatalytic water splitting using semiconductor particles: History and recent developments. *Journal of Photochemistry and Photobiology C: Photochemistry Reviews* vol. 12 (2011) 12, 4, 237-268.
113. Bard, A. J. & Fox, M. A. Artificial Photosynthesis: Solar Splitting of Water to Hydrogen and Oxygen. *Accounts of Chemical Research* (1995) 28, 3, 141-145.

114. Hara, M. Cu₂O as a photocatalyst for overall water splitting under visible light irradiation. *Chemical Communications* (1998) 3, 357-358.
115. Maeda, K. *et al.* GaN:ZnO solid solution as a photocatalyst for visible-light-driven overall water splitting. *Journal of the American Chemical Society* (2005) 127, 23, 8286-8287.
116. Cao, S., Low, J., Yu, J. & Jaroniec, M. Polymeric Photocatalysts Based on Graphitic Carbon Nitride. *Advanced Materials* (2015) 27, 13, 2150-2176.
117. Li, H., Tu, W., Zhou, Y. & Zou, Z. Z-Scheme Photocatalytic Systems for Promoting Photocatalytic Performance: Recent Progress and Future Challenges. *Advanced Science* (2016) 3, 11, 1500389.
118. Zhou, P., Yu, J. & Jaroniec, M. All-solid-state Z-scheme photocatalytic systems. *Advanced Materials* (2014) 26, 29, 4920-4935.
119. Low, J. *et al.* A Review of Direct Z-Scheme Photocatalysts. *Small Methods* (2017) 1, 5, 1700080.
120. Maeda, K. Z-scheme water splitting using two different semiconductor photocatalysts. *ACS Catalysis* (2013) 3, 7, 1486-1503.
121. Dennler, G. *et al.* Charge carrier mobility and lifetime versus composition of conjugated polymer/fullerene bulk-heterojunction solar cells. *Organic Electronics* (2006) 7, 4, 229-234.
122. Wang, Qian, *et al.* Molecularly engineered photocatalyst sheet for scalable solar formate production from carbon dioxide and water. *Nature Energy* (2020) 5, 9, 703-710.
123. Kim, H., Lim, K. G. & Lee, T. W. Planar heterojunction organometal halide perovskite solar cells: Roles of interfacial layers. *Energy and Environmental Science* (2016) 9, 1, 12-30.
124. Pihosh, Y. *et al.* Photocatalytic generation of hydrogen by core-shell WO₃/BiVO₄ nanorods with ultimate water splitting efficiency. *Scientific Reports* (2015) 5, 1, 1-10.
125. Yang, X. *et al.* Interfacial optimization of g-C₃N₄-based Z-scheme heterojunction toward synergistic enhancement of solar-driven photocatalytic oxygen evolution. *Applied Catalysis B: Environmental* (2019) 244, 240-249.
126. Chen, X., Shen, S., Guo, L. & Mao, S. S. Semiconductor-based photocatalytic hydrogen generation. *Chemical Reviews* (2010) 110, 11, 6503-6570.
127. Abbood, H. A., Alabdie, A., Al-Hawash, A., Abbood, A. A. & Huang, K. Fabrication of double-sided comb-like F/Ce co-doped BiVO₄ micro/nanostructures for enhanced photocatalytic degradation and water oxidation. *Journal of Nanoparticle Research* (2020) 22, 4, 1-13.
128. Yin, X. *et al.* Realizing selective water splitting hydrogen/oxygen evolution on ferroelectric Bi₃TiNbO₉ nanosheets. *Nano Energy* (2018) 49, 489-497.

References

129. Hitoki, G. *et al.* An oxynitride, TaON, as an efficient water oxidation photocatalyst under visible light irradiation ($\lambda \leq 500$ nm). *Chemical Communications* (2002) 16, 1698-1699.
130. Yang, S. *et al.* Exfoliated graphitic carbon nitride nanosheets as efficient catalysts for hydrogen evolution under visible light. *Advanced Materials* (2013) 25, 17, 2452-2456.
131. Zhu, J., Xiao, P., Li, H. & Carabineiro, S. A. C. Graphitic carbon nitride: Synthesis, properties, and applications in catalysis. *ACS Applied Materials and Interfaces* (2014) 6, 19, 16449-16465.
132. Wang, X., Blechert, S. & Antonietti, M. Polymeric graphitic carbon nitride for heterogeneous photocatalysis. *ACS Catalysis* (2012) 2, 8, 1596-1606.
133. Zhu, J., Xiao, P., Li, H. & Carabineiro, S. A. C. Graphitic carbon nitride: Synthesis, properties, and applications in catalysis. *ACS Applied Materials and Interfaces* (2014) 6, 19, 16449-16465.
134. Wang, Y., Wang, X. & Antonietti, M. Polymeric graphitic carbon nitride as a heterogeneous organocatalyst: From photochemistry to multipurpose catalysis to sustainable chemistry. *Angewandte Chemie - International Edition* (2012) 51, 1, 68-89.
135. LIEBIG, J. Uber einige Stickstoff - Verbindungen. *Annalen der Pharmacie* (1834) 10, 1, 1-47.
136. Goettmann, F., Fischer, A., Antonietti, M. & Thomas, A. Metal-free catalysis of sustainable Friedel-Crafts reactions: Direct activation of benzene by carbon nitrides to avoid the use of metal chlorides and halogenated compounds. *Chemical Communications* (2006) 43, 4530-4532.
137. Wang, X. *et al.* Polymer semiconductors for artificial photosynthesis: Hydrogen evolution by mesoporous graphitic carbon nitride with visible light. *Journal of the American Chemical Society* (2009) 131, 5, 1680-1681.
138. Zhao, Z., Sun, Y. & Dong, F. Graphitic carbon nitride based nanocomposites: A review. *Nanoscale* (2015) 7, 1, 15-37.
139. Wang, Y., Wang, X. & Antonietti, M. Polymeric graphitic carbon nitride as a heterogeneous organocatalyst: From photochemistry to multipurpose catalysis to sustainable chemistry. *Angewandte Chemie - International Edition* (2012) 51, 1, 68-89.
140. Thomas, A. *et al.* Graphitic carbon nitride materials: Variation of structure and morphology and their use as metal-free catalysts. *Journal of Materials Chemistry* (2008) 18, 41, 4893-4908.
141. Shinde, S. S. *et al.* Scalable 3-D Carbon Nitride Sponge as an Efficient Metal-Free Bifunctional Oxygen Electrocatalyst for Rechargeable Zn-Air Batteries. *ACS Nano* (2017) 11, 1, 347-357.

-
142. Wu, G. *et al.* Carbon nanocomposite catalysts for oxygen reduction and evolution reactions: From nitrogen doping to transition-metal addition. *Nano Energy* (2016) 29, 83–110.
 143. Jiang, W. J. *et al.* Understanding the High Activity of Fe-N-C Electrocatalysts in Oxygen Reduction: Fe/Fe₃C Nanoparticles Boost the Activity of Fe-N_x. *Journal of the American Chemical Society* (2016) 138, 10, 3570-3578.
 144. Man, I. C. *et al.* Universality in Oxygen Evolution Electrocatalysis on Oxide Surfaces. *ChemCatChem* (2011) 3, 7, 1159-1165.
 145. Liang, Y. *et al.* Co₃O₄ nanocrystals on graphene as a synergistic catalyst for oxygen reduction reaction. *Nature Materials* (2011) 10, 10, 780-786.
 146. Schiros, T. *et al.* Connecting dopant bond type with electronic structure in n-doped graphene. *Nano Letters* (2012) 12, 8, 4025-4031.
 147. Savateev, A. & Antonietti, M. Ionic Carbon Nitrides in Solar Hydrogen Production and Organic Synthesis: Exciting Chemistry and Economic Advantages. *ChemCatChem* (2019) 11, 24, 6166-6176.
 148. Thomas, A. *et al.* Graphitic carbon nitride materials: Variation of structure and morphology and their use as metal-free catalysts. *Journal of Materials Chemistry* (2008) 18, 41, 4893-4908.
 149. Wang, X., Blechert, S. & Antonietti, M. Polymeric graphitic carbon nitride for heterogeneous photocatalysis. *ACS Catalysis* (2012) 2, 8, 1596-1606.
 150. Dontsova, D. *et al.* Triazoles: A New Class of Precursors for the Synthesis of Negatively Charged Carbon Nitride Derivatives. *Chemistry of Materials* (2015) 27, 15, 5170-5179.
 151. Lau, V. W. *et al.* Dark Photocatalysis: Storage of Solar Energy in Carbon Nitride for Time-Delayed Hydrogen Generation. *Angewandte Chemie - International Edition* (2017) 129, 2, 525-529.
 152. Savateev, A. *et al.* Potassium Poly(heptazine imides) from Aminotetrazoles: Shifting Band Gaps of Carbon Nitride-like Materials for More Efficient Solar Hydrogen and Oxygen Evolution. *ChemCatChem* (2017) 9, 167–174.
 153. Schlomberg, H. *et al.* Structural Insights into Poly(Heptazine Imides): A Light-Storing Carbon Nitride Material for Dark Photocatalysis. *Chemistry of Materials* (2019) 31, 18, 7478-7486.
 154. Biesinger, M. C. *et al.* Resolving surface chemical states in XPS analysis of first row transition metals, oxides and hydroxides: Cr, Mn, Fe, Co and Ni. *Applied Surface Science* (2011) 257, 3, 887-898.
 155. Shchukarev, A. V. & Korolkov, D. V. XPS study of group IA carbonates. *Central European Journal of Chemistry* (2004) 2, 347–362.

References

156. Jia, H. *et al.* A novel two-dimensional nickel phthalocyanine-based metal-organic framework for highly efficient water oxidation catalysis. *Journal of Materials Chemistry A* (2018) 6, 1188–1195.
157. Huang, M. L. *et al.* Energy-band parameters of atomic-layer-deposition Al₂O₃/InGaAs heterostructure. *Applied Physics Letters* (2006) 89, 1, 012903.
158. Vance, A. L. *et al.* XAS and XPS characterization of a surface-attached rotaxane. *Nano Letters* (2003) 3, 1, 81-84.
159. Mihelic, A. XANES spectroscopy. *of EXAFS, SEXAFS and XANES* (2002) 23, 2, 127-146.
160. Bare, S. XANES Measurements and Interpretation. *EXAFS Data Collection and Analysis Course, APS* (2005) 26, 29.
161. Yano, J. & Yachandra, V. K. X-ray absorption spectroscopy. *Photosynthesis Research* (2009) 102, 2, 241-254.
162. Rehr, J. J. & Ankudinov, A. L. Progress in the theory and interpretation of XANES. *Coordination Chemistry Reviews* (2005) 249, 1, 2, 131-140.
163. Oliveira, R. L. *et al.* Confinement of Cobalt Species in Mesoporous N-Doped Carbons and the Impact on Nitroarene Hydrogenation. *ACS Sustainable Chemistry & Engineering* (2020) 8, 30, 11171-11182.
164. Li, S. *et al.* Metal-Organic Precursor-Derived Mesoporous Carbon Spheres with Homogeneously Distributed Molybdenum Carbide/Nitride Nanoparticles for Efficient Hydrogen Evolution in Alkaline Media. *Advanced Functional Materials* (2019) 29, 1–10.
165. Zhao, S. *et al.* Ultrathin metal-organic framework nanosheets for electrocatalytic oxygen evolution. *Nature Energy* (2016) 1, 1–10.
166. Zitolo, A. *et al.* Identification of catalytic sites in cobalt-nitrogen-carbon materials for the oxygen reduction reaction. *Nature Communications* (2017) 14, 9, 937-942.
167. Aikens, D. A. Electrochemical methods, fundamentals and applications. *Journal of Chemical Education* (1983) A25.
168. Mefford, J. T. *et al.* Water electrolysis on La_{1-x}Sr_xCoO_{3-δ} perovskite electrocatalysts. *Nature Communications* (2016) 7, 1, 1-11.
169. Zhao, X. *et al.* Macro/Microporous Covalent Organic Frameworks for Efficient Electrocatalysis. *Journal of the American Chemical Society* (2019) 141, 16, 6623-6630.
170. Gopi, S. & Kathiresan, M. 1,4-Phenylenediamine based covalent triazine framework as an electro catalyst. *Polymer* (2017) 109, 315–320.
171. Dontsova, D. *et al.* Triazoles: A New Class of Precursors for the Synthesis of Negatively Charged Carbon Nitride Derivatives. *Chemistry of Materials* (2015) 27, 5170–5179.

-
172. Islam, M. M., Tentu, R. D., Ali, M. A. & Basu, S. Enhanced Visible-Light-Driven Activity of Sodium-, Calcium- and Aluminium-Inserted g-C₃N₄. *ChemistrySelect* (2018) 3, 11241–11250.
 173. Horvath-bordon, E. *et al.* Elisabeta Horvath-Bordon (2004) 7, 3900–3908.
 174. Cobo, S. *et al.* A Janus cobalt-based catalytic material for electro-splitting of water. *Nature Materials* (2012) 11, 9, 802-807.
 175. Moniz, S. J. A., Shevlin, S. A., Martin, D. J., Guo, Z. X. & Tang, J. Visible-light driven heterojunction photocatalysts for water splitting-a critical review. *Energy and Environmental Science* (2015) 8, 3, 731-759.
 176. Pinhassi, R. I. *et al.* Hybrid bio-photo-electro-chemical cells for solar water splitting. *Nature Communications* (2016) 7, 1, 1-10.
 177. McCrory, C. C. L., Jung, S., Peters, J. C. & Jaramillo, T. F. Benchmarking heterogeneous electrocatalysts for the oxygen evolution reaction. *Journal of the American Chemical Society* (2013) 135, 45, 16977-16987.
 178. Zhang, J., Zhao, Z., Xia, Z. & Dai, L. A metal-free bifunctional electrocatalyst for oxygen reduction and oxygen evolution reactions. *Nature Nanotechnology* (2015) 10, 5, 444-452.
 179. Danilovic, N. *et al.* Activity-stability trends for the oxygen evolution reaction on monometallic oxides in acidic environments. *Journal of Physical Chemistry Letters* (2014) 5, 14, 2474-2478.
 180. Sanchezcasalongue, H. G. *et al.* InSitu observation of surface species on iridium oxide nanoparticles during the oxygen evolution reaction. *Angewandte Chemie - International Edition* (2014) 126, 28, 7297-7300.
 181. Reier, T., Oezaslan, M. & Strasser, P. Electrocatalytic oxygen evolution reaction (OER) on Ru, Ir, and Pt catalysts: A comparative study of nanoparticles and bulk materials. *ACS Catalysis* (2012) 2, 8, 1765-1772.
 182. Song, F. & Hu, X. Ultrathin cobalt-manganese layered double hydroxide is an efficient oxygen evolution catalyst. *Journal of the American Chemical Society* (2014) 136, 47, 16481-16484.
 183. Wang, J. *et al.* Recent Progress in Cobalt-Based Heterogeneous Catalysts for Electrochemical Water Splitting. *Advanced Materials* (2016) 28, 2, 215-230.
 184. Zitolo, A. *et al.* Identification of catalytic sites in cobalt-nitrogen-carbon materials for the oxygen reduction reaction. *Nature Communications* (2017) 14, 9, 937-942.
 185. Ba, R. *et al.* Synthesis of Co-based bimetallic nanocrystals with one-dimensional structure for selective control on syngas conversion. *Nanoscale* (2015) 7, 29, 12365-12371.

References

186. Makuła, Patrycja, Michał Pacia, and Wojciech Macyk. How to correctly determine the band gap energy of modified semiconductor photocatalysts based on UV–Vis spectra. (2018) 6814-6817.
187. Lu, X. F. *et al.* An Alkaline-Stable, Metal Hydroxide Mimicking Metal-Organic Framework for Efficient Electrocatalytic Oxygen Evolution. *Journal of the American Chemical Society* (2016) 138, 27, 8336-8339.
188. O.V. Magdysyuk, F. Adams, H-P. Liermann, I. Spanopoulos, P.N. Trikalitis, M. Hirscher, R.E. Morris, M.J. Duncan, L.J. McCormick, R. E. D. Understanding the Adsorption Mechanism of Noble Gases Kr and Xe in CPO-27-Ni, CPO-27-Mg, and ZIF-8. 1–6 (2016) 16, 43, 23908-23914.
189. Xu, Y. *et al.* Ultrathin two-dimensional cobalt-organic framework nanosheets for high-performance electrocatalytic oxygen evolution. *Journal of Materials Chemistry A* (2018) 6, 44, 22070-22076.
190. Wang, X. L. *et al.* Exploring the Performance Improvement of the Oxygen Evolution Reaction in a Stable Bimetal–Organic Framework System. *Angewandte Chemie - International Edition* (2018) 57, 9660–9664.
191. Wang, X. K. *et al.* Two Novel Co(II)/Ni(II) coordination polymers based on 3,5-(di(2',5'-dicarboxylphenyl)benzoic acid ligand: Crystal structures, magnetic properties and oxygen evolution reaction. *Journal of Solid State Chemistry* (2019) 269, 348–353.
192. Cao, J. *et al.* An ultrathin cobalt-based zeolitic imidazolate framework nanosheet array with a strong synergistic effect towards the efficient oxygen evolution reaction. *Journal of Materials Chemistry A* (2018) 6, 18877–18883.
193. Meng, F., Zhong, H., Bao, D., Yan, J. & Zhang, X. In Situ Coupling of Strung Co₄N and Intertwined N-C Fibers toward Free-Standing Bifunctional Cathode for Robust, Efficient, and Flexible Zn-Air Batteries. *Journal of the American Chemical Society* (2016) 138, 32, 10226-10231.
194. Wang, W. *et al.* Atomic dispersion of Fe/Co/N on graphene by ball-milling for efficient oxygen evolution reaction. *International Journal of Hydrogen Energy* (2018) 43, 22, 10351-10358.
195. Guan, C. *et al.* Decorating Co/CoN_x nanoparticles in nitrogen-doped carbon nanoarrays for flexible and rechargeable zinc-air batteries. *Energy Storage Materials* (2019) 16, 243–250.
196. Hou, J. *et al.* Electrical Behavior and Electron Transfer Modulation of Nickel–Copper Nanoalloys Confined in Nickel–Copper Nitrides Nanowires Array Encapsulated in Nitrogen-Doped Carbon Framework as Robust Bifunctional Electrocatalyst for Overall Water Splitting. *Advanced Functional Materials* (2018) 28, 37, 1803278.
197. Shakeel, M., Arif, M., Yasin, G., Li, B. & Khan, H. D. Layered by layered Ni-Mn-LDH/g-C₃N₄ nanohybrid for multi-purpose photo/electrocatalysis: Morphology controlled

- strategy for effective charge carriers separation. *Applied Catalysis B: Environmental* (2019) 242, 485-498.
198. Lyu, F., Wang, Q., Choi, S. M. & Yin, Y. Noble-Metal-Free Electrocatalysts for Oxygen Evolution. *Small* (2019) 15, 1, 1804201.
 199. Liang, H. W. *et al.* Molecular metal-Nxcentres in porous carbon for electrocatalytic hydrogen evolution. *Nature Communications* (2015) 6, 1, 1-8.
 200. Wang, X. *et al.* Polymer semiconductors for artificial photosynthesis: Hydrogen evolution by mesoporous graphitic carbon nitride with visible light. *Journal of the American Chemical Society* (2009) 131, 5, 1680-1681.
 201. Gong, Q. *et al.* Ultrasmall and phase-pure W₂C nanoparticles for efficient electrocatalytic and photoelectrochemical hydrogen evolution. *Nature Communications* (2016) 7, 1, 1-8.
 202. Bard, A. J. & Fox, M. A. Artificial Photosynthesis: Solar Splitting of Water to Hydrogen and Oxygen. *Accounts of Chemical Research* (1995) 28, 3, 141-145.
 203. Zhang, Jinshui, *et al.* Photocatalytic oxidation of water by polymeric carbon nitride nanohybrids made of sustainable elements. *Chemical Science* (2012) 3, 2, 443-446.
 204. Lotsch, B. V. & Schnick, W. From triazines to heptazines: Novel nonmetal tricyanomelaminates as precursors for graphitic carbon nitride materials. *Chemistry of Materials* (2006) 18, 7, 1891-1900.
 205. Oliveira, R. L. *et al.* Confinement of Cobalt Species in Mesoporous N-Doped Carbons and the Impact on Nitroarene Hydrogenation. *ACS Sustainable Chemistry & Engineering* (2020) 8, 30, 11171-11182.
 206. Jun, Y. S., Hong, W. H., Antonietti, M. & Thomas, A. Mesoporous, 2D hexagonal carbon nitride and titanium nitride/carbon composites. *Advanced Materials* (2009) 21, 23, 2430-2435.
 207. Lu, B., Liu, Q. & Chen, S. Electrocatalysis of Single Atom Sites: Impacts of Atomic Coordination. *ACS Catalysis* (2020) 10, 14, 7584-7618.
 208. Titova, Y. Y., Belykh, L. B. & Schmidt, F. K. EPR Spectroscopy of catalytic systems based on nickel complexes of 1,4-diaza-1,3-butadiene (α -diimine) ligands in hydrogenation and polymerization reactions. *Low Temperature Physics* (2015) 41, 1, 25-28.
 209. Taguchi, A. T., O'Malley, P. J., Wraight, C. A. & Dikanov, S. A. Hyperfine and nuclear quadrupole tensors of nitrogen donors in the Q A site of bacterial reaction centers: Correlation of the histidine N δ tensors with hydrogen bond strength. *Journal of Physical Chemistry B* (2014) 118, 31, 9225-9237.
 210. Schneider, J. & Bahnemann, D. W. Undesired role of sacrificial reagents in photocatalysis. *Journal of Physical Chemistry Letters* (2013) 3479-3483.

References

211. Swift, T. J. & Connick, R. E. Proton Relaxation in Dilute Solutions of Cobalt(II) and Nickel(II) Ions in Methanol and the Rate of Methanol Exchange of the Solvation Sphere The Journal of Chemical Physics. *Proton Relaxation Times in Paramagnetic Solutions The Journal of Chemical Physics* (1962) 40, 9, 2686-2692.
212. Delpuech, J. J. Application of multinuclear magnetic resonance spectroscopy to solvation and aggregation phenomena in solution Plenary lecture. *Analyst* (1992) 117, 3, 267-288.
213. Schoedel, A., Ji, Z. & Yaghi, O. M. The role of metal–organic frameworks in a carbon-neutral energy cycle. *Nature Energy* (2016) 1, 4, 1-13.
214. Lu, B., Liu, Q. & Chen, S. Electrocatalysis of Single Atom Sites: Impacts of Atomic Coordination. *ACS Catalysis* (2020) 10, 14, 7584-7618.
215. Hiraba, H., Nogawa, H., Koizumi, H., Kodaira, A. & Akahane, S. Effect of multi-purpose primers on the bond durability between tri-n-butylborane initiated resin and gold alloy. *Journal of Prosthodontic Research* (2019) 63, 1, 95-99.
216. Aria, A. I. *et al.* Time Evolution of the Wettability of Supported Graphene under Ambient Air Exposure. *Journal of Physical Chemistry C* (2016) 120, 4, 2215-2224.
217. Grosvenor, A. P., Kobe, B. A., Biesinger, M. C. & McIntyre, N. S. Investigation of multiplet splitting of Fe 2p XPS spectra and bonding in iron compounds. *Surface and Interface Analysis* (2004) 36, 12, 1564-1574.
218. Huang, M. L. *et al.* Energy-band parameters of atomic-layer-deposition Al₂O₃/InGaAs heterostructure. *Applied Physics Letters* (2006) 89, 1, 012903.